Master's thesis

NTNU
Norwegian University of Science and Technology
Faculty of Engineering
Department of Marine Technology

Frode Moen

Experimental Analysis of Sea-bass Hydrodynamics

Master's thesis in MARINE TECHNOLOGY
Supervisor: Marilena Greco
June 2020

NTNU
Norwegian University of
Science and Technology

NTNU Trondheim
Norwegian University of Science and Technology
Faculty of Engineering Science and Technology
Department of MarineTechnology

MASTER THESIS IN MARINE TECHNOLOGY

Spring 2020

FOR

Frode Moen

Experimental Analysis of Sea-bass Hydrodynamics

(Eksperimentell analyse av havabbor -hydrodynamikk)

Fish can be quite fast and efficient swimmers, highly skilled in cruising and manoeuvring their bodies. Some can move at speeds equal to several body lengths per second or reach accelerations much larger than gravity acceleration. Understanding the unsteady fish hydrodynamics relevant for these important fish skills can guide towards novel bio-inspired concepts for underwater vehicles and robots.

In the project thesis, the candidate examined preliminary tests on sea-bass locomotion previously carried out in an authorized CNR-IAS lab, within a collaboration of the Italian research institute CNR-INM with the Centre of Excellence NTNU AMOS. Using top-view videos from the tests for one speed case, he attempted the modeling of the midline motion and identification of involved wavelength and tail bit frequency. The student also selected the open-source platform, openFOAM, for the complementary studies in the master thesis.

Objective

The present master thesis aims to investigate the fish hydrodynamics based on analysis of available sea-bass experiments.

The work should be carried out in steps as follows:

1. Summarize major findings/outcomes from the project thesis, reporting on the background and motivation, literature study, sea-bass experiments and analysis so far carried out. Possibly complement the literature survey in order to identify state-of-the-art of the problem.
2. Examine the analysis performed during the project thesis for the fish motion identification in terms, i.e. fish midline motion, its envelope, its connected frequencies and wavelengths, in order to identify/avoid possible error sources in the results within the adopted strategy based on the use Fast Fourier Transform (FFT) of targeted points distributed along the fish midline.
3. Consider at least an alternative strategy to perform this analysis based on available literature, for example the use of Least-Square-Method (LSM), verify its feasibility and apply it to at least one experimental case. Discuss comparatively this and the FFT strategy. In this context, examine the possibility to distinguish the locomotion and the recoil contributions to the fish motions in order to more accurately identify the fish-motion parameters.
4. Describe the OpenFOAM solver selected for the study, in terms of used fluid-flow assumptions, solution strategy and gridding features. Perform a numerical convergence study applying the solver to the sea-bass fish modelled as rigid geometry (identified in step 2) in steady inflow without an angle of attack inside a channel.

Apply the method to investigate the effect of the side walls used in the experimental set up on the numerical results.

5. Draw the conclusions from the studies carried out and their results and discuss possible further research steps in connection with use of image analysis in life-fish experiments.

The work may show to be more extensive than anticipated. Some topics may therefore be left out after discussion with the supervisor without any negative influence on the grading.

The candidate should in his report give a personal contribution to the solution of the problem formulated in this text. All assumptions and conclusions must be supported by mathematical models and/or references to physical effects in a logical manner.

The candidate should apply all available sources to find relevant literature and information on the actual problem.

The thesis should be organised in a rational manner to give a clear presentation of the work in terms of exposition of results, assessments, and conclusions. It is important that the text is well written and that tables and figures are used to support the verbal presentation. The thesis should be complete, but still as short as possible. In particular, the text should be brief and to the point, with a clear language. Telegraphic language should be avoided.

The thesis must contain the following elements: the text defining the scope (i.e. this text), preface (outlining project-work steps and acknowledgements), abstract (providing the summary), table of contents, main body of thesis, conclusions with recommendations for further work, list of symbols and acronyms, references and (optional) appendices. All figures, tables and equations shall be numerated.

The supervisor may require that the candidate, in an early stage of the work, present a written plan for the completion of the work. The plan should include budget for the use of computer and laboratory resources that will be charged to the department. Overruns shall be reported to the supervisor.

From the thesis it should be possible to identify the work carried out by the candidate and what has been found in the available literature. It is important to give references to the original source for theories and experimental results.

Supervisor : Marilena Greco
Co-supervisor : Claudio Lugni

Submitted : January 15th 2020
Deadline : June 30th 2020

Marilena Greco
Supervisor

Preface

The work included in this thesis was conducted during the spring of 2020, and marks the end of a 5 year master program within Marine Technology at the Norwegian University of Science and Technology (NTNU).

The topic of research was proposed by my supervisor Prof. Marilena Greco and inspired by an on-going project within the Centre of Excellence NTNU AMOS in collaboration with the Italian research institute CNR-INM. The work has been carried out independently, with the assist and support of Prof. Greco and Adjunct Professor Claudio Lugni. I hope this thesis will inspire others to pursue research within the field of bio-inspired mechanism for underwater vehicles and robots, and I am excited about what Prof. Greco and her team will accomplish in the years to come.

As a dyslexic, I have faced additional challenges during my time as a student. It has been a long dream to obtain a M. Sc. degree, and I am proud to fulfill that goal with normal study progression. In addition to these challenges, the work in this thesis has been carried out during the global pandemic of Covid-19. This have led to challenging work conditions closing down the university facilities and making collaboration with my supervisor and her team harder. However, NTNU has done a wonderful job making the best of a difficult situation, and I am grateful for all fruitful discussions with people relevant knowledge despite the national restrictions.

Basic knowledge of hydrodynamics and fish morphology is recommended, but not necessary to understand the topics and contributions presented in this thesis.

Trondheim, 30-06-2020

Frode Moen

Acknowledgments

First and foremost, I would like to thank my supervisor Professor Marilena Greco for providing excellent guidance and assistance in conducting this work. Her field of research has been of interest to me for some time, and I have truly enjoyed being part of her team. My co-supervisor, Adjunct Professor Claudio Lugni has been especially helpful regarding the technical input and theoretical principles for this work.

Thanks to Prof. Greco's team and resources, I have been able to complete and achieve more than I had hoped during the spring of 2020. There are many researchers affiliated with NTNU I would like to thank for their contributions, and I will mention some of them here. My appreciation goes to PhD Candidate Hui-li Xu, PhD Candidate Mohd Atif Siddiqui and PhD Candidate Shaojun Ma. Hui-li showed great enthusiasm and introduced me to different ways of creating a mesh and helping me with openFoam and associated software. I am also grateful for the fruitful discussions I had with Atif about OpenFOAM. Additionally, I would like to thank Shaojun for sharing his insights on the sea bass experiment of which the thesis is based upon.

It is rewarding to work in a team with such a good flow of information and people who are always willing to take a pause from their own endeavors to assist others. It has been a privilege to be under Prof. Greco's supervision and I look with excitement at what she and her team will accomplish in the near future.

Abstract

Prior to this Master thesis, an experiment was conducted to analyse the hydrodynamics involved in steady swimming of a sea bass. The first part of this work propose an analytical solution of the sea bass' swimming form (i.e. locomotion) based on this experiment. A preliminary study was conducted to understand the necessary theoretical principles such as the fish-like hydrodynamics and the efficient swimming characteristics of a sea bass. This thesis will present the two major aspects of the swimming form, namely the locomotion and recoil. These two swimming mechanisms have been analysed separately with the aim of exploiting their strengths in underwater robotics. Two methods that stand out in the relevant analysis have been the Fast Fourier Transforms (FFT) and the Least square method (LSM).

To analyse the fish movement a camera was fixed with a bird's eye perspective above the fish during the experiment. However, the problem with the experimental setup was that the camera had too low resolution meaning that multiple object was visually disturbing with the outline of the fish. Therefore a comprehensive image processing was conducted using a proposed semi automatic code to decrease this disturbance and enhance the detected outline of the fish. The consequence of the identified midline being to rough, was that a curve fitting process had to be done in order to predict a better midline. Furthermore, the frequency, amplitude, phase and wave number was found for the combined fish motion using a Fast Fourier Transform. To identify the fish motion without influencing the midline, the Least Square Method was then used. By evaluating points directly from the midline, an analytical expression for both the locomotion and the recoil was found. Finally, the influence of wall effect in the experiment was evaluated creating a fish foil replica of the sea bass. This was implemented using the software OpenFOAM.

After proposing the methods described above, results were obtained and discussed. One interesting finding was that the experiment of which the analysis and results were based on show room for improvement. The fish makes unexpected maneuvers and show an unnatural behaviour causing the post analysis of the steady swimming form challenging. A proposed solution is allowing the fish to swim for a longer period of time to reach a stable swimming mode before starting the experiment. Additionally, other choice of background colors and materials might improve the experimentation setup.

When extracting the locomotion, the biggest challenge was to overcome the physical aspects of the phase shifts. Despite this, the results were satisfactory, but a more thorough analysis is recommended for further work. Another motivation for further work is to enhance the linearization method for the reference law of the LSM. OpenFOAM has shown to be a powerful framework in analysing the locomotion of the sea bass. The numerical method relies heavily on the chosen grid, which may be further enhanced to obtain even better future results, when imposing the locomotion.

Sammendrag

I forkant av denne masteroppgaven ble det utført et eksperiment for å analysere hydrodynamikken for det stabile strømningsbildet til en havabbor. Den første delen av dette arbeidet foreslår en analytisk løsning av havabborens svømmeform (dvs. bølgebevegelse) basert på dette eksperimentet. Et litteraturstudie ble utført for å forstå de nødvendige teoretiske prinsippene som hydrodynamikk for fisk og de effektive svømmeferdighetene til en havabbor. Denne oppgaven vil legge fram de to hovedbidragene til svømmebevegelsen, nemlig bølgebevegelse og rekyl. Disse to svømmemekanismene er analysert hver for seg med det formål å utnytte deres styrker for undervannsrobotikk. To sentrale metoder i oppgavens analyse har vært Fast Fourier Transforms (FFT) og Least square-metoden (LSM).

For å analysere fiskebevegelsen under eksperimentet ble et kamera hengt opp i fugleperspektiv over fisken. Problemet med det eksperimentelle oppsettet var imidlertid at kameraet hadde for lav oppløsning, noe som betyr at flere objekter var visuelt forstyrrende for omrisset til fisken. Derfor ble en omfattende bildebehandling utført ved bruk av en foreslått semiautomatisk kode for å redusere denne forstyrrelsen og forbedre den observerte omrisset av fisken. Fordi den identifiserte midtlinjen var for grov, måtte en kurvetilnærming gjennomgjøres for å forutsi en bedre midtlinje. Videre ble frekvensen, amplituden, fasen og bølgetallet funnet for den kombinerte fiskebevegelsen ved bruk av FFT. For å identifisere fiskebevegelsen uten å påvirke midtlinjen ble LSM deretter brukt. Ved å evaluere poeng direkte fra midtlinjen ble det funnet et analytisk uttrykk for både bevegelsen og rekylen. Til slutt ble påvirkningen av veggens tilstedeværelse i eksperimentet evaluert og laget en form-kopi av havabboren. Dette ble implementert ved hjelp av programvaren OpenFOAM.

Etter å ha foreslått metodene beskrevet ovenfor, ble resultater funnet og diskutert. Et interessant funn var at eksperimentet som analysen og resultatene var basert på, viser rom for forbedring. Fisken gjør uventede manøvrer og viser en unaturlig oppførsel som gjør analysen av den stabile svømmeformen utfordrende. En foreslått løsning er å la fisken svømme over lengre tid for å nå et stabil svømmemønster før eksperimentet starter. I tillegg kan andre valg av bakgrunnsfarger og materialer forbedre eksperimentoppsettet.

Den største utfordringen ved å hente ut bevegelsen, var å overvinne de fysiske aspektene ved faseforskyvningen. Til tross for dette var resultatene tilfredsstillende, men en grundigere analyse anbefales for videre arbeid. En annen motivasjon for videre arbeid er å forbedre lineariseringsmetoden for referanseloven til LSM. OpenFOAM har vist seg å være et kraftig rammeverk for å analysere havabborens bevegelse. Den numeriske metoden er avhengig av det valgte “grid”, som kan forbedres ytterligere for å oppnå enda bedre fremtidige resultater.

Contents

List of Tables

List of Figures

This appendix contains some of the commonly used abbreviations throughout the thesis.

Re Reynolds number

St Strouhal number

BCF body and/or caudal fin

MPF median and/or paired fin

CFD computational fluid dynamics

AUV Autonomous Underwater Vehicle

CoM Center of Mass

COT Cost of Transport

$F_R^{'}$ The radial reaction force

$F_T^{'}$ The horizontal component to the thrust contribution

$F_L^{'}$ The lateral component perpendicular to the thrust direction

U Average forward velocity

p Pressure

L Relative length

ν Kinematic viscosity

f Tail beat frequency

A Width of the wake

κ Wave number

ω Angular frequency

ϵ Phase shift

FFT Fast Fourier Transform

LSM Least Square Method

BL Body length

NAN Not a number

λ Wave length

LHS Left hand side

RHS Right hand side

BC Boundary condition

CPU Central processing unit

δ Boundary layer

C_d Drag coefficient

C_l Lift coefficient

Chapter 1

Introduction

1.1 Background

During the late 1980's and 1990's, the development of Autonomous Underwater Vehicle (AUV's) made a leap in technology [6], as Inertial Navigation Systems (INS), underwater communication and hardware technology (batteries, sensors, etc.) became better. Stan Murphy, Bob Francois and Terry Ewar was the first developed a AUV. This was done in the Applied Physics Laboratory at the University of Washington in 1957 [10]. Since then, the design has developed towards many fields of application through research, recognition, and underwater manipulation, and is today mandatory in ocean science.

AUV's are independent marine systems, in terms of power and intelligence [1] and commonly maneuverable in three dimension. Autonomy is their biggest advantage, which minimizes the risk of human fatalities. The applications for AUV's are numerous, stretching from offshore oil and gas, mineral exploration, military application, and in academic ocean science. Classic scientific operations include water column surveys [4] and bathymetric mapping [28, 13]. Operations below ice have also been explored, e.g. Lighthill [11], Barrett [2]. Common characteristics within scientific usage are large areas and prolonged/persistent time, with focus on data recovery.

For a survation mission, sensor payload allows for analyzing and navigation, while the propulsive system allows the AUV to maneuver. To maintain constant speed, the thrust has to balance to hydrodynamic resistance on the AUV. In order to reduce thrust force, resistance has to be reduced. Traditionally, this is done through optimization with respect to hull shape and hull area.

In effort to further develop the thrust performances of AUV's, bio-inspired solutions have been investigated since the first AUV was created. Fish produce an efficient jet, by generating vortices in the wake of their tails, rotating compatible with the thrust vector. Traditional screw propeller waste power when it generating a jet perpendicular to the thrust direction [24]. Thus, the coordinated movements of the fish body and tail are a potential source for efficiency.

For these reasons, the huge potential payoffs of aquatic animals locomotion are beyond the modern nautical technology. Despite the fact that biological swimmers propulsive performances are still far to reach, researchers all around the world has developed prototypes of robotic fish. Driven by the goal to exploit the best that nature had to offer, new ways of thinking have guided the designs towards fish-shaped AUV's, e.g. Ghostswimmer [20], developed by Boston Engineering as the first commercialized robotic fish.

1.2 Motivation

The complexity of fish locomotion mechanisms has developed through years of evolution. Swimming techniques evolved as fish had adjust to the environment and ecosystem. Efficient swimming methods to minimize the use of energy are of interest for bio-inspired concepts for underwater vehicles and robots that have a limited power supply. In addition to superior cruising, fish also have high efficiency, long endurance ability, high maneuverability and low noise, which can potentially provide inspiration for a propulsion that will outperform the thrusters used today. The advantages of a propulsion system without noise, could be of additional significance, especially for military applications.

The aim is to improving the capabilities of underwater vehicles in terms of both speed and manoeuvrability, by replacing the conventional screw propellers with a more efficient bio-ispired thruster. This dose not necessarily mean creating fish robot, but to select and or retrieve motions from fish. To the aim of selecting these motions, it is essential to investigate and understand how fish swims and creating fish robot is a part of understanding how fish generates thrust. To this extent the locomotion of fish is the most studied motion for power-efficient cruising. Even though locomotion has been thoroughly studied in the past, it will still require a lot of investigation to fully understand.

Conventional AUV's are primarily interested in replicating the advantages of steady efficient swimming. Specific swimming modes can be replicated from the understanding of the fluid mechanics principles through a multiphysics approach. Understanding the relevant fish hydrodynamics for these important fish mechanisms can, with an efficient research approach and numerical modeling guide towards new designs, drive the theoretical developments in the marine industry further.

1.3 Main contribution

The main contribution from this thesis is:

- A semi-automatic image processing procedure to identify fish
- A constructed fish motion function.
- A separated locomotion function.

1.4 Outline

Chapter 1 In the Introduction the background, motivation, main contribution and the outline of the thesis is presented.

Chapter 2 The first part of the thesis have regarded the classification of the various swim modes of locomotion, along with the contributions of thrust. An extensive review of mathematical swimming expressions together with an overview of the experiment on sea bass is presented.

Chapter 3 This chapter contains the experimental analysis of the sea bass. The video for video analysing is initially chosen. Thereafter, a thorough image processing procedure is performed with a semi automatic iteration process, in order to identify the fish. Based on the processed image, the midline is constructed, followed by replicating the fish motion as a simplified function by use of a Fast Fourier Transform. In order to identify the locomotion, the fish motion is separated to locomotion and recoil with a Least Square Method.

Chapter 4 This chapter contains the numerical analysis of the sea bass. A numerical convergence study applying the solver to the sea-bass fish modelled as rigid geometry identified with image processing from Chapter 3. A steady inflow without an angle of attack inside a channel is conducted to investigate the effect of the side walls used in the experimental set up on the numerical results.

Chapter 5 This chapter contains the discussion of the thesis. It connects all the previous chapters together to evaluate the locomotion.

Chapter 6 This chapter contains the summary, conclusion and further work of the thesis.

Appendix A A table of travelling index of BCF fish analyzed from the biological data, used to verify the locomotion.

Appendix B Midline construction, contains all the verification frames for the different steps in Chapter 3.

Appendix C Midline Reconstruction, contains all the verification of the FFT input and the curve fitting.

Appendix D Experimental layout, contains an additional visual insight to the experiment.

Appendix E OpenFOAM, contains all additional plots for chosing the cell size.

Chapter 2

Preliminary work

To exploit the best that nature has to offer, it is essential for engineers to evaluate their own underwater vehicles and robots design with a wide background knowledge of the swimming abilities and performance of fish. The following chapter is meant to give a thorough insight to the fish propulsion, with focus on swimming mechanics relevant for the sea bass, figure 2.1.

The European sea bass is in the Serranidae family and is common all over the Mediterranean, the Black Sea and the North Eastern Atlantic from Norway to Senegal. The sea bass investigated in this thesis comes from a fish farm in front of the Oristano Gulf in the south-west part of Sardinia.

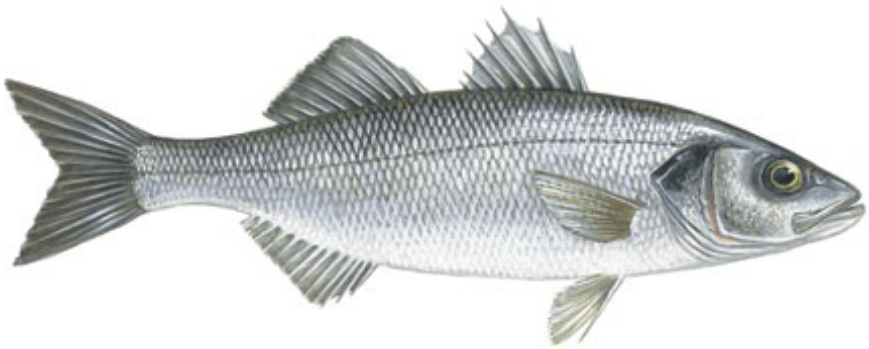

Figure 2.1: European Sea bass [29]

2.1 Fish swimming modes

The main mechanical properties of water are incompressibility and high density. Incompressible media have a constant volume, regardless of the pressure, which allows the fish to move water during swimming [23]. The high density result in a buoyancy force that counterbalance the weight, and the combination of these two features allows the fish to move freely. Through years of evolution in this media, the most efficient swimming modes have been developed. The acting forces on fish are illustrated in figure 2.2. In the horizontal direction, both thrust and resistance forces is acting. While in the vertical direction, buoyancy, weight, and hydrodynamic lift are acting.

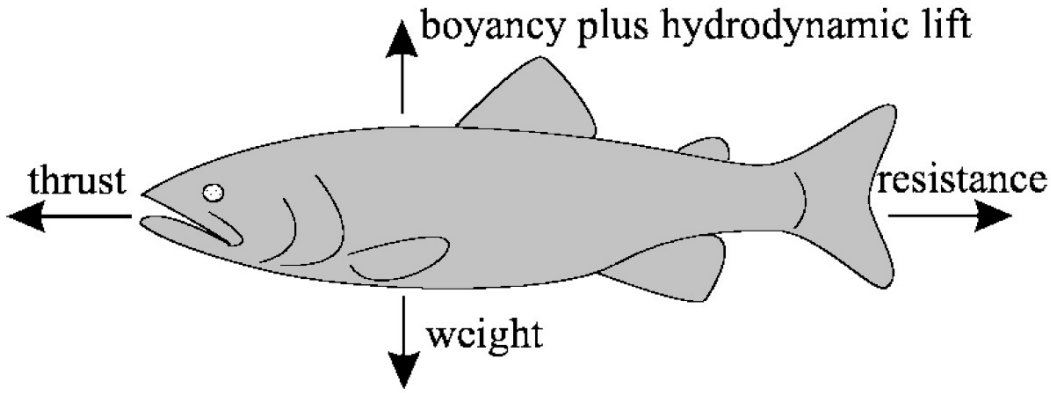

Figure 2.2: Forces acting on a swimming fish. Adapted from Sfakiotakis et al. [22]

The principle of conservation of momentum states that when you have an isolated system with no external forces, the initial total momentum of objects before a collision equals the final total momentum of the objects after the collision [8]. For fish with stead swimming, the resistance has to be balanced out by the thrust. Thus the thrust is the momentum transfer mechanism between drag, lift and acceleration reaction forces.

For a fish not affected by the free surface, there are two types of drag and they can be classified as pressure drag and skin friction drag. Skin friction drag is the drag between surface and water. The drag arises from the friction of the fluid against the "skin" of the object that is moving through it. Assuming that the water consist of Newtonian fluids, this drag is a conscience of the velocity gradients being proportional with the flow and large close to the body. Thus skin friction is caused by viscous drag in the boundary layer around the object, hence the body is dragging some amount of water with it and acts as a resistance force only.

Pressure drag arises as a consequence of the objects form. Pressure drag is the resistance generated due to differential pressure along the body. It is further classified as form drag, which is a result of the flow around the object while being solid, shown in figure (a) 2.10, and induced drag, that is a result of the objects ability to generation lift. Lift forces is a consequence of the difference in pressure between two opposite sides of a body, and results further in a force normal to the flow and is illustrated in Figure 2.3.

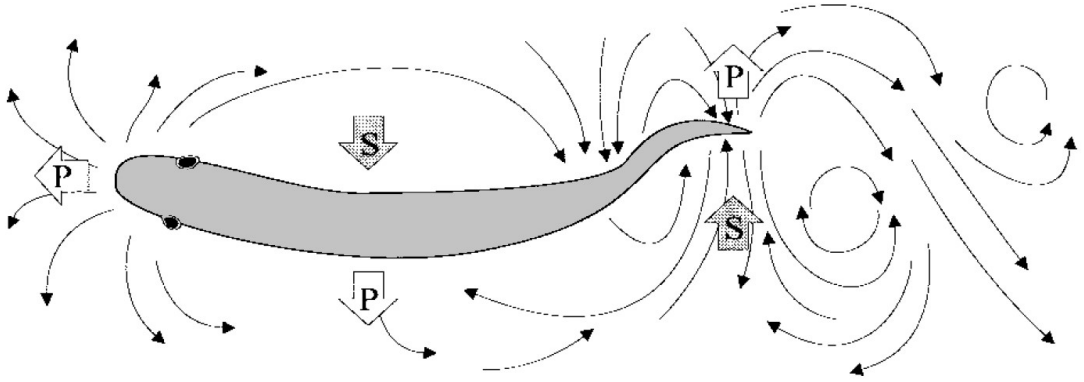

Figure 2.3: Flow field around a swimming body. Adapted from Sfakiotakis et al. [22]

Acceleration reaction is the additional inertial force that occurs when an object is accelerated in a fluid. It is normally associated with fluid-structure interaction mechanism and depends on the instantaneous acceleration, not velocity, of an object relative to its fluid environment [9]. While drag is resistance to motion through a fluid, the acceleration reaction is resistance to changes in the velocity of that motion.

The water close to a body accelerates as a propulsive wave towards the tail during locomotion. Added mass account for this force, and is equivalent the mass of water that must be effectively accelerated. Figure 2.4 illustrates the decomposed added mass forces and their contribution. $F_R^{'}$ is the radial reaction force perpendicular to the fluent flow. The horizontal component $F_T^{'}$ is the thrust contribution, while the lateral component $F_L^{'}$ is perpendicular to the thrust direction and is therefore a loss of potential thrust force. This force leads the body to sideslip and recoil [22].

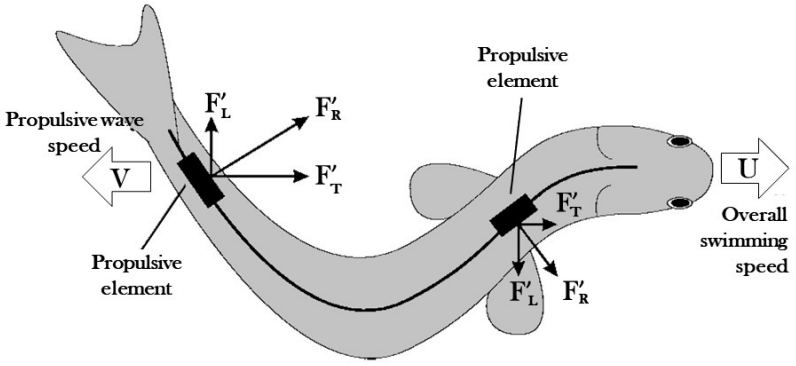

Figure 2.4: Added mass forces in BCF locomotion. Adapted from Sfakiotakis et al. [22]

Reynolds number is the ratio of inertial to viscous forces within a fluid which is subjected to relative internal movement due to different fluid velocities. It is an important parameter to implement for the fish swimming characteristics within numerical simulations, and is used to predict flow patterns in different fluid flow situations. The thrust generation consisting of drag, lift and added mass forces depends directly on the Reynolds number and is defined as,

$$Re = \frac{UL}{\nu} \tag{2.1}$$

where U is the flow speed or the average forward velocity (m/s), ν is the kinematic viscosity of the fluid (m^2/s) and L is the length of the fish (m). Re for typical adult fish swimming is $10^3 < Re < 5 \cdot 10^6$. In this range the thrust generation consist of the summation of lift, pressure drag and acceleration reaction forces. As indicated in figure 2.5, the inertial forces are dominant and viscous forces are usually neglected. At the higher range of Re for adult fishes, acceleration reaction, pressure drag and lift are all important contributions to the force [22].

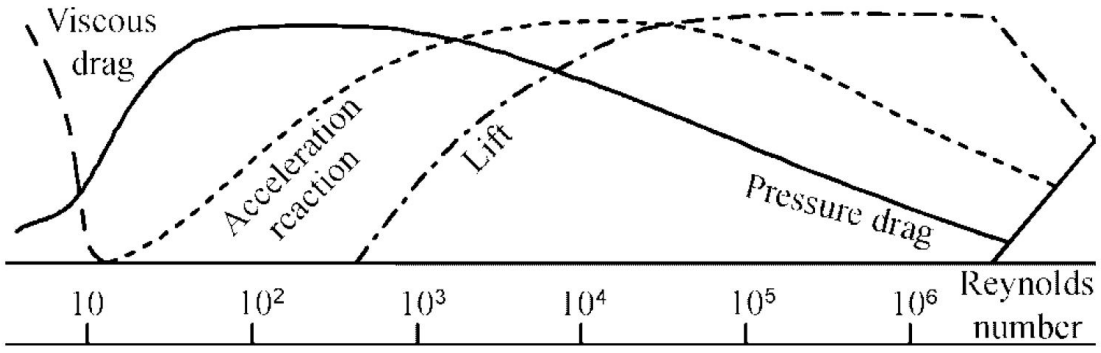

Figure 2.5: Functions of the contribution to the inertial forces relative to the Reynolds number. Adapted from Sfakiotakis et al. [22]

According to Taylor and Francis [3], analysing swimming performance and determining the aforementioned propulsive forces and their effect is very difficult as they are complex and cobbled. In order to evaluate each contribution individually and to understand the relationship between them and the swimming performances, it is beneficial to use Breder's classification of acquatic locomotion of marine animals to separate fish into different propulsion categories. Figure 2.6 shows the terminology describe features of fish,

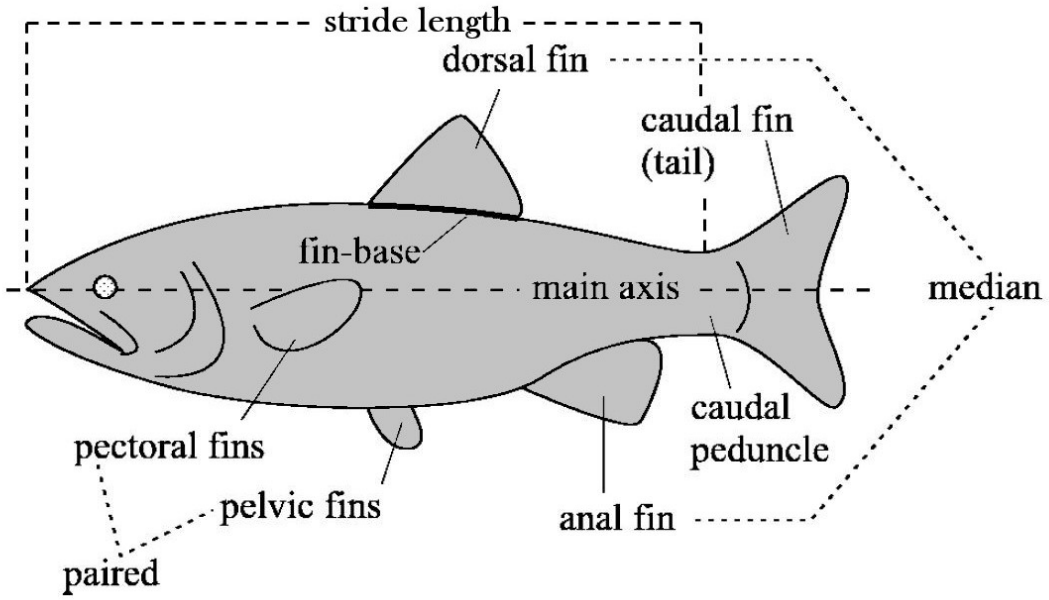

Figure 2.6: Terinology used to describe features of fish. Adapted from Sfakiotakis et al. [22]

To distinguish between the main contribution of propulsive forces, fish motion can be categorised into two types, Body and/or Caudal Fin (BCF) movements and Median and/or Paired Fin (MPF) propulsion. BCF locomotion is motion where the fish bends its body into a backward propulsive wave moving along the body towards the tail up to its caudal fin. The MPF has a similar behavior, but the bending motion is confined to their median and paired fins. MPF is essential for moving in slow speeds to accurate positioning, while the BCF is an efficient high speed movement with less accuracy and great accelerations [22]. Both BCF and MPF locomotion mechanisms are further classified as undulatory and oscillatory, depending on how the thrust is generated. Webb [28] identified which features corresponding to the different fish morphology specialization accelerating, cruising and manoeuvring, as shown in figure 2.7.

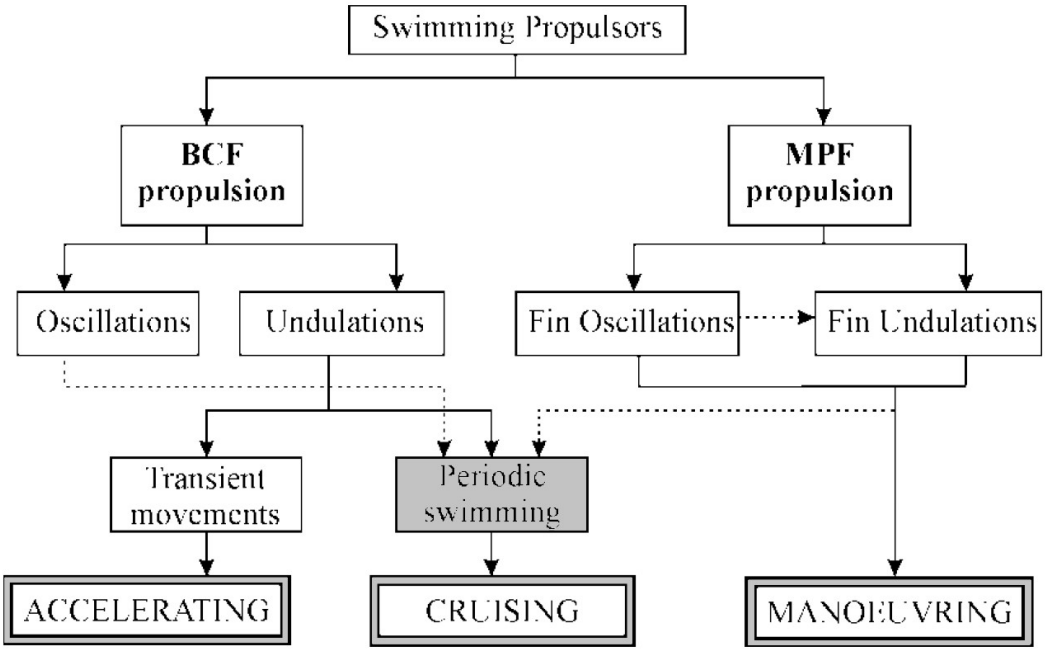

Figure 2.7: The diagram gives an overview swimming propulsion's. Adapted from Sfakiotakis et al. [22]

MPF propulsion or other fin propulsion will not be further discussed, as the motivation for this thesis is efficient swimming connected to underwater vehicles and robots.

The BCF undulatory mechanisms for generating thrust are further classified into four swimming modes. The terminology in figure 2.6 is used to distinguish the different modes. Undulatory BCF modes means that they produce thrust by passing transverse body waves along the fish, down to the caudal fin, like an added mass changing effect. These locomotion waves build up momentum towards the tail, giving them great thrust [3]. Figure 2.9 and 2.8 shows the four undulatory BCF modes. The difference between the swimming modes, is the length of the fish used to generate thrust and the forces that contribute to thrust generation. The different modes are divided into Angulliform, subcarangiform, carangiform and thunniform modes, which are listed based on the length of the fish used to generate thrust, from the longest to the shortest. Angulliform, subcarangiform and carangiform modes mainly exist of forces that contributes to the acceleration reaction as added mass effect.

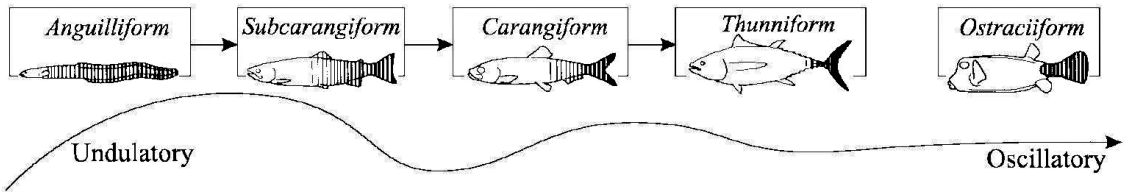

Figure 2.8: Indication of how much of the body is contributing to propulsion. Adapted from Sfakiotakis et al. [22]

The sea bass undulatory BCF mode is subcarangiform, similar to the rainbow trout [25]. The remaining modes will not be further discussed, as the motivation for this thesis is to investigate efficient swimming from the experiment done on sea bass. This also agrees with the aforementioned analysis provided by Webb [28].

Subcarangiform uses parts of the body to make large-amplitude undulations. Since there is not necessarily a complete wavelength on the fish, an yawing moment and recoil has to be assumed present. Recoil is a result of the added mass effect near the tail of the fish caused by the reaction force.

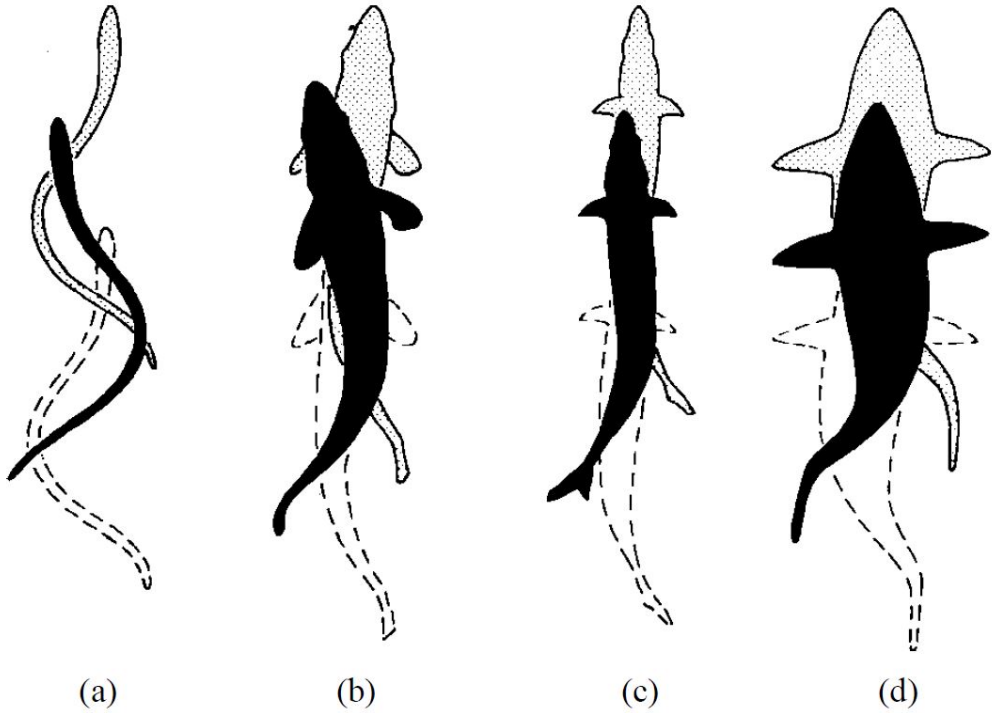

Figure 2.9: (a) Anguilliform, (b) Subcarangiform, (c) Carangiform and (d) Thunniform. Adapted from Sfakiotakis [22]

According to amputation experiments on salmonids and gadoids, the removal of fins shows little effect on steady periodic swimming speed. This is because the fish with subcarangiform swimming style get its main thrust contribution form locomotor waves passing back along the body [3]. Knowing that the efficient steady periodic swimming is little effected by fin removal, is beneficial for excluding fins when conducting image analysis and numerical simulations.

Locomotion can be classified as either periodic or transient. Periodic swimming is defined as swimming characteristic that goes in cycles. In this case it means that vortexes are created with the same tail frequency, ideally resulting in a constant cruising speed. The transient is an unsteady movement by changing frequencies, for escape maneuvers and turns. Transient motion will not further be discussed, because the target of this thesis is efficient swimming and not maneuverability and change of direction [22]. Hence the target for this thesis is to replicate the periodic locomotion for the undulatory subcarangiform sea bass.

The wake behind an undulatory BCF swimmer is illustrated in figure 2.10, and is a result of the tail moving back and forth generating a staggerd array of trailing vortexes of alternating sign. The tail movement give arise to vortexes with circulation where the direction of the velocity of the vortexes is aliened as a jet flow opposite of the fish direction. This effect generates thrust, unlike the common Von Karman vortex street from a cylinder which generates drag [3]. The main parameter for characterizing the wake behind a fish is the Strouhal number. The Strouhal number is essentially the ratio of unsteady to inertial forces, and for BCF swimmer, it is defined as,

$$St = \frac{fA}{U} \tag{2.2}$$

where f is the tail beat frequency in hertz, A is the width of the wake and U is the average forward velocity[3]. For a fish with subcarangiform swimming mode, the Strouhal number is predicted to be between $0.25 < St < 0.40$ [22].

When analysing BCF locomotion for subcarangiform modes with Re ranging between 10^4 and 10^6, St is

the essential parameter.

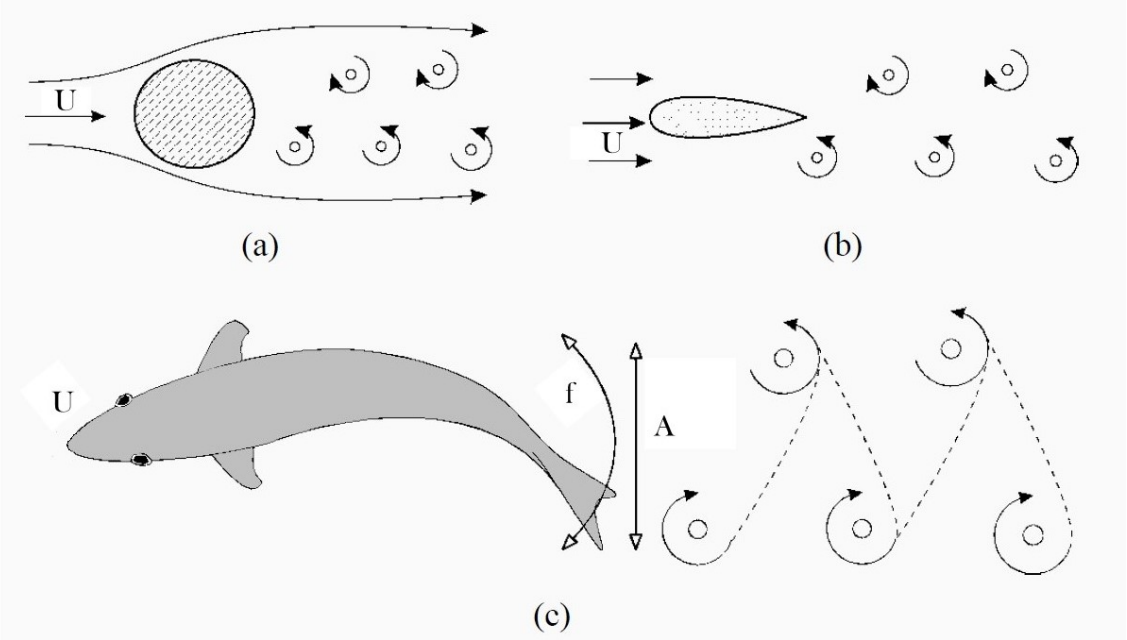

Figure 2.10: a) Von-Karman vortex b)Von-Karman vortex for a foil c) vortexes induced by the tail motion. Adapted from Sfakiotakis et al. [22]

2.2 Sea bass characteristics

Comparing the frequencies resulting in efficient cruising speed for different fish, it is beneficial to compare them with relative speed and movement. Speed is therefor given as body lengths per second. According to Taylor and Francis [3], most trout cruise at one to two body lengths per second for long durations. This gives an indication of what speeds to consider when finding the optimal cruising speed for the sea bass.

Cost of Transport (COT) and energy storage capability are used to express how efficient a fish or AUV is compared to endurance. It is shown in figure 2.11 that trout, similar to the sea bass can travel one to two body lengths per second, but can not do this for long.

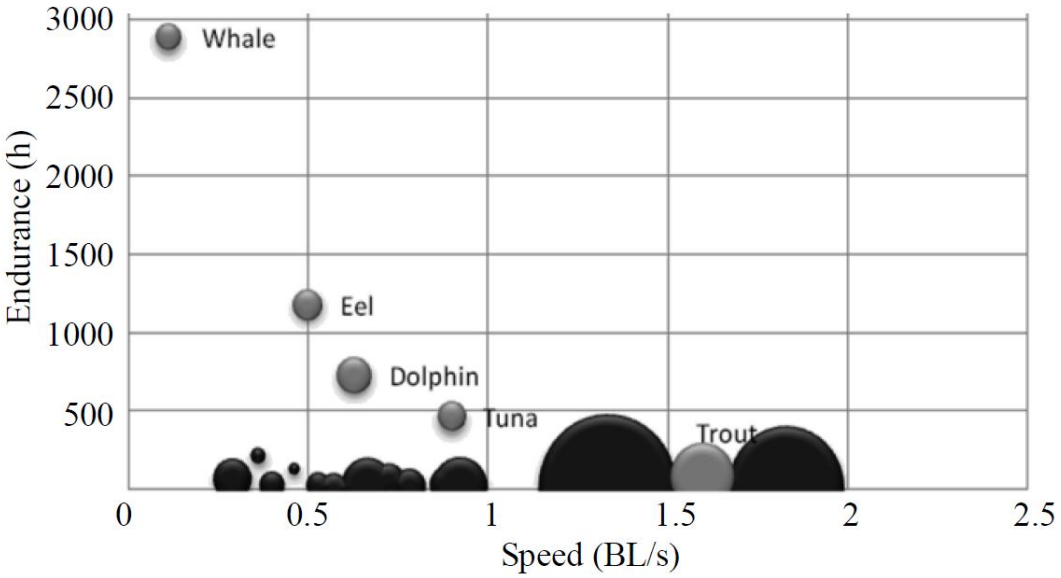

Figure 2.11: Endurance of marine animales(light grey) and AUVs(black). Adapted from Murphy [16]

Experiments done with different speeds indicate that the wave length for a sea bass is between $0.65 < \lambda < 1.25$ of the body length as indicated in figure 2.12.

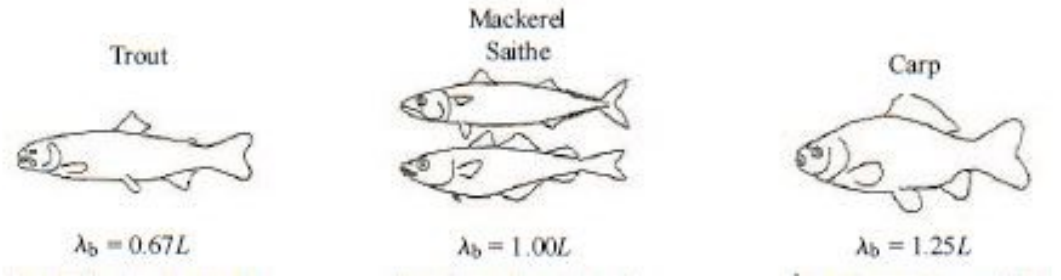

Figure 2.12: Espected wave length relative the body length, Adapted from Wardle et al. [27]

The sea bass as aforementioned, do not necessarily have a complete wavelength present along the body of the fish. The lateral component $F_L^{'}$ is perpendicular to the thrust direction and leads the body recoil. Recoil has to be assumed present. The fish motion in the experiment has to be assumed consequently as a combination of a lateral motion and recoil. Recoil is a combination of an horizontal oscillation, a oscillating heave of Center of Mass (CoM) and a pitch motion of CoM. The target for this thesis is to replicate the periodic locomotion for the undulatory subcarangiform sea bass. The oscillation heave motion of the CoM and the pitch motion that is superimposed to heave, most therefor be identified and removed.

$$
\begin{aligned}
y^{'}(x_i,t) &= \text{lateral movement} + \text{recoil} \\
y^{'}(x_i,t) &= Y_1(x_i,t) + Y_2(x_i,t) \\
y^{'}(x_i,t) &= A(x_i)\cdot\sin(\kappa x_i - \omega t + \epsilon_1^{'}) + B(x_i)\cdot\sin(\omega t + \epsilon_2^{'}) \\
y^{'}(x_i,t) &= (A_0 + A_1 x_i + A_2 x_i^2)\cdot\sin(\kappa x_i - \omega t + \epsilon_1^{'}) + (B_0 + B_1 x_i)\cdot\sin(\omega t + \epsilon_2^{'})
\end{aligned}
\tag{2.3}
$$

expressed with the wave number κ, Angular frequency ω and the phase shift ϵ.

2.3 Mathematical models for fish locomotion

To exploit the fish locomotion motion, a mathematical replica has to be built. Studies show that steady locomotion movement for a BCF type of fish, can be determined as a function in time and space. The method done by Cui et al. [5] is to create a midline motion for a fish, such that a CFD solver can implement and investigate the flow around a 2D fish. Parts of their method and approach is repeated, to illustrate the method on which I will build my thesis. This is done by first defining the amplitude as many waves increasing in horizontal axis.

$$h(x,t) = H(x)\sin(\omega t - \kappa x) = (a_1 + a_2 x + a_3 x^2)\sin(\omega t - \kappa x) \tag{2.4}$$

where ω=2πf is the tail-beat frequency, κ is the wave number, and H(x) is the amplitude envelope, which is parameterized by the amplitude coefficients a_1, a_2 and a_3.

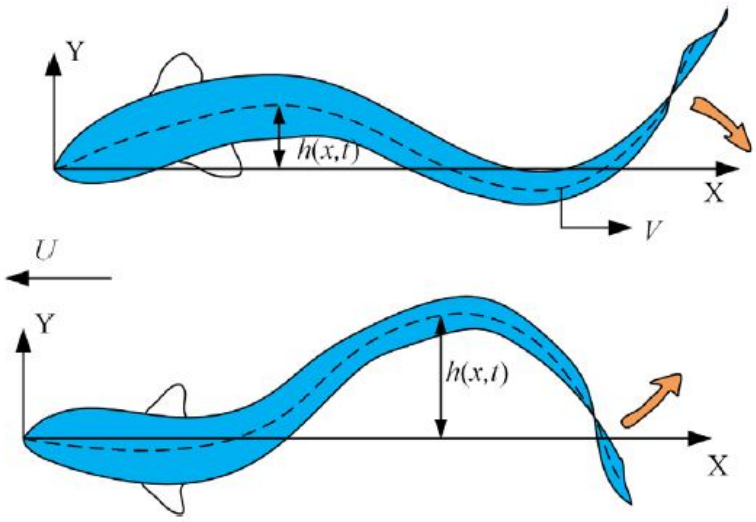

Figure 2.13: Reference frame and variables used to describe the kinematics of swimming fish. Adapted from Cui [5]

The amplitude H(x) is described by a polynomial, which varies with the swimming state.

The wave number is defined by characteristic length, to be able to compare numerical finding to other fish

$$k = 2\pi/\lambda = 2\pi/(s_1 L) \tag{2.5}$$

where λ is the wave length, L is the length of the fish body, and s_1 is a constant.

The envelope magnitude of the lateral fish motion at the head and tail can be normalized as

$$\frac{H(0)}{L} = \frac{a_1}{L} = s_2, \frac{H(0)}{L} = \frac{a_1 + a_2 L + a_3 L^2}{L} = s_3, \tag{2.6}$$

where s_2 and s_3 represent the dimensionless magnitudes of lateral fish motion at the head and tail.

Parameter, s_4, is used to identify the location of the minimum transverse body motion location as

$$(\frac{dH}{dx})_{x=s_4 L} = a_2 + 2a_3 s_4 L = 0 \tag{2.7}$$

This results in dimensionless parameters, which is important in order to be able to implement the function into numerical studies.

$$h(x,t) = (s_2 L + \frac{-2s_4(s_3 - s_2)}{1-2s_4}x + \frac{(s_3 - s_2)}{(1-2s_4)L}x^2) sin(2\pi f t - \frac{2\pi}{s_1 L}x) \tag{2.8}$$

The dimensional position x along the fish body is further replaced by x*L(0≤x*≤1), where x* is a dimensionless position. The dimensionless midline motions of the fish g can be further described as

$$g(x,t) = \frac{h(x,t)}{L} = G(x)\sin(2\pi f t - \frac{2\pi}{s_1}x*), \tag{2.9}$$

$$G(x) = (s_2 + \frac{-2s_4(s_3 - s_2)}{1-2s_4}x* + \frac{(s_3 - s_2)}{(1-2s_4)L}x*^2)). \tag{2.10}$$

The different scaling parameters of the midline motion of BCF fish, is shown in 2.14.

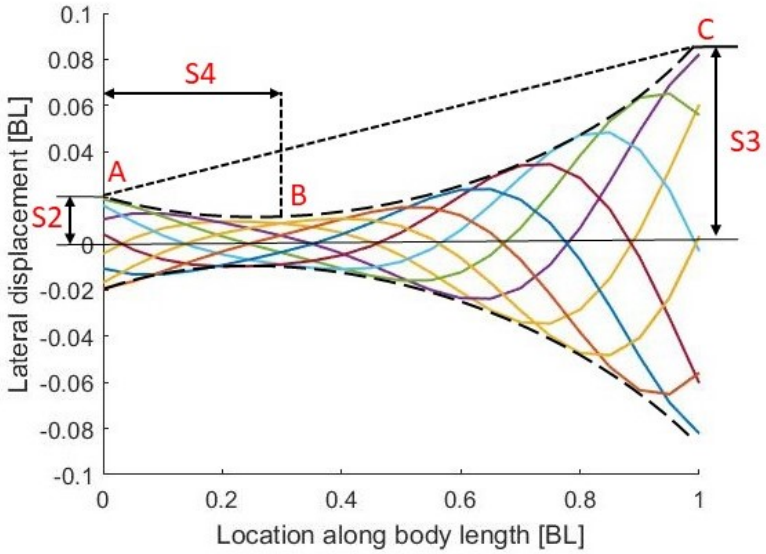

Figure 2.14: The scaling parameters of the midline motion of BCF fish. Inspired from Cui [5]

A table of $s_1, s_2, s_3 and s_4$ for different fishes is included in appendix chapter A

2.4 Numerical studies on swimming modes

To understand the flow structure around a fish, both experimental and numerical studies has to be investigated. The main limitations are the accuracy and the repeatability of experiments. The fish behaves naturally, which for the locomotion result in a bias error. The human aspect of conducting multiple experiments on the same fish and fish in general, reduces repeatability.

Early hydrodynamic models were based on quasi-static approaches, while more resent models deal with more realistic motions, assuming inviscid fluids. These models are 2D elastic foils solving for slender body theory, which for Lighthill's elongated-body theory [12] is suitable for subcarangiform and carangiform fish, where carangiform is better represented by elongate body assumptions. These models are implemented in CFD to solve undulating fish body and/or caudal fin by solving the Navier-Stoked equation. A trade-off between accuracy and computational time has to be made as computational power often limit the complexity, i.e. the resolution of the solution. Thus, the results are limited to the assumptions and how the operator implements the analytical methods.

2.5 Locomotion experiment

Preliminary tests on sea bass locomotion and fast-start phase have been carried out in authorized laboratories within the Centre of Excellence NTNU AMOS in collaboration with the Italian research institute CNR-INM. I have not done nor overseen the experiment my self, but the experimental log and results has be sheared with me by courtesy of Adjunct Professor Claudio Lugni and PhD Candidate Shaojun Ma. The experimental set up and result will be presented, concerns to the first mentioned will be stated, but not further discussed.

The experiment was conducted with an european sea bass and the paralyzed fish is illustrated in figure 2.15. The total length is measured to be 32.5cm ± 1cm. The stride length is measured to be 28.5cm ± 1cm, 0.88 of the total length.

Figure 2.15: The European sea bass, with which the experiment was done. The figure is a courtesy of Adjunct Professor Claudio Lugni

The experiment was carried out in a closed flow tunnel, where an impeller was circulating the water flow through the tank. The impeller forces the water through longitudinal plates when the flow is going in one direction long side, before it is forced through several vertical plates when making the turn, to ensure that the steady flow is kept. The flow passes a Honeycomb filter before entering the inlet part of the tank where the fish is located, before passing the outlet and through vertical plates before coming back to the impeller. The setup of the tank can be seen in figure 2.16 and the image of the experimental set up in figure Figure D.1.

The dimensions of the tank with the fish is:

- width 20cm = 0.62 BL
- height 20cm = 0.62 BL
- length 66cm = 2.09 BL

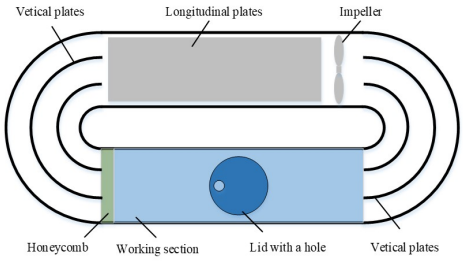

Figure 2.16: The experimental setup. The figure is a courtesy of PhD Candidate Shaojun Ma

The experimental target is to investigate fish hydrodynamics without interaction with the free surface. Hence the closed flow tunnel, representing the underwater condition for which underwater vehicles and robots are operating. The free surface effects is therefor replaced with a wall effect. A lid with a hole located on the top of the tunnel, to insert the fish and to connect the accelerometers and pressure sensors on to the fish.

The fist accelerometer was attach, at 2/3 BL from the head, above the lateral line. The second accelerometers were attached ahead the caudal tail. There was in addition attached one pressure sensor in the front.

To capture the movement of the fish in time, three slow speed high resolution cameras and one high speed low resolution GoPro camera were set up. One slow speed high resolution camera was placed on each side of the tank. The purpose for the these were to verify stable swimming height for the time interval investigated. Two cameras were located at the top, as a top view, one slow speed high resolution camera and one high speed low resolution GoPro camera. The GoPro camera is suppose to takes 100 frames pr. second, but loses 3 out of 4 frames due to a bias error, resulting in 25 frames pr. second. The high resolution camera takes 8 frames pr. second. The most problematic with the camera setup, was that the outline of the hole for inserting the fish was placed between the fish and the camera, as one can see in both figure 3.2. The high resolution cameras are triggered by laser, and has therefor the possibility to give the accurate time, corresponding to the reading from the accelerometer and can therefor potentially be very helpful for post processing the data.

there are two different types of cameras capturing the experiment. There is a high speed low resolution GoPro camera which is suppose to takes 100 frames pr. second and a low speed high resolution camera which takes 8 frames pr. second. The GoPro loses 3 out of 4 frames due to a bias error, resulting in 25 frames pr. second.

Initially, the flow speed was tested in the range 0.5L/sec to 3L/s, which is under and above the assumed cruising speed for the sea bass.

From the experimental log, there is a list of factors that may effect results in different ways. The following are:

- no calibration has been conducted for the new motor that was installed prior to the experiment. This gives rise to unknown uncertainty in flow speed.
- According to the biologist, the flow velocity monitor they are using has an error of 10%.
- The tunnel bottom had a slope, which makes it 1cm higher in the front.
- The accelerometer was attached on the fish with glue.
- It was found that the accelerators had problems of noise.
- It was also found that the noise of the pressure sensors was too high.

- The Pitot was installed ahead of the working tunnel region, meaning that the absolute value of its measurements is not the flow velocity within the working part.
- Based on a CFD analysis carried out by Shaojun Ma, it indicates that the velocity in the tank is not steady. His results show that there is local differences in the flow, which is most present close to the inlet.

Chapter 3

Image processing, midline construction and locomotion extraction

Through this chapter, a review of the image processing, midline construction and locomotion extraction will be presented. This chapter builds on my project thesis. Possible error sources have been identified and improved, and thus sections from the project thesis is integrated and/or enlarged.

In effort to investigate the fish locomotion numerically, images combined with mathematical methods are used. Images from the experiment are used to match the fish motion. These images are used to build a function of the midline in time. The function is further separated into a recoil and a lateral motion, to investigate the effects of the lateral motion individually.

3.1 Fish identification by image processing

Image processing is used to separate the fish from the background. The experiment on which this thesis is based, has limitations as mentioned in section 2.5. These limitations limit the reconstruction of the fish to a short duration of 2D top view swimming. The main challenge for the image processing, is to compensate for the camera setup. The top view cameras were as previously mentioned placed above the upper transparent panel. The outline for the hole, for inserting the fish, is in the center of the panel, thus it is between the fish and the lens as see in figure 3.2. It is for this reason not possible to directly identify the fish, thus a more comprehensive image processing and analysis have to be carried out.

After a thorough investigation of the former image processing preformed in the project thesis, it was found that the fish length was not properly reconstructed for every time step, as shown in figure 3.5. It was further found that the Fast Fourier Transform (FFT), which constructs the fish motion, is highly sensitive to having an exact replication of the fish length. The FFT is therefore also sensitive to a rough outline of the fish, as it is directly cobbled with the initial midline of the fish and makes the midline longer than in reality. To overcome this combined challenge, a semi-automatic iterative image possess has been developed.

3.1.1 Video selection

As already mentioned in section 2.5, two top view cameras have recorded the experiment. The criteria for selecting the video use for the analysis is listed below in an ascending order.

- Flow velocity
- Stable swimming
- Recorded frame rate
- Duration of time sequence

- Clarity of images

Comparing the GoPro image and the high resolution image, shown in figure 3.1, one can see that there are a lot of noise in the GoPro image, meaning that the fish in itself is neither howl nor clear. The outline of the hole for which the fish is inserted, is the circle visually dividing the fish into two parts. The GoPro camera captures the caudal peduncle poorly and the caudal fin even worse. Additionally the accelerometer are reattached with glue several times, resulting in a discolored white area at the connection points. These challenges makes it difficult to distinguish the fish from the background. The 2D top view projection of the body do not capture the main axis for the the tail region, as the caudal fin has a 3D effect, resulting in a visualized layered fin, shown in the high resolution image 3.1. The wire also visually interferes with the tail. All these forth mentioned challenges combined makes the reconstruction especially challenging in the tail region.

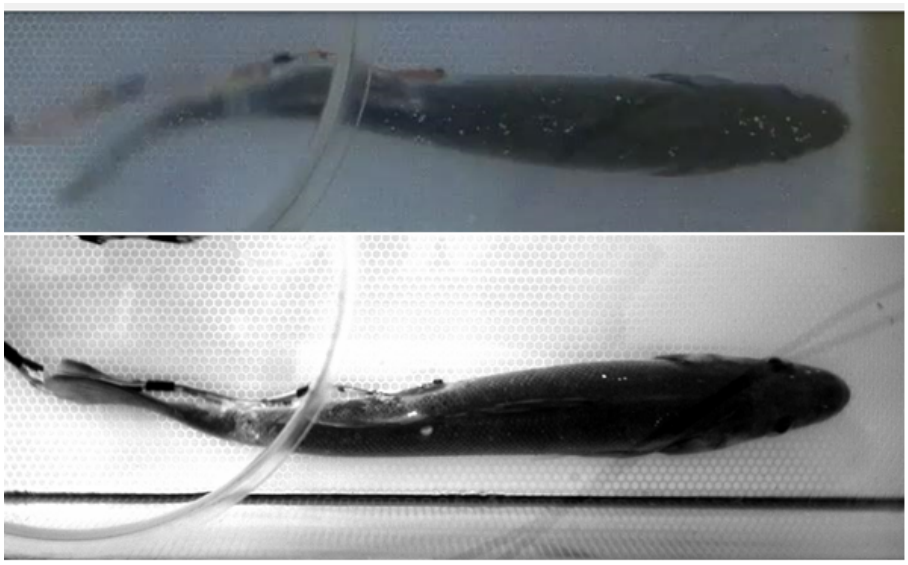

Figure 3.1: Initial image, before reconstruction

In the project thesis the GoPro video which had previously been analyzed by co supervisor Adjunct Professor Claudio Lugni was chosen. This was video was chosen in order to verify my result, against his 70 manually chosen outline points. Finding from my project thesis indicates that the video chosen, was recording an unsteady swimming motion, where the fish had the tendency to accelerate. This acceleration gave raise to changes in frequency and motion, thus directly affecting the FFT reconstruction of the fish in time.

For this thesis the GoPro video shown in figure 3.2 has been chosen. The video selection was based on finding the longest sequence of stable swimming, while keeping the remaining criteria in mind. This was done to get the real tendency, which the same beat frequency to minimize the effect of acceleration. The slow speed high resolution camera was not considered, as it was not able to capture a sufficient amount of images, during a period of swimming speed between 1 to 3 BL/s.

The video analysed:

- 25 frames pr. sec
- 113 frames
- Video format: RGB24
- Pixel size: 1080x1920
- Impeller : 408 rpm
- $U = 1BL/s$

- $Re = \frac{UL}{\nu} = 1.05099 \cdot 10^5$

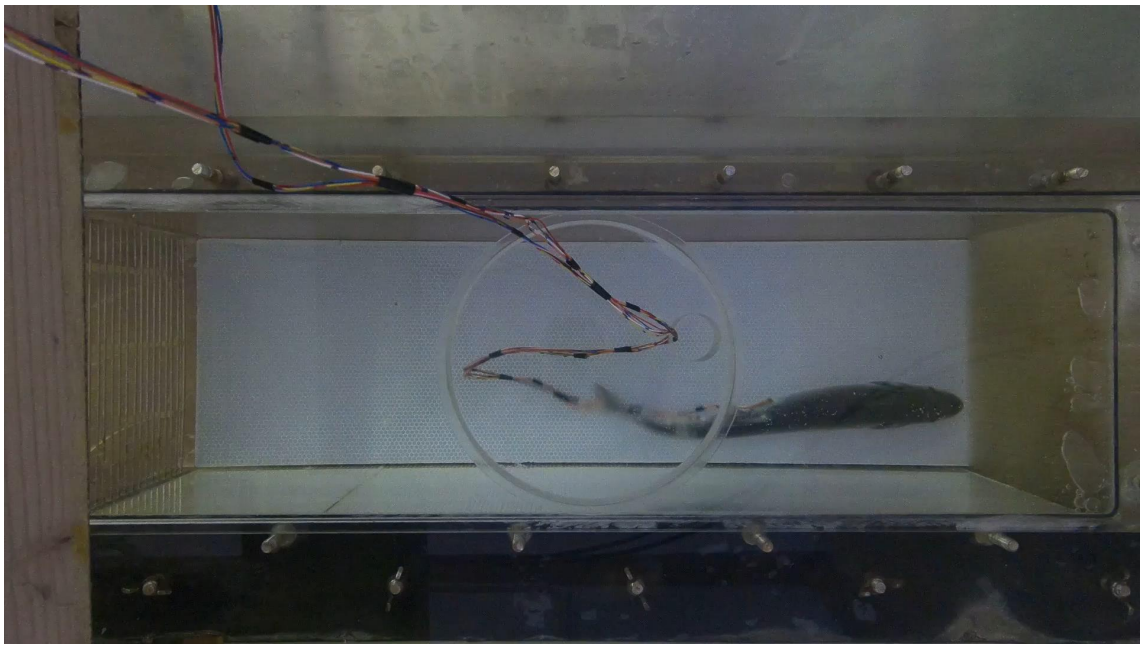

Figure 3.2: Untreated GoPro frame

3.1.2 Image initialization

Before proceeding with the semi-automatic iterative process, an initial rough filter without losing information is applied. This filter is done manually, by checking every color value on the fish against the background. Every color value that is not associated with the fish is then filtered out.

The image is then cropped into a 196x755 pixle frame, as shown in figure 3.3, to minimize the interference between the background and the fish it self.

Figure 3.3: The cropped image

The cropped image is separated into red, green and blue colored RGB matrices. RGB has values between 0 and 255, and each matrix are imported into Excel. In Excel the different color values for each matrix are distinguish from bright red to bright green, as indicated in figure 3.4. To minimise the interference with the background, only the visually color ranges on the fish is chosen. The remaining color values are discard and forced to be bright green, value 255, meaning that they will not interfere with the red fish. These new RGB matrices are merge together again, and the chosen colors are indicated as the blue color in figure 3.1.3. The image is then gray scaled to make the image easier to work with.

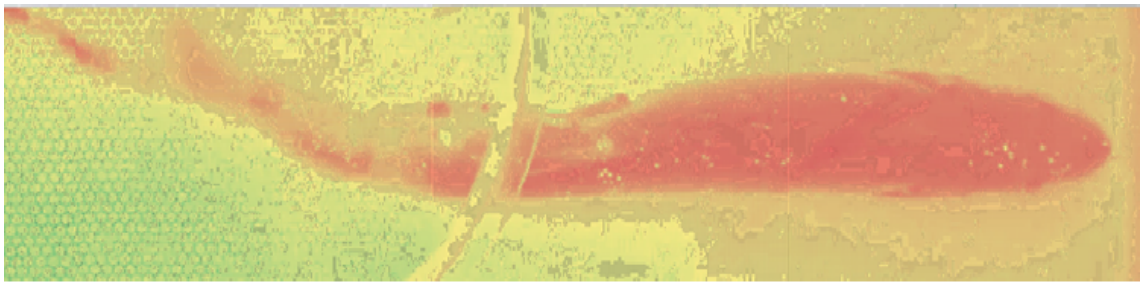

Figure 3.4: The red color values in excel from 0(red) - 255(green)

3.1.3 Semi-automatic iterative processing

A semi-automatic iterative cleaning processing is performed to overcome the challenges connected to the low resolution of the GoPro camera, combined with the blending background. These challenges makes it difficult to separate the fish from the background, as shown in figure 3.1. This initiates for a more comprehensive cleaning process, where each part of the fish has to be treated separately.

Findings form the project thesis as forth mentioned, indicates that the FFT is sensitive to fish lengths shorter then the actual fish length. The separation of the fish from the background performed in the project thesis, was done by first removing the same gray tones from the entire image similar to the RGB selection above, before applying the reaming filters. The result was that parts of the tail, for certain time frames, was lost as illustrated in figure 3.5.

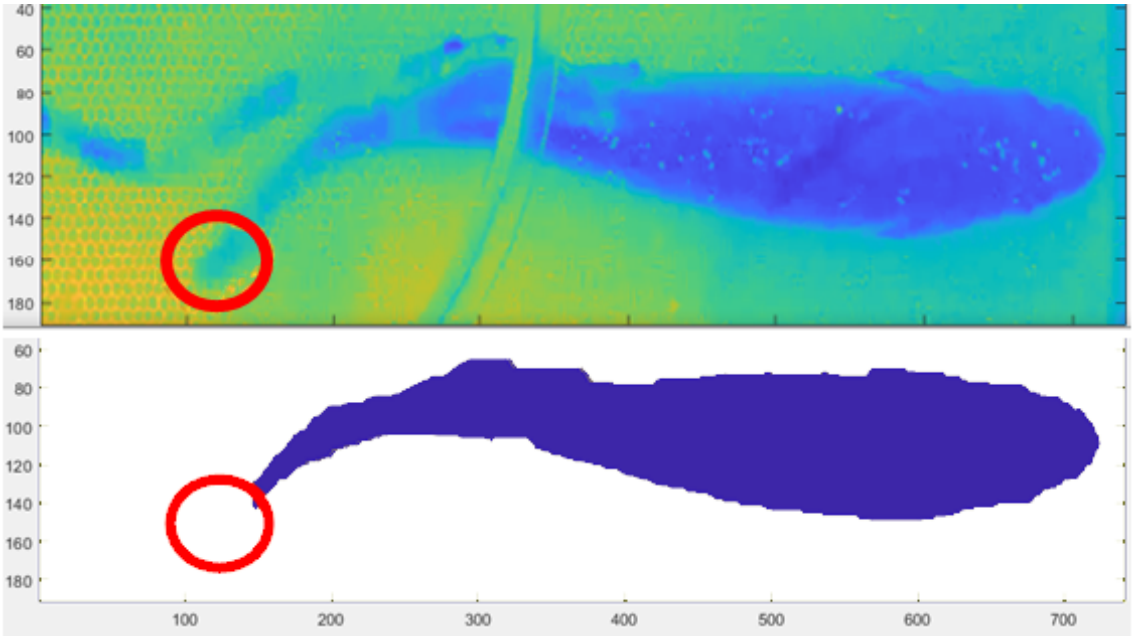

Figure 3.5: The myred circles indicates the tail in the upper image and the lost tail by using the method in the project thesis in the lower image

Every image spaced with an exact swimming period in time has a similar reconstruction challenge. Within a period, every image has to be treated individually. When the fish changes position, the amount of interference with the wire and the sharpness of the tail is differs. To overcome these challenges, a semi-automatic image cleaning code is used.

To ensure that the entire fish length is reconstructed, a reference fish length is initially calculated from a chosen image. The reference image is reconstructed manually, shown in figure 3.6, and the calculated fish length in pixels is now the verification parameter for the iterative code.

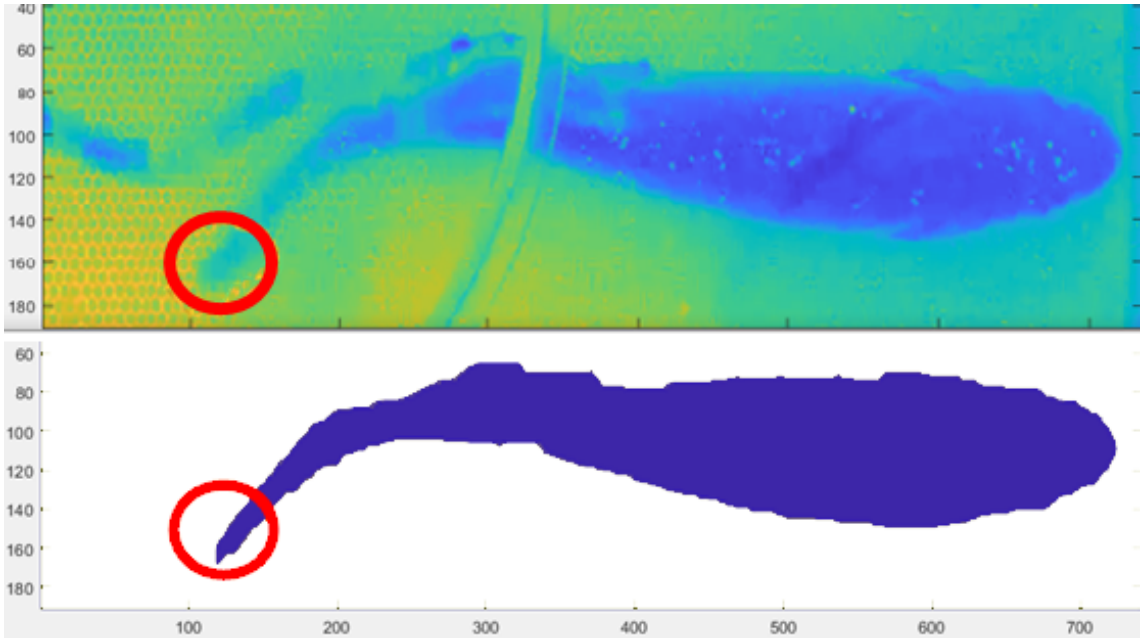

Figure 3.6: The red circles indicates the tail in the upper image and the proper reconstructed tail by manually choosing filters in the lower image

Additional restraints is applied to make sure that the length measured is only the fish and not the background. The iterative procedure is shown in the the flowchart 3.7.

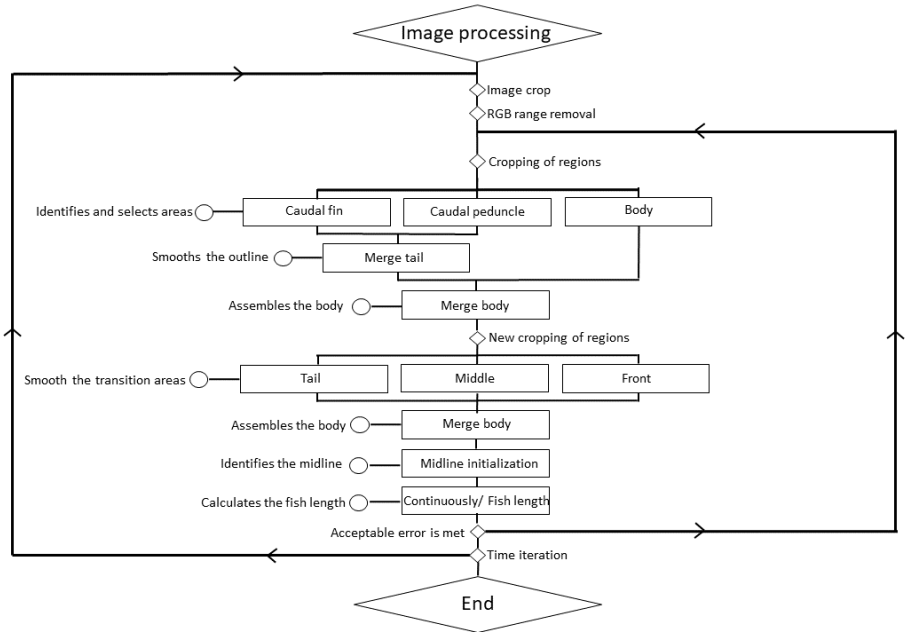

Figure 3.7: Removes all color values over 85.

Establishing regions

From the image initialization the image is cropped and the majority of the colors from the background is removed. To further identify the fish in the gray scaled image, gray tones from the image is removed. The gray tones are distributed between 0 to 255, where 0 is black and 255 is white. If the same gray tone range for the entire image is discard, the result would be that either parts of the fish or the entire fish with additional background noise would be reconstructed, as shown in figure 3.8.

Figure 3.8: All gray tones above 50, 85 and 100 are discarded respectively from top to bottom.

The semi-automatic iterative image cleaning code, takes advantage of this change by dividing the fish into regions and cleansing them separately. The regions are divided based one the resolution of the fish relative to the background, as illustrated in figure 3.8. As aforementioned the caudal peduncle is poorly resolved and the caudal fin even worse, while the main body is better. The resolution is directly cobbled with how fast every body part moves. The fish will blend into the background if the motion it to high, see figure 3.1. Thus the regions are divided into caudal fin, caudal peduncle to the cut off and the main body, see figure 3.9.

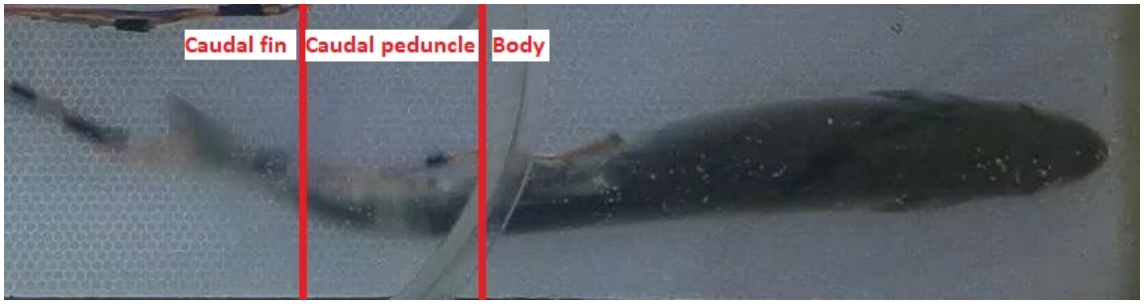

Figure 3.9: The regions are divided in caudal fin, caudal peduncle and body respectively from blurry to sharp.

Caudal fin, caudal peduncle and body

The fish is now divided into three parts. To visualize the gray scaled tones more clearly the scale is shown as white = yellow and black = blue.

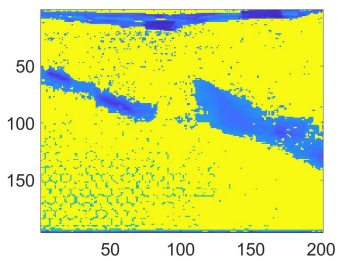

Figure 3.10: RBG cleansed caudal fin region, in pixels

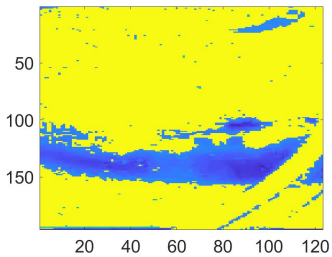

Figure 3.11: RBG cleansed caudal peduncle region, in pixels

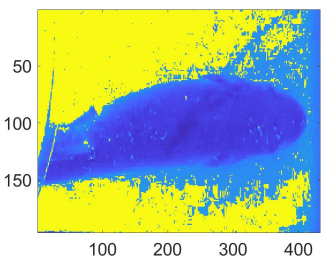

Figure 3.12: RBG cleansed body region, in pixels

To obtain the midline in each area, it is essential to remove all smaller areas of background noise, see 3.1.3. As aforementioned, the most challenging region to reconstruct is the fin. This region is therefor the only region cobbled to the iteration parameter. The iterative parameter is cobbled to the removed gray tone value.

The image is converted to logical 1 (true, yellow) and logical 0 (false, purple). The iterative parameter is the highest gray tone value that is false and all gray tones above this value is true. This means that for every iteration brighter tones are included in false. Larger parts of the fish will be included for every iteration. This is because the tail is merged whiter with the background towards the tail, as the amplitude increases and the relative horizontal speed as well. When including brighter and brighter gray tones, the false region will eventually capture the entire fish, see figure 3.1.3.

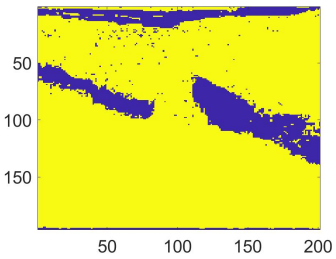

Figure 3.13: All gray scale values above 98 is removed.

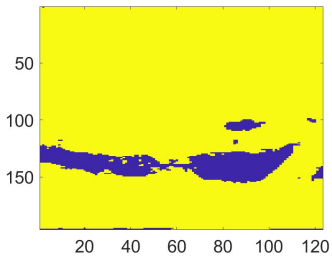

Figure 3.14: All gray scale values above 82 is removed.

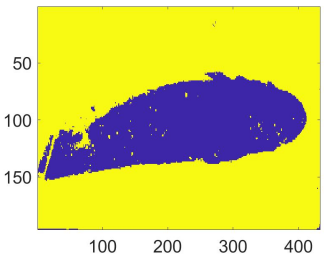

Figure 3.15: All gray scale values above 70 is removed.

Dark areas are sorted in size, and all areas less than a defined numbers of pixels are removed, as shown in figure 3.1.3. The image is once again converted to logical 1 (true, yellow) and logical 0 (false, purple). All dark areas with smaller then the defined number of pixels are now false. Areas smaller then this are considemyred noise. For the caudal fin larger and larger clusters of areas will evolve, throughout the iteration, until they become large enough to appear. The tail will then keep growing in size and eventually merge together with the wire. This is not ideal, and the goal is to stop the iteration process before this happens.

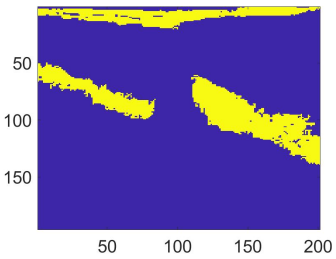

Figure 3.16: Areas less than 800 pixels are removed.

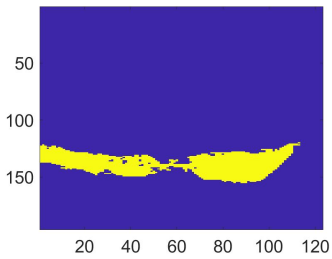

Figure 3.17: Areas less than 600 pixels are removed.

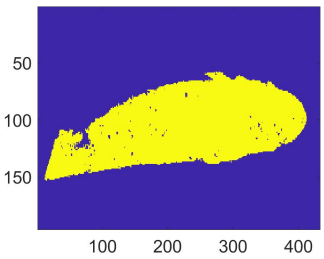

Figure 3.18: Areas less than 2000 pixels are removed.

Before converting the logical matrix back to a binary image, it first has to be converted to a matrix of double precision. To ensure that fish do not have gaps in dark areas, a disk-shaped structuring element is create. The disk structuring element with radius of 5 pixels is specified. A morphological close operation is perform on the image, to fill the gaps based on the disk-shaped structuring element. The disk-shaped structure goes pixel by pixel through the entire image, and when it identifies that more then 50 percent of the pixels in the disk is black, then it gives the remanding pixel in the disk the value black, as shown in figure 3.1.3. The color representing logical 1 is changes to (true, white).

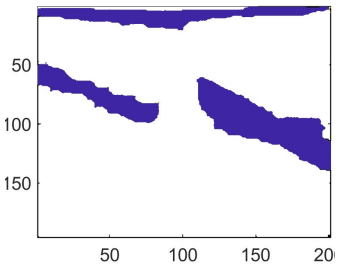

Figure 3.19: Morphological close operation with disk-shaped of radius 5.

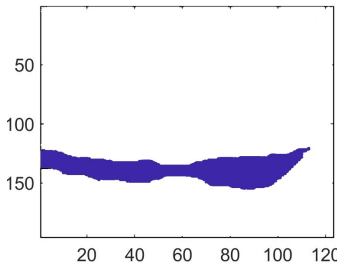

Figure 3.20: Morphological close operation with disk-shaped of radius 6.

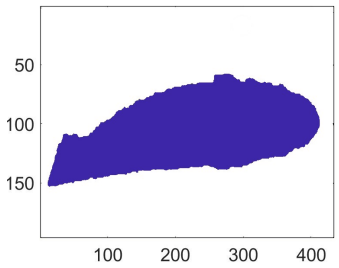

Figure 3.21: Morphological close operation with disk-shaped of radius 5.

Numbers of appeared areas may be several depending on the image. All different areas are numbered to associated area in stead of binary values. Knowing that the tail is attached to the frame, identified areas are attached to the wall. Then a zero matrix is created and the associated area number to the tail is defined as logical value 0, and remaining background 1, to make it binary. The selected tail part is separated from the remaining areas in figure 3.1.3.

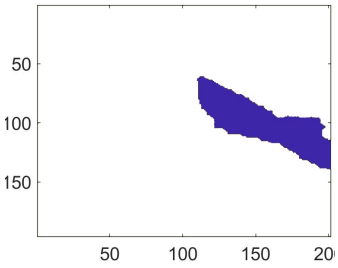

Figure 3.22: The tail is selected from the remaining areas and the image inverted.

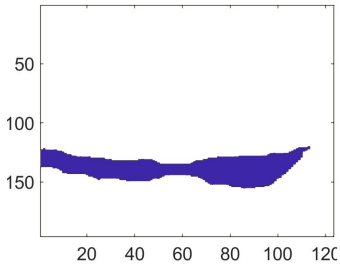

Figure 3.23: The image is inverted.

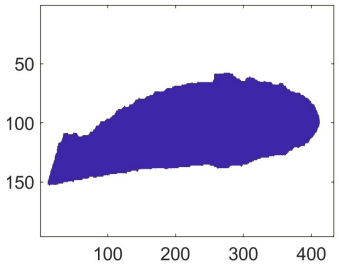

Figure 3.24: The image is inverted.

Merging caudal fin and caudal peduncle

The caudal fin and caudal peduncle regions are merged. They are merged separate from the body because the surface from the reconstruction is rougher. To smooth the surface, a disk-shaped structuring element is create. The disk structuring element with radius of 14 pixels is specified. A morphological opening operation is perform on the image, to remove edges based on the disk-shaped structuring element. The disk-shaped structure goes pixel by pixel through the entire image, and when it identifies that the disk is not initially black, then it makes all the pixel in the disk white, as shown in figure 3.1.3. Thus making the black region shrinking in size and the surface smooth.

Figure 3.25: The merged caudal fin and caudal peduncle.

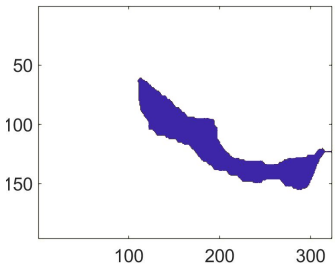

Figure 3.26: Morphological open operation with disk-shaped of radius 14.

Merging tail and body

The tail and body is merge shown in figure 3.27, to divide the fish into new regions.

Figure 3.27: Merged tail and body

New established regions

The new regions are divided such that the previous connection points between the caudal fin, caudal peduncle and body is now in the center of the regions, shown in figure 3.1.3. This allows the previous regions to merge smoother together.

Figure 3.28: The new tail region.

Figure 3.29: The new middle region.

Figure 3.30: The new front region.

The most crucial region to smooth is the middle region between the caudal peduncle and the body. The disk-shaped structuring element created for closing this gap is given a radius of 27 pixels. The tail and the leading body is given respectively 14 and 6, to smooth the attached areas, as shown in figure 3.1.3. A morphological close operation is perform on the image, to fill the gaps based on the disk-shaped structuring element.

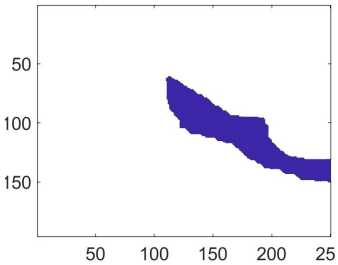

Figure 3.31: Morphological close operation with disk-shaped of radius 14.

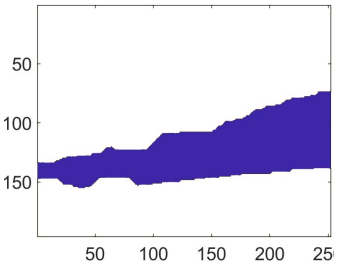

Figure 3.32: Morphological close operation with disk-shaped of radius 27.

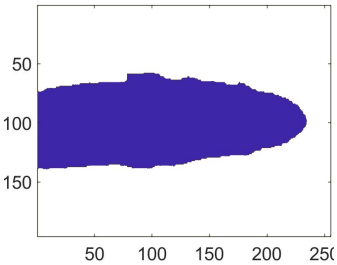

Figure 3.33: Morphological close operation with disk-shaped of radius 6.

Reconstructing fish

After smoothing the outline of the fish regions, they are simply merge together and the fish is now reconstructed. Logical 1 (true, white) and the logical 0 (false, purple), is coveted to binary values.

Figure 3.34: Reconstructed binary image of the fish (black).

Verification of the reconstruction

To ensure that the reconstructed fish has the same length as the real fish, the midline is obtained and the midline length is calculated. The procedure for the midline construction is explained in section 3.2.

To ensure that midline is continuous, the initial midline is checked. Every midline pixel from the head and back is checked. If the midline is not reconstructed a not a number (NAN) will replace the midline value. The continuous check stops when the check comes to a NAN, which is a gap or the end of the fish tail. The midline up until this point is saved as the new midline and if there are any remaining midline points, whey will by discarded.

The fish length is calculated from the new continuous midline. Based on the fish length and the number of iteration ran, an acceptable solution is found. The iterative process will continue until this acceptable error is met. When an acceptable error is met, the midline reconstruction will continue for the next time step. The reconstructed midline length have,

- Mean fish length: 651.63 pixels
- Standard deviation: 14.21 pixels

and visual inspection 3.35 and B.17 indicates that the midline length properly reconstructed.

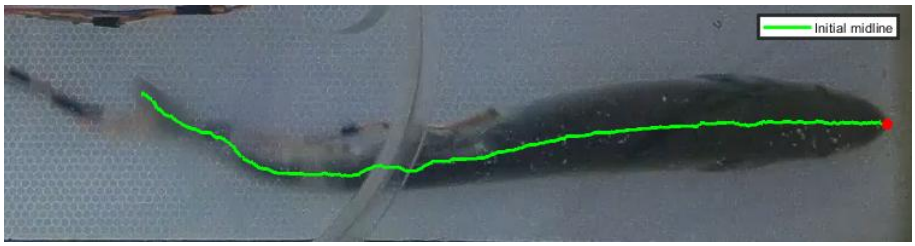

Figure 3.35: Visual midline verification

3.2 Midline construction by curve fitting

The coordinate values should preferentially be non-dimensionalized to make it easier to work with. It is also beneficial when using the constructed function for numerical simulations. The pixel dimensional position X_f along the fish body is further replaced by x, where x is the dimensionless position.

$$\begin{aligned} x &= X_f / BL\,[-] \\ y &= Y_f / BL\,[-] \end{aligned} \tag{3.1}$$

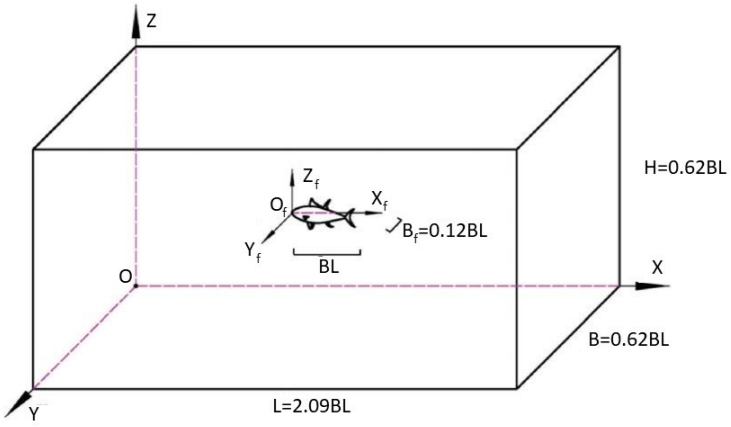

Figure 3.36: Coordinate system for the experimental set up.

The reconstructed outline from the midline reconstruction of the fish is not smooth, as shown in figure 3.34. Consequently the midline can not be found directly from the reconstructed image. From the reconstructed image, the initial midline is found based on the outline of the fish. The midline is corrected by curve fitting methods. To replicate the fish motion, two methods are used. Firstly a strongly simplified Fast Fourier Transform (FFT) is performed, before a Least Square Method (LSM) is performed. For the first method, all midlines are processed through a FFT. Secondly a direct method, LSM, which used the points in space and time directly.

3.2.1 Midline initialization

Before imposing curve fitting methods to the initial midline, the midline has to be identified.

Identifying the initial midlines

The reconstructed image of the fish is not smooth. To construct the midline the sea bass is assumed top view symmetrical about the spline. The initial midline is therefor chosen as the midpoints between the outline tracing of the fish, in the flow direction. The binary image is white for background pixels and black for pixels of the fish. The row is define in the flow direction and the column normal to the flow. The initial midline is found by first identifying the value where the column pixel changes from white to black and vice versa. The midline point is then found by taking the middle pixel value between these two points. The midline is created by repeating this for all the columns. The green line in 3.37 illustrates an initial midline.

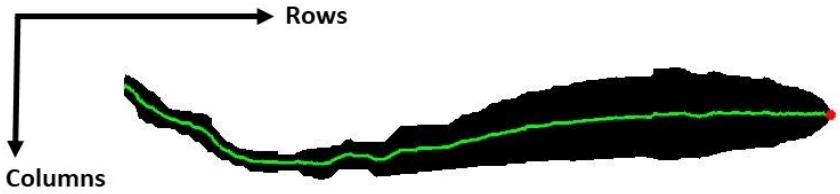

Figure 3.37: The midline retrieved from the the cleaned image

Initializing the initial midlines

The identified midline is in pixels and the initial midline vector length is the total number of rows in the image. Every point in this vector is associated with either a midline value or a NAN value. A new midline vector without NAN values is created. The length of the new midline vector changes as the fish changes curvature. The length of the midline vector is the number midline value points. It is assumed that for a steady case, the fish has a fixed Center of Mass(CoM) position in the flow direction. This assumption is acceptable as the objective of this thesis is to investigating steady swimming. The CoM position changes in time, and the position is not possible to directly retrieve for the 2D case. It is therefor further assumed that the fish head is fixed in flow direction. The column number for the fish head pixel point value, is therefor identified, as indicated with a red dot in 3.37.

3.2.2 Curve fitting

The midline obtained directly from the image reconstruction, is not smooth as aforementioned. It is assumed that the midline is following the spine of the fish and is therefor a smooth curved line. It is further assumed that the spline length is constant, meaning that it is not contraction nor expanding. From figure 3.34, it is visible that the outline of the fish is rough, thus the midline is rough. From the assumption of the midline as a smooth curved line, this error has to be correct. The correction is done by evaluating different curve fitting methods and choosing the best fit.

Cure fitting methods

The midlines are input for FFT, a method where a time sequence for points on the fish are evaluated. It is crucial that the same point on the fish is evaluated in time and that these points are the actual points on the fish. The first and last evaluated point is the far end of the head and the tail respectively. It is therefor essential to ensure that the head and the tail region are well imposed. The tail is the region that has the largest uncertainty, it is therefor desirable to minimize further error in this region. Additionally, two important features for how the flow act around an object, is how the flow interact with the form of the object and how the flow leaves the body. To ensure that the midlines are replicated well, a set of criteria are used to evaluated the different curve fitting methods.

The criteria for selecting the curve fitting method is listed below in an ascending order.

- Capture the tendency
- Capture exit angle
- Capture entry angle
- Capture body curve
- It is a smooth curve

Matlab has multiple options for cure fitting and in table 3.1, a selection of curve fitting methods is compared.

Table 3.1: Overview of precision error for the shear force amplitude. The single measurement is taken as run number 5.

Names	Smooth	Capture body	Capture exit	Capture entry	Capture tendency
Pchip(15 points)	no	yes	yes	yes	yes
Pchip(21 points)	no	yes	no	yes	no
Pchip(31 points)	no	yes	no	yes	no
movmean[20 20]	no	yes	no	yes	yes
movmean[20 20] + Pchip(15)	no	yes	yes/no	yes	yes
movmean[20 20] + Pchip(21)	yes/no	yes	yes/no	yes	yes
movmean[20 20] + Pchip(31)	no	yes	yes/no	yes	yes
smoothingspline(SmoothingParam=0.995)	yes	yes	no	yes	yes
sin4	no	no	yes/no	no	no
rat25	yes	no	no	no	yes
rat33	yes	yes	no	no	yes
rat05	yes	yes	no	no	yes
rat15	yes	yes	no	yes	yes
rat35	yes	yes	no	no	yes
gauss2	yes	no	no	no	no
gauss2 + Pchip(15 points)	yes	no	no	no	no
Polyval	yes	no	no	no	no

Based on the criteria for selecting a curve fitting method, a combination of the method movemean and Pchip is chosen. The Pchip is a linearized method where several exact percentage point on the original curve i chosen and connected linearly. The advantage of a linear method is that local changes dose not affect the smooth midline. The disadvantage is that points can be chosen at local peeks, giving local error to mush influence, resulting in a rougher inaccurate global midline. This error is visual for Pchip between 0.2 BL and 0.3 BL in figure 3.38. Despite the possibility of evaluating the midline at a point deviating from the smooth midline, Pchip has the advantage that it dose not try to fit curves to a higher order form. This is an advantage for the uncertain tail region, where the risk of imposing tendencies that incorrect are larger. To reduce further error in the tail region, it is desirable to base the midline directly on the initial midline. To improve the Pchip method, movmean is introduced. Movmean flattens out the initial midline and reduces the influence of local peaks. The movmean for this case, flattens the curve based on the 20 closes points in each direction. Evaluating Pchip for the movmean is more robust, and more importantly the issues of sampling the exact initial midline points for the FFT is take care of.

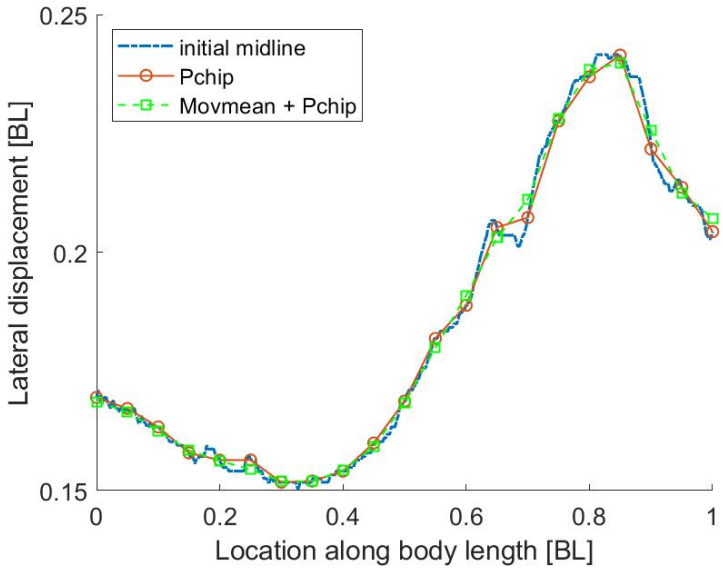

Figure 3.38: The midline retrieved from the the cleaned image

Movmean and Pchip implementation

Movmean is not in it self smooth, but smooths out the already excising curvature. Movmean is uses directly on the initial midline points. It is computing the mean with a window of length $20+20+1$ in this case, that includes the element in the current position, 20 elements backward, and 20 elements forward. After having flatten the initial curve, a vector that indicated how long the fish is up until each pixel point of the midline is calculated. This calculation assume a linear relation between each pixel point. The last point on this new vector states the fish length in pixels.

Based on the new length vector and the fish length, the new length vector is made dimensionless with respect to the entire fish length. Now the percentage length of the fish for every corresponding initial midline pixel value point is found. The movmean midline is then made dimensionless with respect to the fish length, before applying Pchip. The Pchip is applied by finding the percentage points from the corresponding pixel midline. Based on this relation 21 evenly spaced points from 0, the head, to 1, the tail, with corresponding position points in time is found.

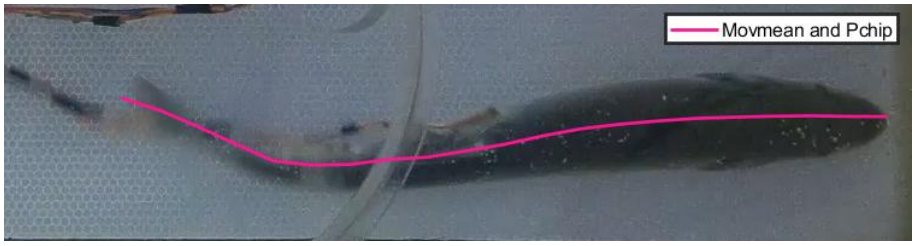

Figure 3.39: The initial midline, Pchip and Movmean with Pchip

Fast Fourier Transform

Fast Fourier transform is creating a strongly simplified function of the fish motion. It linearize every point in time and only considers the dominating frequency. Then choosing numbers of points to evaluate it is impotent to consider what the quality of the input is. In this case the input as the initial midline, is not very good, and fewer points are chosen.

The FFT is used to obtain the amplitude, frequency and the wave number combined with the phase. From the combination of movmean and Pchip, 21 evenly spaced points on the fish with corresponding values is found for all image frames. The input for the FFT is each point position in time. The target is to investigate steady swimming, but the fish is not swimming steady, this additional information is assumed to be noise. To filter out this noise detrend is used.

Detrend identifies the best straight-fit line from the data in time. Detrend subtracts the trend from the elements in time. The strait-fitted trend line is shown in figure 3.40, and the reconstructed signal is illustrated as lateral displacement without trend. The signal used for the FFT, is the one with mean equal zero. The removed information is saved for verifying the FFT function.

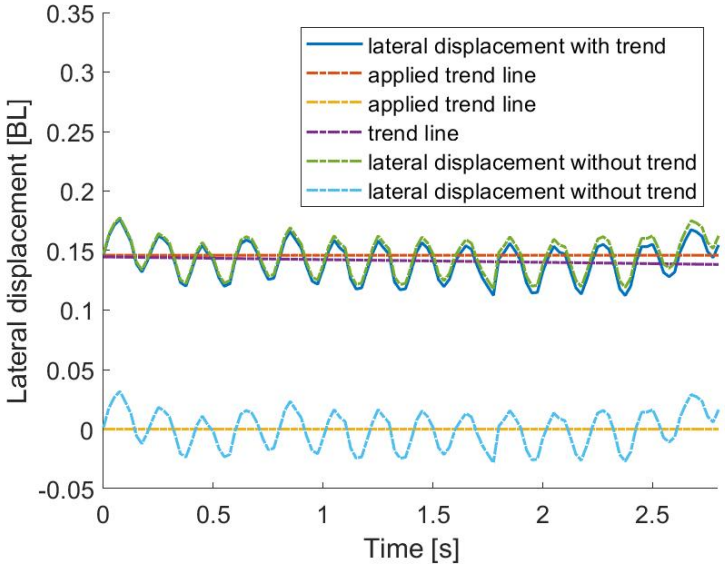

Figure 3.40: The polynomial curve fitting of the image midline

To ensure that the Fast Fourier transform is able to reconstruct the trend good, the input signal should start and stop at two phase shifted points and located close to the midline. The influence of this problem, is minimize by evaluation more periods, in this case 14 periods is considered. The verification of having implemented the transform correctly is shown in Section C.1, 13/20 BL point in time is illustrated in figure 3.41.

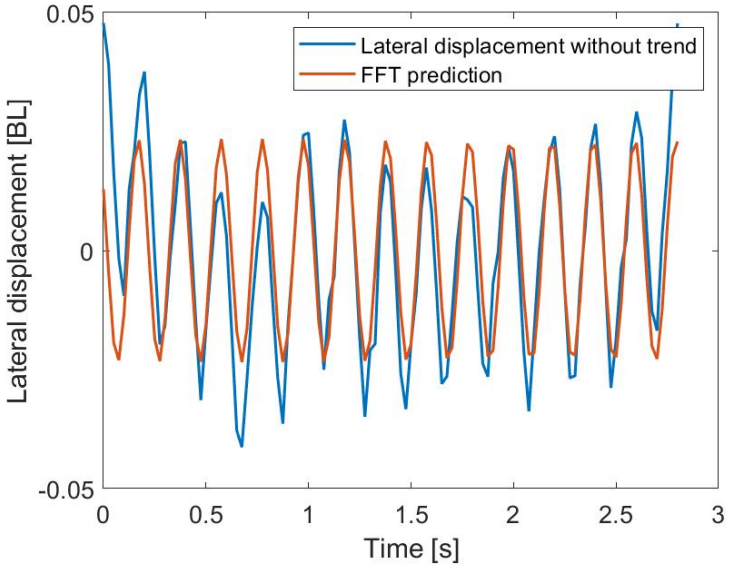

Figure 3.41: The comparison between the amplitude of the 0.6 BL in time and the corespondent Fast Fourier Transform

The dominating frequency is found by looking at the plot of the maximum amplitude for the 21 points form the Fast Fourier transform and retrieving the corresponding frequency. figure 3.42 indicates that most amplitudes is associated with the frequency 4.9558 Hz and a lager minority is associated with the frequency 1.0619 Hz. With the target of separating the fish motion into locomotion and recoil, it is convenient to only consider the domination frequency by assumed that the dominating frequency alone represents the fish motion.

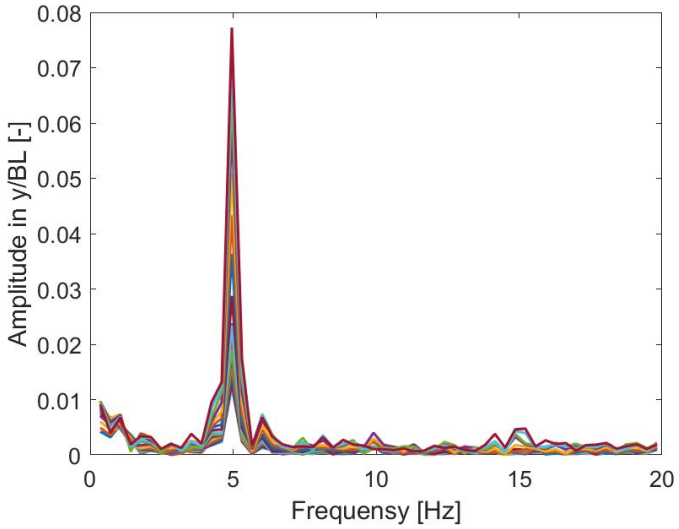

Figure 3.42: The plot indicates that 4.9558 Hz is most dominating for the Fast Fourier Transform

The corresponding amplitudes to the dominating frequency is identified for the 21 evenly spaced points, illustrated as points in figure 3.43. To be able to evaluate more points than the known 21 points from the FFT, a curve fitting method is used. Based on the known points a second order polynomial is curve fitted through the points, illustrated as the line in figure 3.43 and given by the function,

$$Amp(x) = 0.1365x^2 - 0.07703x + 0.02419. \tag{3.2}$$

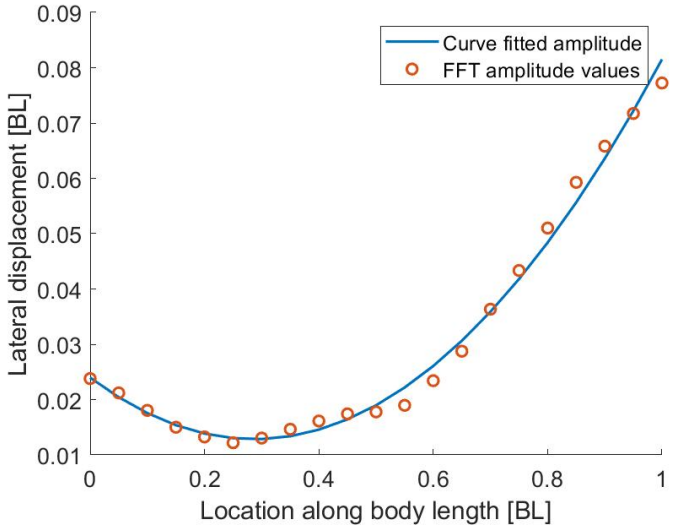

Figure 3.43: The amplitude points for the 21 evaluated points with frequency 4.9558 Hz and the estimated curved fitted line

The corresponding wave number combined with the phase shift to the dominating frequency is identified for 21 chosen points in time, illustrated as points in figure 3.44. when plotting the points, a non-physical phase shift interfered with the plot around 0.24 BL, 2π was therefor added to every point before the phase shift. A third order polynomial was then curve fitted through the points, illustrated as the line in figure 3.44 and given by the function,

$$Pm(x) = 5.132x^3 - 7.651x^2 - 3.911x + 5.074. \tag{3.3}$$

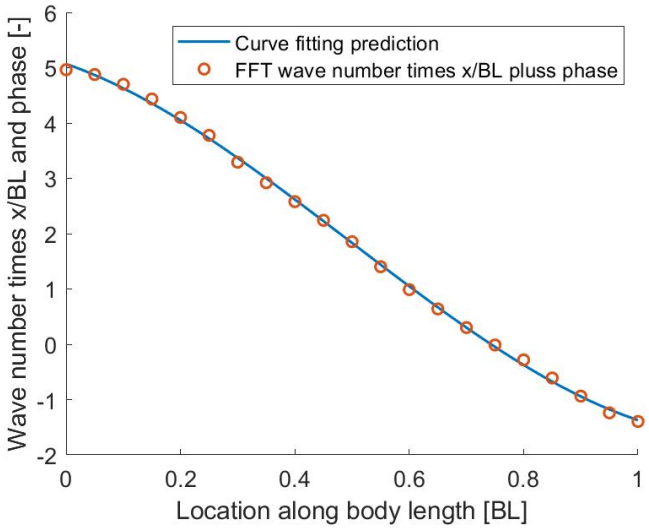

Figure 3.44: The wave number combined with the phase shift points for the 21 evaluated points with frequency 4.9558 Hz and the estimated curved fitted line

The steady motion of the fish is represented, as

$$Y(x,t) = Amp(x) \cdot \cos(2\pi fr \cdot t + Pm(x)) \tag{3.4}$$

$$Y(x,t) = (0.1365x^2 - 0.0770x + 0.0242) \cdot \cos(2\pi 4.9558t + (5.132x^3 - 7.651x^2 - 3.911x + 5.074)) \tag{3.5}$$

The function plotted in space at different time steps is seen in figure 3.45.

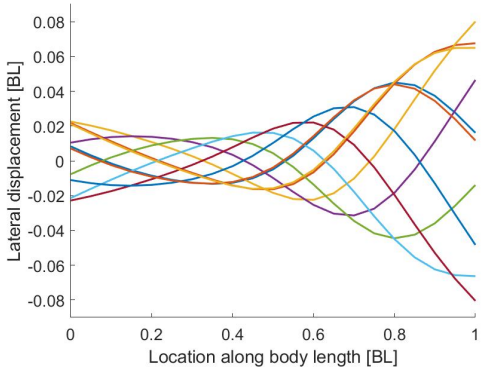

Figure 3.45: function of the midline motion in space for 10 time steps

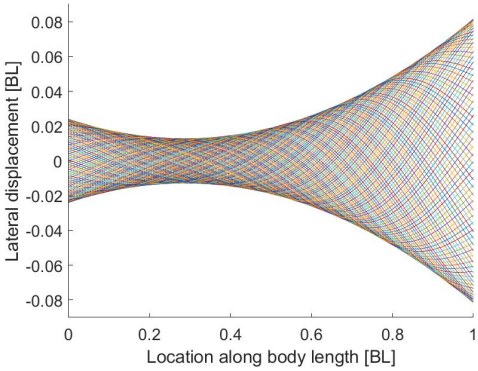

Figure 3.46: function of the midline motion in space for 113 time steps

The wave length, λ, is found by plotting the cosine function with unitary amplitude at different time instants as a function of x/BL. Then $(x_{max} - x_{min})/BL$ from the plots is estimated for each curve and the average is made to get an estimation of half of the wavelength.

$$\cos(2\pi f \cdot t + Pm(x)). \tag{3.6}$$

The evaluated maximas is shown in figure3.47. The mean value of λ is 0.8578 BL, with standard deviation of 0.0348 BL. This agrees well with the expected λ between 0.6 BL and 1.2 BL.

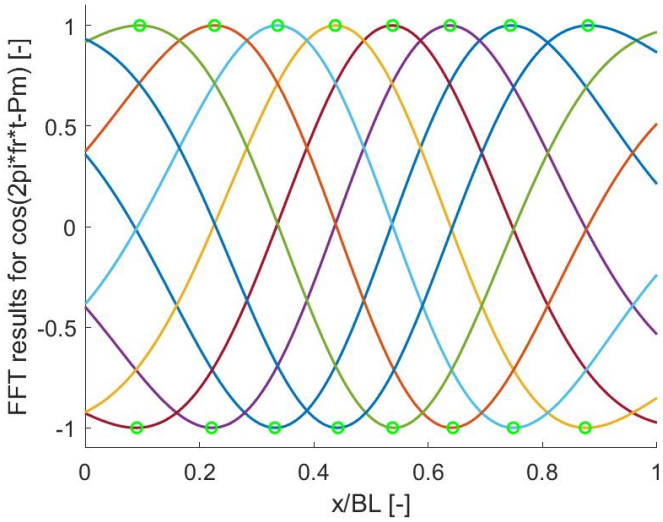

Figure 3.47: The cosinus function for the fish motion, used to find λ

The Wave number, κ, is,

$$\kappa = 2\pi/\lambda = 7.325\ [BL^{-1}]. \tag{3.7}$$

3.2.3 Verification of reconstructed fish motion

To verify if the FFT derived function represents the actual fish motion, the acquired detrend is added to the function and plotted against the image for each corresponding time steps. It can be seen from the comparison in figure 3.51.

$$s1 = \lambda\ [BL] \tag{3.8}$$

A selection of the travelling index of BCF fish analyzed from the biological data, brought together by Cui et al. [5] is in table Section 3.2.3. The different scaling parameters of the midline motion of BCF fish are color coded with reference to the FFT functions scaling parameters. The bold is the reference, the yellow indicates parameters close to the reverence and the green indicated the two BCF fish that fits the FFT functon best.

Fish names	Fish categories	s_2(BL)	s_3(BL)	s_4(BL)	λ(BL)
FFT function	**Subcarangiform**	**0.0240**	**0.0815**	**0.2864**	**0.8578**
Largemouth bass Swim at 1.6 BL/s	Carangiform	0.0185	0.072	0.35	0.8
Largemouth bass Swim at 0.7 BL/s	Carangiform	0.0041	0.0472	0.3	0.59 ~ 0.83
Largemouth bass Swim at 1.2 BL/s	Carangiform	0.0053	0.0576	0.3	0.59 ~ 0.83
Largemouth bass Swim at 1.6 BL/s	Carangiform	0.0153	0.0651	0.3	0.59 ~ 0.83
Largemouth bass Swim at 2.0 BL/s	Carangiform	0.0165	0.0718	0.3	0.59 ~ 0.83
Largemouth Bass Swim at 2.4 BL/s	Carangiform	0.0181	0.0741	0.3	0.59 ~ 0.83
Saithe (Pollachius virens)	Carangiform	0.018	0.095	0.25	0.64 ~ 1.0
Mackerel (Scomber scombrus)	Carangiform	0.019	0.1075	0.35	0.63 ~ 0.83

Table 3.2: Travelling index of BCF fish analyzed from the biological data.The table is adapted for Cui et al. [5]

From Cui et al. [5], a empirical model for creating the fish locomotion, with defined scaling parameters

illustrated in figure 2.14. The empirical dimensionless model,

$$g(x,t) = G(x)\sin(2\pi f t - \frac{2\pi}{s_1}x) \tag{3.9}$$

with the dimentionless amplitude model,

$$G(x) = (s_2 + \frac{-2s_4(s_3 - s_2)}{1-2s_4}x + \frac{(s_3 - s_2)}{(1-2s_4)L}x^2)). \tag{3.10}$$

The empirical model, g(x,t) is now inserted with scaling parameters from the FFT. The g(x,t) plot with scaling parameters from the FFT for 10 midlines with 25 midlines pr. sec is shown in figure 3.48 and with 113 midlines and 25 midlines pr. sec i figure 3.49.

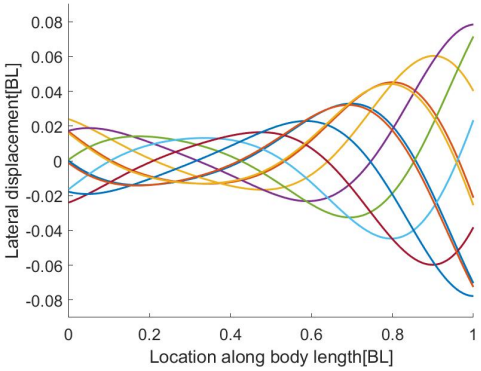

Figure 3.48: Fish motion with traveling index of the sea bass, 10 midlines

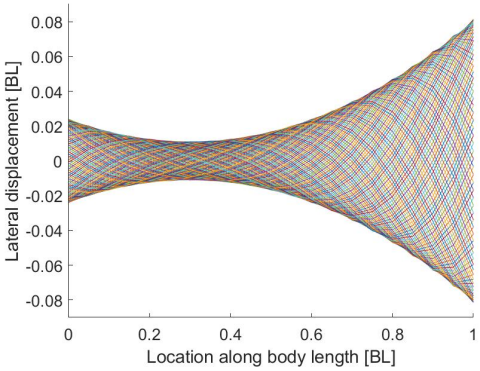

Figure 3.49: Fish motion with traveling index of the sea bass, 113 midlines

To further investigate if the FFT captures the entire fish motion, parts of the fish motion or the locomotion, the amplitude slope for the FFT function and for the empirical model with scaling parameters from the FFT is compared. Figure 3.50 indicates that the x_{min} for the empirical model of the FFT is close to zero, but the FFT function it is higher. The empirical model is only considers locomotion, which indicates that the FFT function consist of something more.

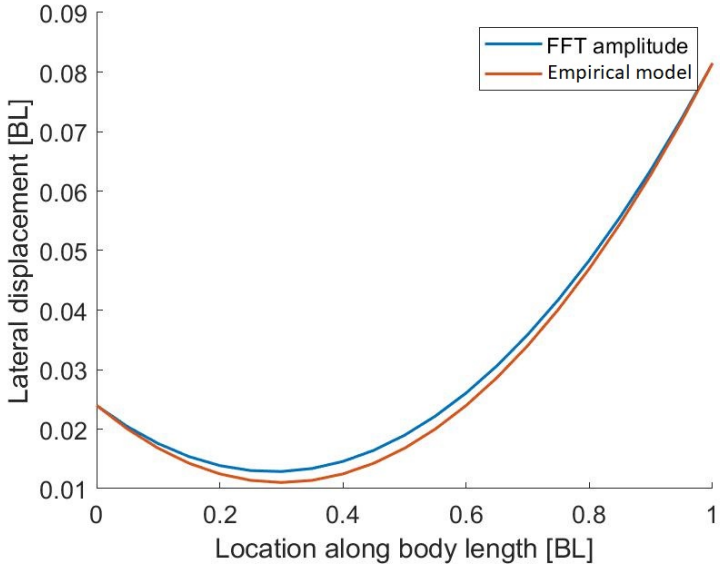

Figure 3.50: Difference in amplitude slope between the traveling index and the FFT

From the visual inspection, the FFT function with the reapplied detrend is plotted against the image frames, as shown in figures 3.51 and C.1. The fish is changing the mean horizontal position in time, to visually verify that the FFT is able to replicate the fish motion, the detrend is added to follow the trend of the fish.

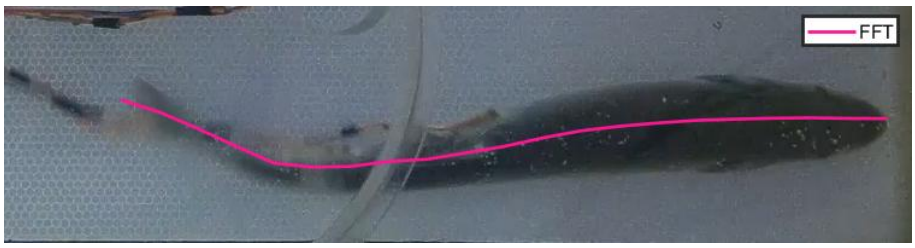

Figure 3.51: The FFT midline on the reference fish

3.3 Locomotion extraction

The fish function from the FFT is a strongly simplified function. From the filtering of every point in time, all motions connected with different frequencies are left out. This function is only considering the dominating frequency and does not truly capture the accurate fish motion. Ideally, the fish function should be dependent on more frequencies, and thus represent the true motion more accurately.

The approach that follows in this section allows the accrual midline to influence the results. The method is evaluating points directly from the initial midline in time. From the signal recorded in time, several points along the fish is evaluated to find the unknown parameters of a predefined law. Then, a linear system is achieved with the number of unknowns less than the number of the known quantities, which requires a Least Squares Method (LSM) and then a single value decomposition (SVD) technique to solve the linear system. The Least Squares Method is a least square fitting process. By using a SVD factorization it has the power to solve a large rectangular linear systems by finding the best fitted solution. The LSM used in this thesis is inspired by the method used by Fucile [7], for analysing and separating wave radar signals. The wave has a similar mathematical law as the fish motion and method should therefore work for separation of fish motion.

The technique will hereinafter be used for the inversion of the separation of fish motion into locomotion and recoil, with the target of evaluation directly from the initial midline in time. In order to verify the accuracy of this method, both a prescribed locomotion and recoil combination and a simplified FFT solution for the fish motion with similar characteristics, will be investigated.

The expressions used by Maertens [14], for describing locomotion and recoil motion, is used as the reference law for the best fitting. The subcarangiform expressions for locomotion used by Maertens [14] is,

$$Y_1(x_i, t_j) = (A_0 + A_1 x_i + A_2 x_i^2) \cdot \sin(\kappa x_i - \omega t_j + \epsilon_1^{'}). \tag{3.11}$$

and the subcarangiform expressions for recoil motion used by Maertens [14] is,

$$Y_2(x_i, t_j) = (B_0 + B_1 x_i) \cdot \sin(\omega t_j + \epsilon_2^{'}). \tag{3.12}$$

The motions, even being simplifications of the complex actual fish motion, still shows a nonlinear dependence. This would require a difficult nonlinear inversion process. To overcome this major challenge, the model is linearized with respect to the unknowns. Two different simplifications with corresponding assumptions are investigated, to solve this problem.

When using the LSM to solve a physical problem, the quality of the solution is directly cobbled with the reference law for the best fitting and the assumptions made for the unknowns in the reference law.

The better the reference law, the better the solution is going to be. When choosing points to evaluate in the LSM, they should not be chosen to close in either space or time. They should lead to independent equations.

The goal as aforementioned, is to obtain the best fitting solution to these models, based on the measurements, meaning that the measured values is set equal to the locomotion and recoil summed. The measured values is on the Right Hand Side (RHS) of the equation system and the combined locomotion and recoil is on the Left Hand Side (LHS).

$$\begin{aligned} A^* X^* &= b^* \\ \textbf{LHS} &= \textbf{RHS} \end{aligned} \tag{3.13}$$

A^* is the linearized combined locomotion and recoil matrix with respect to the X^* unknowns and b^* is measured midline points in time.

$$A^* X^* = \begin{bmatrix} (A_0 + A_1 x_1 + A_2 x_1^2) \cdot \sin(\kappa x_1 - \omega t_j + \epsilon_1^{'}) + (B_0 + B_1 x_1) \cdot \sin(\omega t_j + \epsilon_2^{'}) \\ (A_0 + A_1 x_2 + A_2 x_2^2) \cdot \sin(\kappa x_2 - \omega t_j + \epsilon_1^{'}) + (B_0 + B_1 x_2) \cdot \sin(\omega t_j + \epsilon_2^{'}) \\ \vdots \\ (A_0 + A_1 x_{n-1} + A_2 x_{n-1}^2) \cdot \sin(\kappa x_{n-1} - \omega t_j + \epsilon_1^{'}) + (B_0 + B_1 x_{n-1}) \cdot \sin(\omega t_j + \epsilon_2^{'}) \\ (A_0 + A_1 x_n + A_2 x_n^2) \cdot \sin(\kappa x_n - \omega t_j + \epsilon_1^{'}) + (B_0 + B_1 x_n) \cdot \sin(\omega t_j + \epsilon_2^{'}) \end{bmatrix} \tag{3.14}$$

$$X^* = \begin{bmatrix} A_0 & A_1 & A_2 & \omega & \kappa & \epsilon_1^{'} & B_0 & B_1 & \omega & \epsilon_2^{'} \end{bmatrix}^T \tag{3.15}$$

$$b^* = \begin{bmatrix} \eta(x_1, t_j) \\ \eta(x_2, t_j) \\ \vdots \\ \eta(x_{n-1}, t_j) \\ \eta(x_n, t_j) \end{bmatrix} \tag{3.16}$$

In order verify with the FFT solution, the reference law has to be changed. The function obtained with the FFT is defined with cosine. For the FFT solution to be used as one of the verification tools, the locomotion and recoil function have to be redefined with respect to cosine.

The redefined sum of locomotion and recoil function is then,

$$\begin{aligned} Y^{'}(x_i, t_j) &= (A_0 + A_1 x_i + A_2 x_i^2) \cdot \cos(\kappa x_i - \omega t_j + \epsilon_1) + (B_0 + B_1 x_i) \cdot \cos(\omega t_j + \epsilon_2) \\ &= \textbf{LHS}. \end{aligned} \tag{3.17}$$

$$\mathbf{X} = \begin{bmatrix} A_0 & A_1 & A_2 & \kappa & \omega & \epsilon_1 & B_0 & B_1 & \omega & \epsilon_2 \end{bmatrix}^T \tag{3.18}$$

To solve the equation system, the LHS must be linearized with respect the unknowns **X**. The number of unknowns depends on the assumptions made, meaning that the **A** is linearized with respect to the assumed unknowns **X**. When the system is linearized, the LSM can be applied.

3.3.1 Oversimplified LSM

Assuming that there is only one frequency connected to the fish motion and that the domination frequency from FFT is this motion,then ω is 31.403 rad/s. Assuming further that the the wave number estimated for the FFT is the same for fish motion, then κ is 7.325 BL. The last assumption is that ϵ_1 and

ϵ_2 is zero, this is a bold assumption and an error is expected. These assumptions reduces the unknown **X** vector to,

$$\mathbf{X}' = \begin{bmatrix} A_0 & A_1 & A_2 & B_0 & B_1 \end{bmatrix}^T \tag{3.19}$$

which makes it much easier to linearize the LHS. The **LHS** is simplified from $Y^{'}(x_i, t_j)$ to $Y^{''}(x_i, t_j)$, based on the assumptions.

$$\begin{aligned} Y^{'}(x_i, t_j) &= (A_0 + A_1 x_i + A_2 x_i^2)\cos(\kappa x_i - \omega t_j + \epsilon_1) + (B_0 + B_1 x_i)\cos(\omega t_j + \epsilon_2) \\ Y^{''}(x_i, t_j) &= (A_0 + A_1 x_i + A_2 x_i^2)\cos(\kappa x_i - \omega t_j) + (B_0 + B_1 x_i)\cos(\omega t_j) \\ Y^{''}(x_i, t_j) &= (A_0 + A_1 x_i + A_2 x_i^2) \cdot C_h(x_i, t_j) + (B_0 + B_1 x_i) \cdot S_h(t_j) \end{aligned} \tag{3.20}$$

The linearized **A** matrix is,

$$\underbrace{\begin{bmatrix} C_h(x_1,t_j) & x_1 \cdot C_h(x_1,t_j) & x_1^2 \cdot C_h(x_1,t_j) & S_h(t_j) & x_1 \cdot S_h(t_j) \\ C_h(x_2,t_j) & x_2 \cdot C_h(x_2,t_j) & x_2^2 \cdot C_h(x_2,t_j) & S_h(t_j) & x_2 \cdot S_h(t_j) \\ \vdots & \vdots & \vdots & \vdots & \vdots \\ C_h(x_{n-1},t_j) & x_{n-1} \cdot C_h(x_{n-1},t_j) & x_{n-1}^2 \cdot C_h(x_{n-1},t_j) & S_h(t_j) & x_{n-1} \cdot S_h(t_j) \\ C_h(x_n,t_j) & x_n \cdot C_h(x_n,t_j) & x_n^2 \cdot C_h(x_n,t_j) & S_h(t_j) & x_n \cdot S_h(t_j) \end{bmatrix}}_{\mathbf{A}'} \tag{3.21}$$

3.3.2 Simplified LSM

Assuming that there is only one frequency connected to the fish motion and that the domination frequency from FFT is this motion,then ω is 31.403 rad/s. Assuming further that the the wave number estimated for the FFT is the same for fish motion, then κ is 7.325 BL. This assumption is only considering a dominating frequency, which could possible remove some contributions to the motion. These assumptions reduce the unknown **X** vector to,

$$\mathbf{X''} = \begin{bmatrix} A_0 & A_1 & A_2 & \epsilon_1 & B_0 & B_1 & \epsilon_2 \end{bmatrix}^T \tag{3.22}$$

The **LHS** is simplified from $Y^{'}(x_i, t)$ to $Y^{''}(x_i, t)$, based on the assumptions.

$$\begin{aligned} Y^{'}(x_i, t) =& (A_0 + A_1 x_i + A_2 x_i^2)\cos(\kappa x_i - \omega t + \epsilon_1) + (B_0 + B_1 x_i)\cos(\omega t + \epsilon_2) \\ =& (A_0 + A_1 x_i + A_2 x_i^2) \cdot (\cos(\kappa x_i - \omega t_j) \cdot \cos(\epsilon_1) + \sin(\kappa x_i - \omega t_j) \cdot \sin(\epsilon_1)) \\ &+ (B_0 + B_1 x_i) \cdot (\cos(\omega t_j) \cdot \cos(\epsilon_2) + \sin(\omega t_j) \cdot \sin(\epsilon_2)) \end{aligned} \tag{3.23}$$

To linearize the A matrix, it is now assumed that omega and the wave number is known from FFT and that ϵ is nonzero. Based on these assumptions, the cosine functions for locomotion and recoil has to be separated in order to be linearized. Each ϵ has to be included with the amplitude coefficients in order to get a linear system. The results must be separated into ϵ and amplitude coefficients respectfully

afterwards.

$$\mathbf{A}'^{\mathbf{T}} = \begin{bmatrix} \sin(\kappa x_1 - \omega t_1) & \sin(\kappa x_2 - \omega t_1) & \dots & \sin(\kappa x_{n-1} - \omega t_1) & \sin(\kappa x_n - \omega t_1) \\ x_1 \sin(\kappa x_1 - \omega t_1) & x_2 \sin(\kappa x_2 - \omega t_1) & \dots & x_{n-1} \sin(\kappa x_{n-1} - \omega t_1) & x_n \sin(\kappa x_n - \omega t_1) \\ x_1^2 \sin(\kappa x_1 - \omega t_1) & x_2^2 \sin(\kappa x_2 - \omega t_1) & \dots & x_{n-1}^2 \sin(\kappa x_{n-1} - \omega t_1) & x_n^2 \sin(\kappa x_n - \omega t_1) \\ \cos(\kappa x_1 - \omega t_1) & \cos(\kappa x_2 - \omega t_1) & \dots & \cos(\kappa x_{n-1} - \omega t_1) & \cos(\kappa x_n - \omega t_1) \\ x_1 \cos(\kappa x_1 - \omega t_1) & x_2 \cos(\kappa x_2 - \omega t_1) & \dots & x_{n-1} \cos(\kappa x_{n-1} - \omega t_1) & x_n \cos(\kappa x_n - \omega t_1) \\ x_1^2 \cos(\kappa x_1 - \omega t_1) & x_2^2 \cos(\kappa x_2 - \omega t_1) & \dots & x_{n-1}^2 \cos(\kappa x_{n-1} - \omega t_1) & x_n^2 \cos(\kappa x_n - \omega t_1) \\ \sin(\omega t_1) & \sin(\omega t_1) & \dots & \sin(\omega t_1) & \sin(\omega t_1) \\ x_1 \sin(\omega t_1) & x_2 \sin(\omega t_1) & \dots & x_{n-1} \sin(\omega t_1) & x_n \sin(\omega t_1) \\ \cos(\omega t_1) & \cos(\omega t_1) & \dots & \cos(\omega t_1) & \cos(\omega t_1) \\ x_1 \cos(\omega t_1) & x_2 \cos(\omega t_1) & \dots & x_{n-1} \cos(\omega t_1) & x_n \cos(\omega t_1) \end{bmatrix} \tag{3.24}$$

$$\mathbf{X}''' = \begin{bmatrix} A_0 \cos(\epsilon 1) \\ A_1 \cos(\epsilon 1) \\ A_2 \cos(\epsilon 1) \\ A_0 \sin(\epsilon 1) \\ A_1 \sin(\epsilon 1) \\ A_2 \sin(\epsilon 1) \\ B_0 \cos(\epsilon 2) \\ B_1 \cos(\epsilon 2) \\ B_0 \sin(\epsilon 2) \\ B_1 \sin(\epsilon 2) \end{bmatrix} \tag{3.25}$$

$$\mathbf{X}''' = \begin{bmatrix} A_{00} & A_{10} & A_{20} & A_{01} & A_{11} & A_{21} & B_{00} & B_{10} & B_{01} & B_{11} \end{bmatrix}^T \tag{3.26}$$

$$\mathbf{b} = \begin{bmatrix} Y(x_1, t) = Amp(x_1)\cos(\omega t + Pm(x_1)) \\ Y(x_2, t) = Amp(x_2)\cos(\omega t + Pm(x_2)) \\ \vdots \\ Y(x_{n-1}, t) = Amp(x_{n-1})\cos(\omega t + Pm(x_{n-1})) \\ Y(x_n, t) = Amp(x_n)\cos(\omega t + Pm(x_n)) \end{bmatrix} \tag{3.27}$$

A'X''' = b

The equation system is solved by separating X''' in to 4 linear equation indicated with notation from 1 to 4 in equation 3.28. Then having solved each system, the solution for X'' is found.

$$\mathbf{A'X'''} = \begin{bmatrix} A_1 X_1 \\ A_2 X_2 \\ A_3 X_3 \\ A_4 X_4 \end{bmatrix} = \begin{bmatrix} b_1 \\ b_2 \\ b_3 \\ b_4 \end{bmatrix} \tag{3.28}$$

3.3.3 Verification of LSM

To verify the oversimplified and the simplified LSM, a set of cases is examined. In this section, different cases for verification are introduced, before each method is examined with these cases individually in the next sections.

Cases to be examine:

1. Prescribed locomotion and recoil
2. Prescribed locomotion and recoil + noise

3. Prescribed FFT function

4. Prescribed FFT function + noise

5. LSM directly

To verify if either models are suitable for identifying the locomotion and the recoil directly from the initial midline, the models have to be thoroughly investigated, to know how sensitive they are and which restriction they have. The first and second case are performed by assigning a summation of locomotion and recoil to the RHS, on the same form as the simplified $Y'(x_i, t_j)$ equation of Maertens [14].

The prescribed motion is,

$$Y(x_i,t_j)''' = (0.0240-0.0775x_i+0.1351x_i^2)\cos(7.3250x_i-2\pi 4.9558t_j)+(0.0030-0.0120x)\cos(2\pi 4.9558t_j). \tag{3.29}$$

This is done to simply see if the method is able to solve the problem if given an ideal motion, with respect to the reference law. To further verify if the method is able to find back to the prescribed motion and how sensitive it is, a high frequency noise is added on top of the prescribed motion,

$$Y(x_i,t_j)'''_{noise} = (0.0240-0.0775x_i+0.1351x_i^2)\cos(7.325x_i-2\pi 4.9558t_j)+(0.0030-0.0120x)\cos(2\pi 4.9558t_j)+\textbf{NOISE}. \tag{3.30}$$

For the third case, the fish function obtained thought the FFT is replacing the measurements and set equal to the locomotion and the recoil. The FFT function is the RHS, **b**, of the equation and the combined locomotion and recoil solution is the LHS, **AX**. **b** as the FFT function is assign as the RHS, to verify that the method is able to separate the FFT function into a locomotion and recoil motion.

$$\mathbf{AX} = \mathbf{b} \tag{3.31}$$

The FFT solution of the sea bass is,

$$\begin{aligned} Y(x_i,t_j) &= Amp(x_i)\cdot\cos(2\pi f\cdot t_j + Pm(x_i)) \\ &= \textbf{RHS}. \end{aligned} \tag{3.32}$$

If the method is able to reconstruct the FFT function as a combination of locomotion and recoil, additional high frequency noise is added on to the FFT function, to verify how sensitive it is.

$$\begin{aligned} Y(x_i,t_j) &= Amp(x_i)\cos(\omega t_j + Pm(x_i)) + \textbf{noise} \\ Y(x_i,t_j) &= (0.0242 - 0.0770x_i + 0.1365\cdot x_i^2)\cdot\cos(2\pi 4.9558t_j + (5.074 - 3.911x_i - 7.651x_i^2 + 5.132x_i^3)) + \textbf{noise} \end{aligned} \tag{3.33}$$

Lastly, the application of the LSM directly to the experiments, will be done. The RHS is then,

$$b^* = \begin{bmatrix} \eta(x_1,t_j) \\ \eta(x_2,t_j) \\ \vdots \\ \eta(x_{n-1},t_j) \\ \eta(x_n,t_j). \end{bmatrix} \tag{3.34}$$

3.3.4 Verification of the oversimplified LSM

In this section the oversimplified LSM is examined with the aforementioned cases. For the oversimplified LSM, it is assumed that ω is 31.403 rad/s, κ is 7.325 BL^{-1} and that ϵ_1 and ϵ_2 are zero.

1. Prescribed locomotion and recoil

To verify that the procedure is properly set up, a prescribed locomotion and recoil on the form used by Maertens [14] is initially assign to the RHS. To ensure that the prescribed motion given to the fish is realistically, the FFT amplitude is prescribed as the locomotion amplitude.

The prescribed motion is,

$$Y(x_i,t_j)''' = (0.0240-0.0775x_i+0.1351x_i^2)\cos(7.3250x_i-2\pi 4.9558t_j)+(0.0030-0.0120x)\cos(2\pi 4.9558t_j), \tag{3.35}$$

$$\begin{aligned} \text{Input RHS}: \mathbf{X}' &= \begin{bmatrix} 0.0240 & -0.0775 & 0.1351 & 0.0030 & -0.0120 \end{bmatrix}^T \\ \text{Output LHS}: \mathbf{X}' &= \begin{bmatrix} 0.0240 & -0.0775 & 0.1351 & 0.0030 & -0.0120 \end{bmatrix}^T \end{aligned} \tag{3.36}$$

and **b'** is the RHS vector of $Y(x_i,t_j)'''$, which completes **A'X'** = **b'**. The prescribed **b'** vector is shown in 3.52 as the examined value for each point on the **b'** vector and 3.53 as the midline for 10 examined time frames.

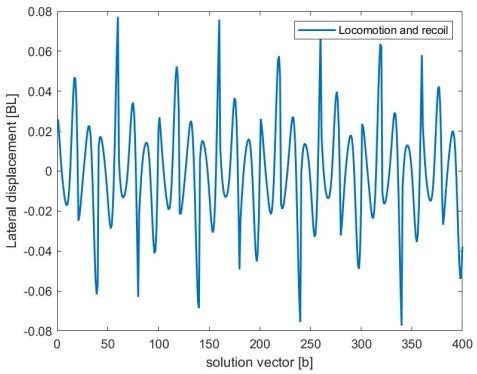

Figure 3.52: The **b'** vector plotted against the lateral displacement

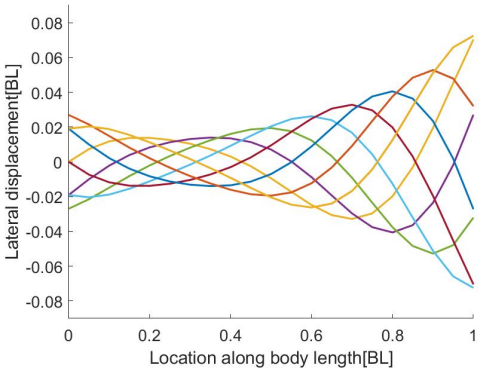

Figure 3.53: The RHS, $Y(x_i,t_j)'''$

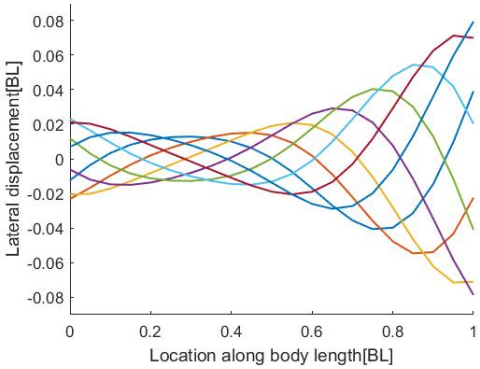

Figure 3.54: The separated locomotion

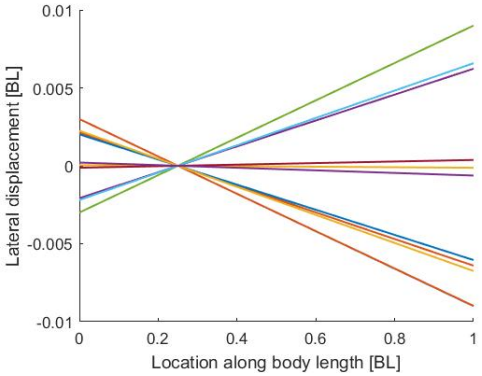

Figure 3.55: The separated recoil

The method is able to separate the ideal function, and the frame work for the set up is properly done. The plot of the separated recoil 3.53 indicates that the recoil has a center between 0.2 BL and 0.3 BL.

Given the form on the locomotion and the combined function, one can conclude that the amplitude slope for the motion does not change sign.

2. Prescribed locomotion and recoil with noise

To verify how sensitive the procedure is, additional high frequency noise is added on the signal.

$$Y(x_i,t_j)'''_{noise} = (0.0240-0.0775x_i+0.1351x_i^2)\cos(7.325x_i-2\pi 4.9558t_j)+(0.0030-0.0120x)\cos(2\pi 4.9558t_j)+\textbf{NOISE} \tag{3.37}$$

$$\begin{aligned} \text{Input RHS}: \mathbf{X}' &= \begin{bmatrix} 0.0240 & -0.0775 & 0.1351 & 0.0030 & -0.0120 \end{bmatrix}^T \\ \text{Output LSH}: \mathbf{X}' &= \begin{bmatrix} 0.0231 & -0.0822 & 0.1410 & 0.0037 & -0.0137 \end{bmatrix}^T \end{aligned} \tag{3.38}$$

b'_{noise} is the RHS vector of $Y(x_i,t_j)'''_{noise}$, which completes **A'X'** = b'_{noise}. The procedure **b'** vector plus the added noise is shown in figure 3.56 as the examined value plus noise for each point on the **b'** vector and in figure 3.58 as the midline for 10 examined time frames.

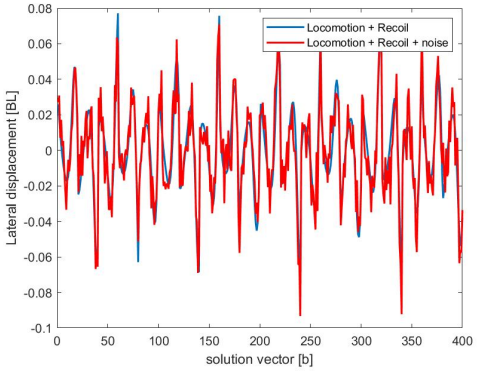

Figure 3.56: The **b'** and the b'_{noise} vector plotted against the lateral displacement

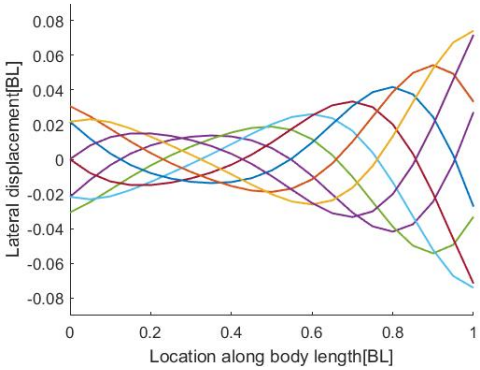

Figure 3.57: The RHS, $Y(x_i,t_j)'''_{noise}$

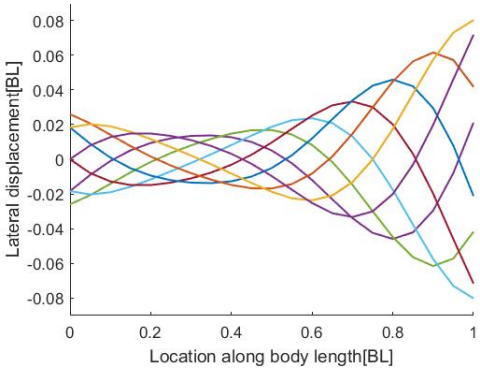

Figure 3.58: The separated locomotion

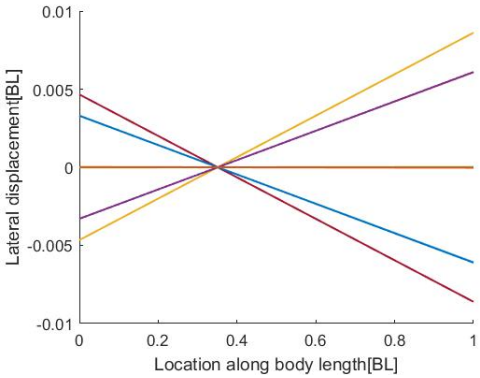

Figure 3.59: The separated recoil

These results indicate that the procedure is affected by high frequency noise. The form of the locomotion is recovered, but the center of recoil is shifted to approximately 0.4 BL and it is smaller. The procedure is able to filter most of noise out.

3. Prescribed FFT function

Thirdly, FFT function is assigned the RHS, without noise, which completes **A'X'** = **b**

.

$$
\begin{aligned}
&Y(x_i,t_j) = Amp(x_i)\cos(\omega t_j + Pm(x_i)) \\
&Y(x_i,t_j) = (0.0242 - 0.0770x_i + 0.1365x_i^2)\cdot\cos(2\pi 4.9558 t_j + (5.074 - 3.911x_i - 7.651x_i^2 + 5.132x_i^3))
\end{aligned}
\tag{3.39}
$$

$$
\begin{aligned}
\text{Input RHS}: \mathbf{X'} &= \begin{bmatrix} 0.0242 & -0.0770 & 0.1365 & [-] & [-] \end{bmatrix}^T \\
\text{Output LHS}: \mathbf{X'} &= \begin{bmatrix} 0.0213 & -0.0734 & 0.1075 & -0.0104 & 0.0232 \end{bmatrix}^T
\end{aligned}
\tag{3.40}
$$

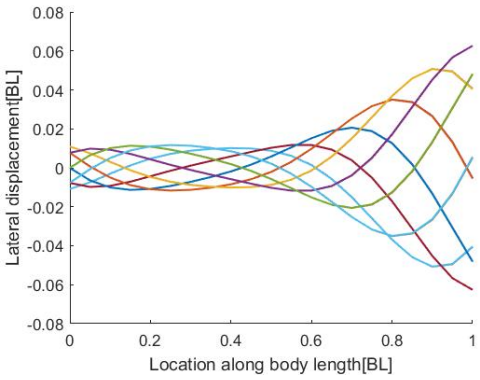

Figure 3.60: The combined locomotion and recoil from FFT

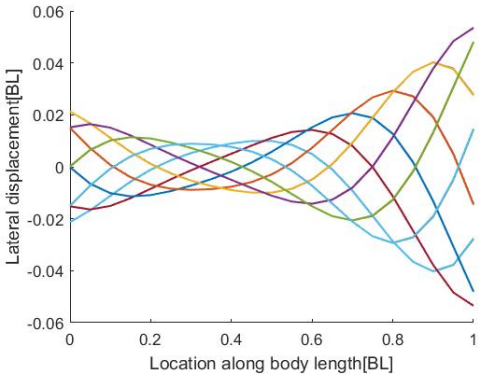

Figure 3.61: The separated locomotion from FFT

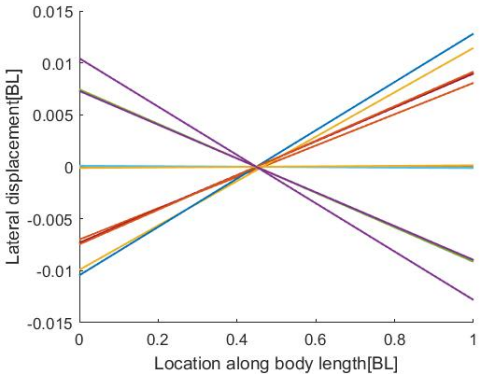

Figure 3.62: The separated recoil motion from FFT

Figure 3.60 indicates that the separated locomotion and recoil function combined in figure 3.60 deviate from the original FFT plot in figure 3.48. The separated locomotion on the other hand is very similar to the FFT plot, as shown in figure 3.61. The sperated recoil is located between 0.4 BL an 0.5 BL.

4. Prescribed FFT function plus noise

The FFT function is subscribed additional noise, to investigate how sensitive the solution is.

$$Y(x_i,t_j) = Amp(x_i)\cos(\omega t_j + Pm(x_i)) + \textbf{noise}$$
$$Y(x_i,t_j) = (0.0242 - 0.0770x_i + 0.1365\cdot x_i^2)\cdot\cos(2\pi 4.9558 t_j + (5.074 - 3.911x_i - 7.651x_i^2 + 5.132x_i^3)) + \textbf{noise} \tag{3.41}$$

$$\begin{aligned} \text{Input}: \mathbf{X} &= \begin{bmatrix} 0.0242 & -0.0770 & 0.1365 & [-] & [-] \end{bmatrix}^T \\ \text{Output without noise}: \mathbf{X} &= \begin{bmatrix} 0.0213 & -0.0734 & 0.1075 & -0.0104 & 0.0232 \end{bmatrix}^T \\ \text{Output}: \mathbf{X} &= \begin{bmatrix} 0.0203 & -0.0670 & 0.1035 & -0.0092 & 0.0210 \end{bmatrix}^T \end{aligned} \tag{3.42}$$

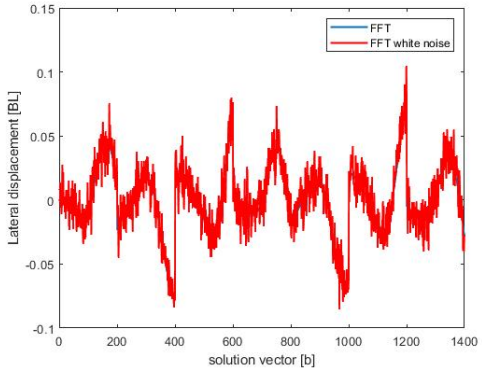

Figure 3.63: The **b'** and the b'_{noise} vector plotted against the lateral displacement

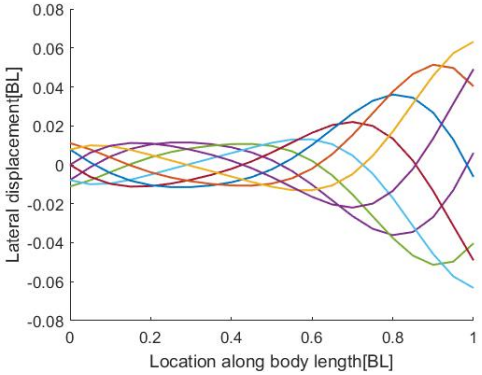

Figure 3.64: The combined locomotion and recoil from FFT plus noise

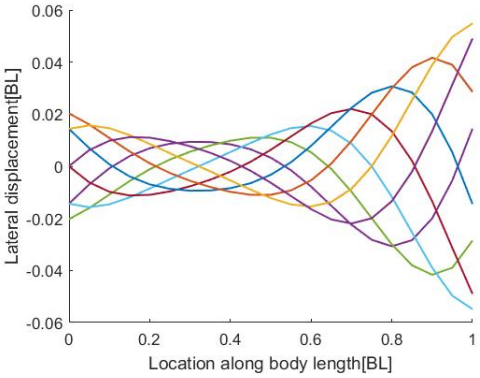

Figure 3.65: The separated locomotion from FFT plus noise

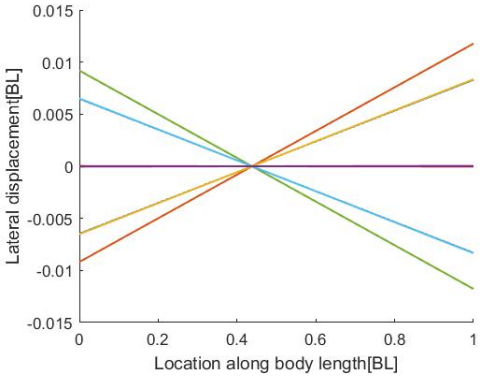

Figure 3.66: The separated recoil motion from FFT plus noise

The results indicate that the oversimplified LSM, with either the prescribed ideal motion or the FFT, is equally sensitive to additional noise, but is able to separate out the function.

5. LSM direct measured evolution of the midline point

The direct measured evolution of the midline points is prescribed to the RHS,

$$\eta(x_i,t_j). \tag{3.43}$$

$$\begin{aligned} &\text{Input RHS}: \textbf{The initial midline} \\ &\text{Output LHS}: \mathbf{X} = \begin{bmatrix} 0.0227 & -0.0678 & 0.0917 & -0.0074 & 0.0320 \end{bmatrix}^T \end{aligned} \tag{3.44}$$

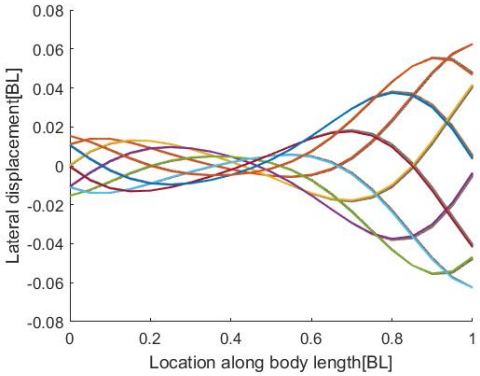

Figure 3.67: The combined locomotion and recoil from the initial midline

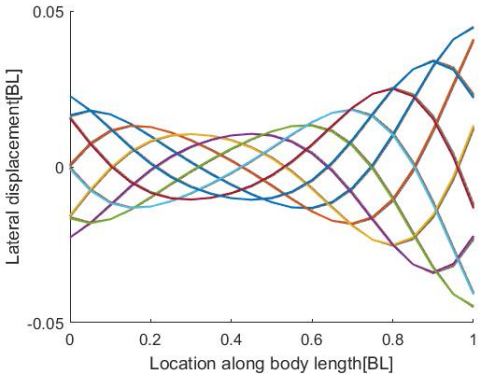

Figure 3.68: The separated locomotion from the initial midline

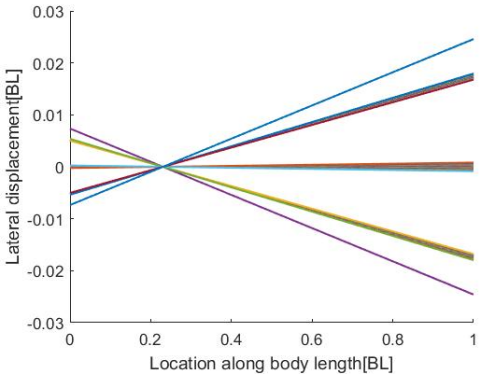

Figure 3.69: The separated recoil motion from the initial midline

The locomotion plot in figure 3.68 has a form very similar to the simplified FFT plot 3.45, but with lower values. The recoil center in figure 3.69 is between 0.2 BL and 0.3 BL, similar to the recoil for the prescribed motion.

3.3.5 Verification of simplified LSM

In this section, the simplified method is examined with the aforementioned cases.The assumption made in the simplified method is that ω is 31.403 rad/s, κ is 7.325 BL^{-1}.

When solving the equation systems one has to adjust for jumps caused by a non-physical phase shift. The phase shift comes as a result of dividing sine and cosine. The tang function is only able to get to two of the four quadrants on the unit circle for sine and cosine. One must therefore make sure that the physical solution is found. This is done by visual inspection of the results and verifying that the recoil has a center on the midline and that the locomotion amplitude slope does not change sign. The LSM is a method where a good academical guess gives good results, and for the results one can iterate towards an improved guess, to get even better results. When knowing that one is in the physical domain, ϵ_1 and ϵ_2 give the location where the difference between functions on each side of the equation system shown in equation 3.45 are the lowest. The red equation system is with ϵ_1 and the green with ϵ_2. In figure 3.70 and figure 3.71, ϵ_1 and ϵ_2 are respectively plotted for values between 0 to 2π on the horizontal axis with

the corresponding difference between the LHS and the RHS on the vertical axis. The red line indicates the lowest error for the physical value for ϵ_1 and ϵ_2 respectively.

$$\begin{bmatrix} A_1X_1 \\ A_2X_2 \end{bmatrix} = \begin{bmatrix} b_1 \\ b_2 \end{bmatrix} \qquad \begin{bmatrix} A_3X_3 \\ A_4X_4 \end{bmatrix} = \begin{bmatrix} b_3 \\ b_4 \end{bmatrix} \tag{3.45}$$

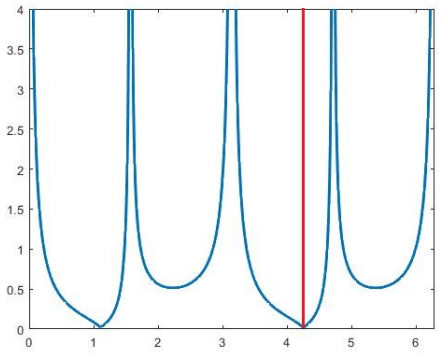

Figure 3.70: ϵ_1 on the horizontal axis with the corresponding difference between the LHS and the RHS on the vertical axis

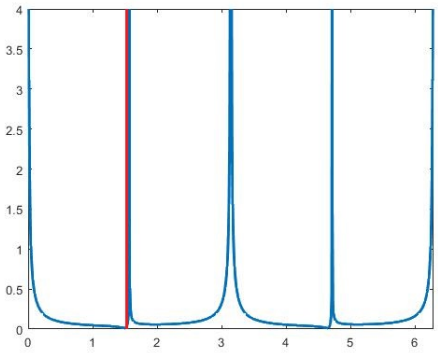

Figure 3.71: ϵ_2 on the horizontal axis with the corresponding difference between the LHS and the RHS on the vertical axis

When this is ensured, the same verification procedure as done for the oversimplified LSM is preformed.

1. Prescribed locomotion and recoil

To verify that the simplified procedure is properly set up, a prescribed locomotion and recoil on the form used by Maertens [14] is initially assigned to the RHS.

The prescribed motion is,

$$Y(x_i,t_j)''' = (0.0240-0.0775x_i+0.1351x_i^2)\cos(7.325x_i-2\pi 4.9558t_j)+(0.0030-0.0120x)\cos(2\pi 4.9558t_j), \tag{3.46}$$

$$\begin{aligned} \text{Input}: \mathbf{X}' &= \begin{bmatrix} 0.0240 & -0.0775 & 0.1351 & 0.0030 & -0.0120 \end{bmatrix}^T \\ \text{Output}: \mathbf{X}' &= \begin{bmatrix} 0.0240 & -0.0775 & 0.1351 & 0.0030 & -0.0120 \end{bmatrix}^T \\ \text{Output}: \mathbf{X}'' &= \begin{bmatrix} 0.0240 & -0.0775 & 0.1351 & -3.9271 & 0.0030 & -0.0120 & -4.5 \end{bmatrix}^T \end{aligned} \tag{3.47}$$

The **b'** is the RHS vector of $Y(x_i,t_j)'''$, which completes **A'X'** = **b'**. A selection of the prescribed **b'** vector is shown in figure 3.72 as the examined value for each point on the **b'** vector and in figure 3.53 as the midline for 10 examined time frames.

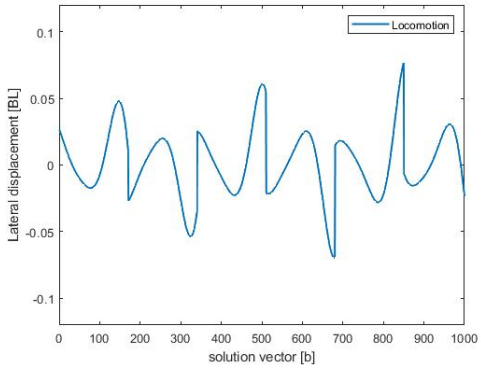

Figure 3.72: A part of the **b'** vector plotted against the lateral displacement

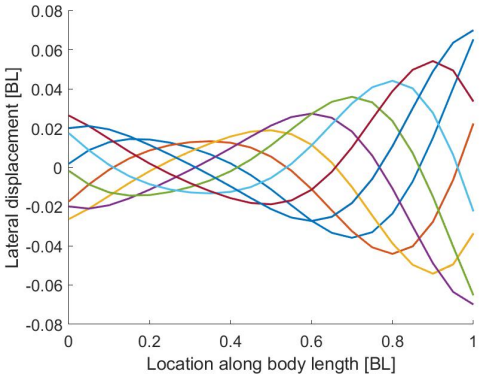

Figure 3.73: The RHS, $Y(x_i,t_j)'''$

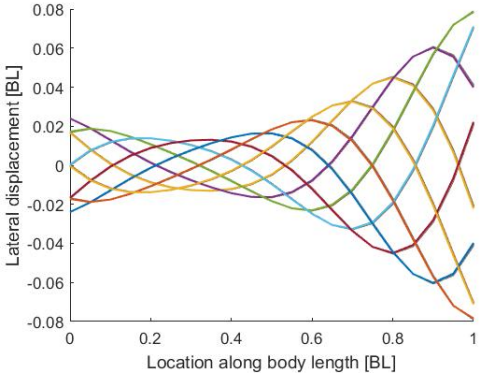

Figure 3.74: The spectated locomotion

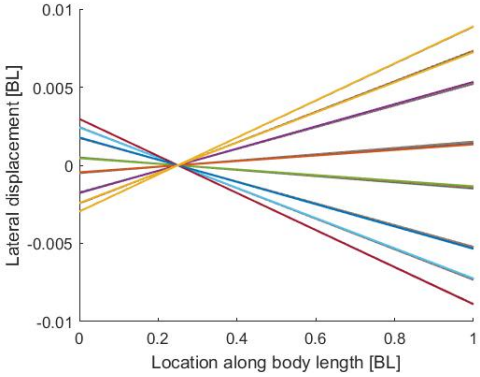

Figure 3.75: The spectated recoil

2. Prescribed locomotion, recoil and noise

To verify how sensitive the procedure is to additional noise on the signal, high frequency noise is added.

$$Y(x_i,t_j)'''_{noise} = (0.02397-0.07754x_i+0.1351x_i^2)\cos(7.325x_i-2\pi 4.9558t_j)+(0.0030-0.0120x)\cos(2\pi 4.9558t_j)+\textbf{NOISE} \tag{3.48}$$

$$\begin{aligned}
\text{Input}: \mathbf{X}' &= \begin{bmatrix} 0.0240 & -0.0775 & 0.1351 & 0.0030 & -0.0120 \end{bmatrix}^T \\
\text{Output}: \mathbf{X}' &= \begin{bmatrix} 0.0172 & -0.0386 & 0.1006 & 0.0087 & -0.0192 \end{bmatrix}^T \\
\text{Output}: \mathbf{X}'' &= \begin{bmatrix} 0.0172 & -0.0386 & 0.1006 & -6.3416 & 0.0087 & -0.0192 & -3.0000 \end{bmatrix}^T
\end{aligned} \tag{3.49}$$

b'_{noise} is the RHS vector of $Y(x_i,t_j)'''_{noise}$, which completes **A'X'** = b'_{noise}. The procedure **b'** vector plus the added noise is shown in figure 3.76 and 3.77.

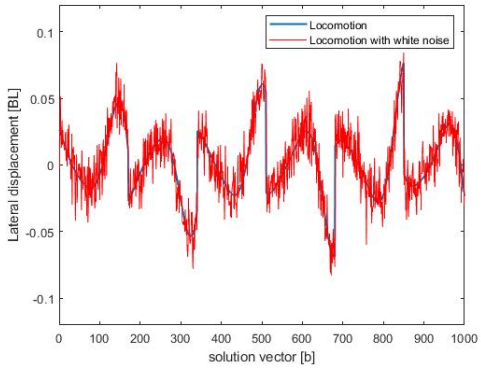

Figure 3.76: A part of the **b'** and the b'_{noise} vector plotted against the lateral displacement

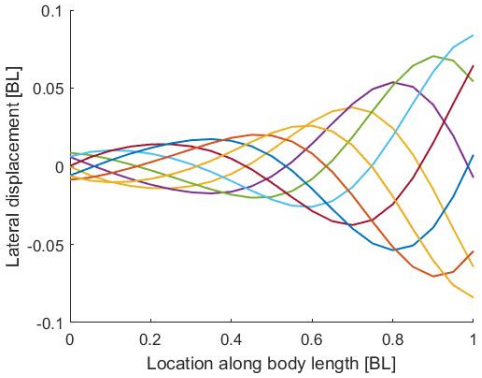

Figure 3.77: The RHS, $Y(x_i,t_j)'''_{noise}$

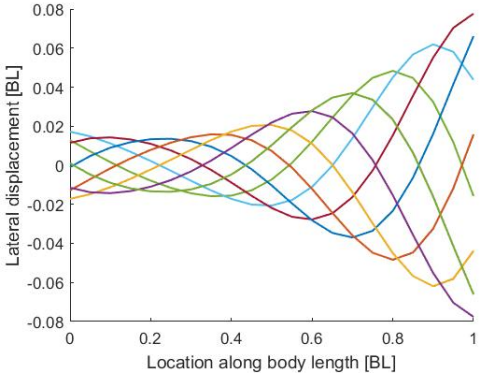

Figure 3.78: The separated locomotion

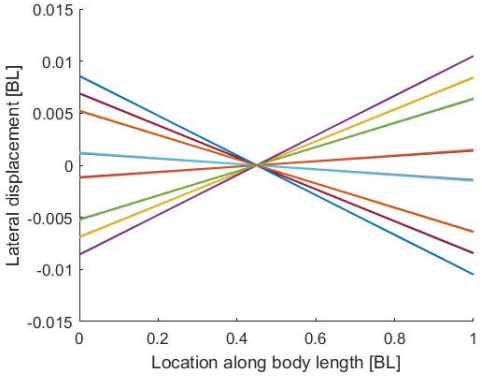

Figure 3.79: The separated recoil

These results indicate that the procedure is affected by high frequency noise, but when the input is on the same form as the output, the procedure is able to filter the noise out.

3. Prescribed FFT function

The prescribed FFT function is,

$$\begin{aligned} Y(x_i,t_j) &= \mathrm{Amp}(x_i)\cos(\omega t_j + Pm(x_i)) \\ Y(x_i,t_j) &= (0.0242 - 0.0770x_i + 0.1365x_i^2)\cdot\cos(2\pi 4.9558 t_j + (5.074 - 3.911x_i - 7.651x_i^2 + 5.132x_i^3)) \end{aligned} \tag{3.50}$$

$$\begin{aligned} \text{Input}: \mathbf{X} &= \begin{bmatrix} 0.0242 & -0.0770 & 0.1365 & [-] & [-] \end{bmatrix}^T \\ \text{Output}: \mathbf{X} &= \begin{bmatrix} -0.0296 & 0.0996 & 0.0367 & -0.0231 & 0.0424 \end{bmatrix}^T \end{aligned} \tag{3.51}$$

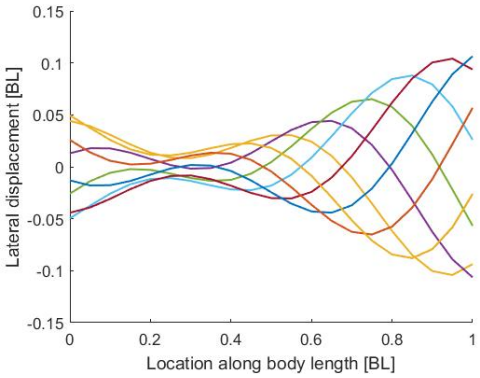

Figure 3.80: The combined locomotion and recoil from the FFT

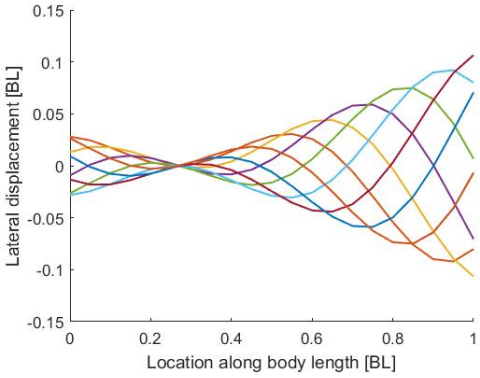

Figure 3.81: The separated locomotion from the FFT

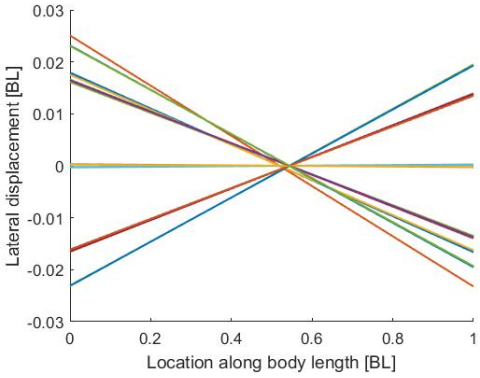

Figure 3.82: The separated recoil motion from the FFT

From the plots in figure 3.81, one can see that the locomotion is changing signs between 0.2 BL and 0.3 BL. This problem is in connection with the phase shift. This is similar to the same problem for the original FFT combination of wave number combined with the phase shift.

5. LSM direct measured evolution of the midline point

The direct measured evolution of the midline points is prescribed to the RHS, with

$$\eta\left(x_i, t_j\right). \tag{3.52}$$

$$\begin{aligned} &\text{Input}: \textbf{The initial midline} \\ &\text{Output oversimplified LSM}: \mathbf{X} = \begin{bmatrix} 0.0227 & -0.0678 & 0.0917 & -0.0074 & 0.0320 \end{bmatrix}^T \\ &\text{Output simplified LSM}: \mathbf{X} = \begin{bmatrix} 0.0285 & -0.1052 & 0.1480 & -0.0085 & 0.0368 \end{bmatrix}^T \end{aligned} \tag{3.53}$$

$$\begin{aligned} \epsilon 1 &= -4.2500 \\ \epsilon 2 &= -1.5575 \end{aligned} \tag{3.54}$$

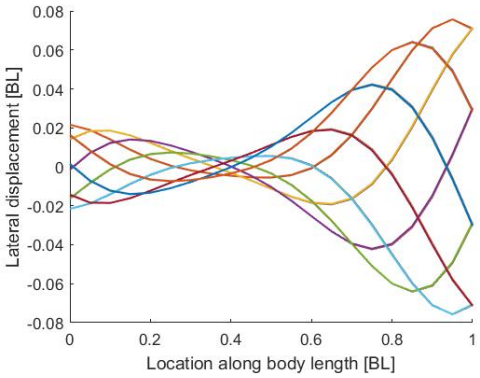

Figure 3.83: The combined locomotion and recoil from the initial midline

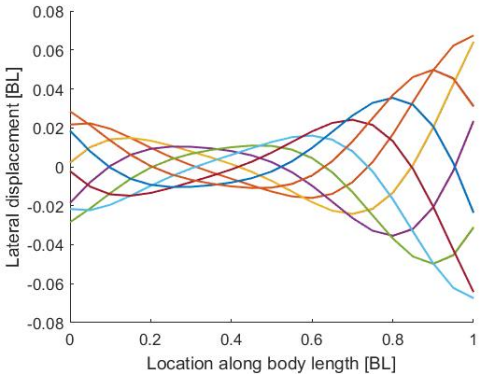

Figure 3.84: The separated locomotion from the initial midline

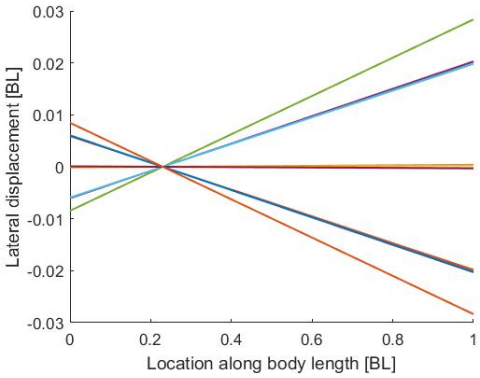

Figure 3.85: The separated recoil motion from the initial midline

From the plot in figure 3.83, one can observe that slope of the amplitude outline is similar to the oversimplified LSM. The locomotion and recoil are equally similar to the oversimplified LSM.

3.3.6 Comparison

The locomotion and recoil results from the different methods, with the different cases in equation 3.54. One can see that the outline of all the slopes is similar, except the simplified LSM with the FFT case. This indicates that the simplified LSM with the direct case is able to separate the locomotion out properly.

$$\begin{aligned}
\text{Oversimplified LSM FFT}: \mathbf{X} &= \begin{bmatrix} 0.0213 & -0.0734 & 0.1075 & -0.0104 & 0.0232 \end{bmatrix}^T \\
\text{Simplified FFT}: \mathbf{X} &= \begin{bmatrix} -0.0296 & 0.0996 & 0.0367 & -0.0231 & 0.0424 \end{bmatrix}^T \\
\text{Oversimplified LSM direct}: \mathbf{X} &= \begin{bmatrix} 0.0227 & -0.0678 & 0.0917 & -0.0074 & 0.0320 \end{bmatrix}^T \\
\text{Simplified direct}: \mathbf{X} &= \begin{bmatrix} 0.0285 & -0.1052 & 0.1480 & -0.0085 & 0.0368 \end{bmatrix}^T
\end{aligned} \tag{3.55}$$

From visually inspection the plots in figures 3.3.6, the oversimplified LSM with FFT case has a similar form to the simplified FFT solution in figure 3.50, but the amplitude in the tail region is smaller then the simplified FFT solution. The oversimplified LSM with the direct case in figure 3.88 has the same problem, but with even larger difference in tail amplitude. The simplified LSM with FFT case in figure 3.87 indicates a change of sign for the outline of the amplitude, as result of a phase shift. The simplified LSM with the direct case in figure 3.89, has a similar form to the simplified FFT solution in figure 3.50, with a similar amplitude in the tail region, but a larger amplitude in head region. The lowest point on the amplitude slope is located further back for the simplified FFT solution.

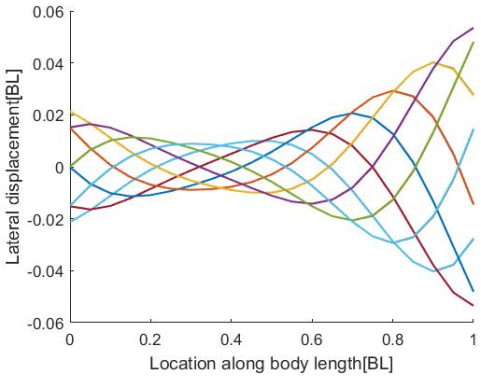

Figure 3.86: The separated locomotion from FFT

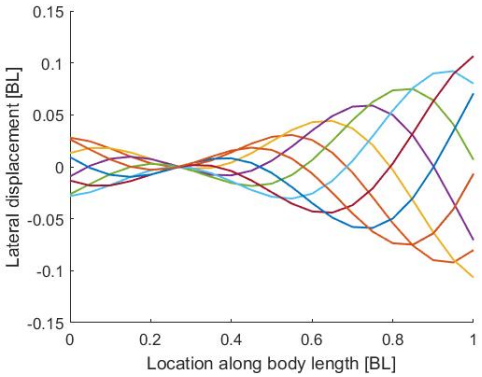

Figure 3.87: The separated locomotion from the FFT

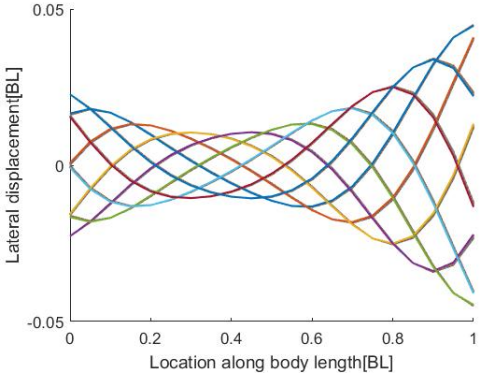

Figure 3.88: The separated locomotion from the initial midline

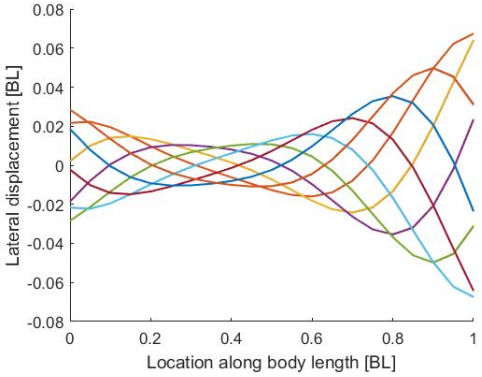

Figure 3.89: The separated locomotion from the initial midline

A selection of the travelling index of BCF fish analyzed from the biological data, is brought together by Cui et al. [5] is in table 3.3. The different scaling parameters of the midline motion of BCF fish are color coded with reference to the scaling parameters of simplified LSM with the direct case. The bold is the reference, the yellow indicates parameters close to the reverence and the green indicates the BCF fish that fits the simplified LSM with the direct case best.

Fish names	Fish categories	s_2(BL)	s_3(BL)	s_4(BL)	λ(BL)
LSM locomotion function	**Subcarangiform**	**0.0271**	**0.0712**	**0.37**	**0.8578**
Largemouth bass Swim at 1.6 BL/s	Carangiform	0.0185	0.072	0.35	0.8
Largemouth bass Swim at 0.7 BL/s	Carangiform	0.0041	0.0472	0.3	0.59 ~ 0.83
Largemouth bass Swim at 1.2 BL/s	Carangiform	0.0053	0.0576	0.3	0.59 ~ 0.83
Largemouth bass Swim at 1.6 BL/s	Carangiform	0.0153	0.0651	0.3	0.59 ~ 0.83
Largemouth bass Swim at 2.0 BL/s	Carangiform	0.0165	0.0718	0.3	0.59 ~ 0.83
Largemouth Bass Swim at 2.4 BL/s	Carangiform	0.0181	0.0741	0.3	0.59 ~ 0.83
Saithe (Pollachius virens)	Carangiform	0.018	0.095	0.25	0.64 ~ 1.0
Mackerel (Scomber scombrus)	Carangiform	0.019	0.1075	0.35	0.63 ~ 0.83

Table 3.3: Travelling index of BCF fish analyzed from the biological data. The table is adaped for Cui et al. [5]

From identifying the scaling parameters for the empirical model locomotion model and comparing them to the ones found from biological data, one can see that the sea bass is closest to the Largmouth

bass swimming at 1.6 BL/s.

$$\begin{aligned} \text{Simplified LSM direct}: \mathbf{X} &= \begin{bmatrix} 0.0285 & -0.1052 & 0.1480 & -0.0085 & 0.0368 \end{bmatrix}^T \\ \text{The empirical model}: \mathbf{X} &= \begin{bmatrix} 0.0271 & -0.0628 & 0.1696 & [-] & [-] \end{bmatrix}^T \end{aligned} \tag{3.56}$$

Chapter 4

Sea bass analysis in OpenFOAM

This chapter builds on the previous work carried out by Schwartz[21]. The starting point for OpenFOAM in this thesis, will thus be to implement the fish form. Schwartz concluded that an overset grid, with two grids seemed promising for a dynamic case. He also pointed out the challenges concerning a proper body fitted grid.

Schwartz had successfully solved and verified the stationary NACA0012 foil case. I will therefor start with creating a foil profile for sea bass and create a boundary fitted grid. I will afterwards investigate the effect that the wall has on the sea bass.

The open source software's OpenFOAM, a C++ toolbox of numerical solvers with CFD capabilities and pre/post-processing applications, was chosen for the numerical simulation [30]. An OpenFOAM case consists of three sub folders as illustrated in figure 4.1. When the case is ran, the information is transferred between the folders.

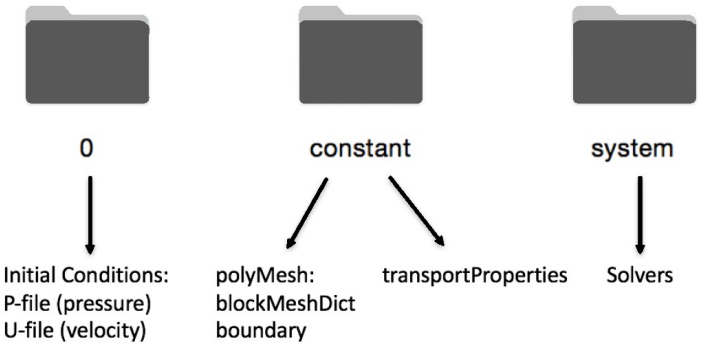

Figure 4.1: The three sub folders in the OpenFOAM folder, Adopted by

4.1 Sea bass case

The fish in the experiment experiences turbulent flow, with Re = $1.05 \cdot 10^5$. The experiment is analysed in 2D, as turbulent flow is a 3D phenomena, the flow is assumed laminar and Re = 1000 is chosen.

The fluid-flow assumptions for this case is:

- 2D laminar flow
- Re= 1000

- Newton fluid
- Neuman BC
- Uniform inflow
- Incompresible, ρ= constant
- Constant viscosity, ν= constant
- Cartesian coordinates

Mesh generation has been both done directly in OpenFOAM with the utilities blockMesh and with ICEM ANSYS CFD, an external mesh generation software and the mesh generated in ICEM has been converted into OpenFOAM format.

The method for solving the numerical simulation is an overset grid. Overset grid is chosen both to save CPU time, as the background is structured and the boundary fitted grid is unstructured, and also because it is practical for moving objects. Overset gird with a structured background mesh of hexahedron elements has been chosen. This choice was taken as it is easier to implement and because OpenFOAM can solve structured mesh more efficiently then unstructured.

The boundary fitted mesh around the fish is chosen as unstructurd, as structured meshes have low adaptability to complex geometries [15]. To get "good" CFD soultion it is evident with a "good" mesh. There exist no clear definition for a "good" mesh, but the quality is generally measured on non-orthogonality, skewness, aspect ratio and smoothness [18].

Sea bass foil

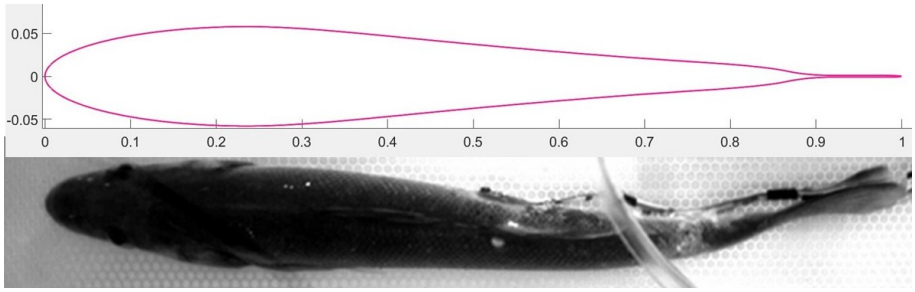

Figure 4.2: The fish foil and the high resolution image

The fish geometry is found from applying the image processing and midline construction for the slow speed high resolution camera. This image is chosen to better reconstruct the true form of the fish, especially in the tail region. The body of fish is smooth, to ensure that the flow around the body is realistic and that the flow is not interrupted by a rough outline and a curve fitting method is used. A smooth outline is also good for the development of standing waves along the body and to reduce skin friction and body drag. The curve fitting method chosen is smoothing spline, as it well predicts the outline and is smooth, as indicated in table 3.1. In addition, the motivation for this study is to improve thrust for AUV's and underwater robotics. Underwater drones are designed smooth to decrease the skin drag and better the pressure distribution on the body. It is therefore of interest to construct the fish foil, with both the actual fish geometry and robotic design in mind.

With the aforementioned in mind, the head to the thickest cross section is given an ellipse form. The curve fitting method is used to reconstruct the fish until the caudal peduncle. From the caudal peduncle to the end of the tail, the reconstruction is based on smooth forms and based on main axes and images of fish.

The created sea bass foil, illustrated against the high resolution images, as shown in figure 4.2, is then imported as MSH file from ICEM CFD Ansys to OpenFOAM.

4.2 Boundary fitted grid

The boundary fitted grid around the fish foil constructed in ICEM ANSYS CFD is shown in 4.3.

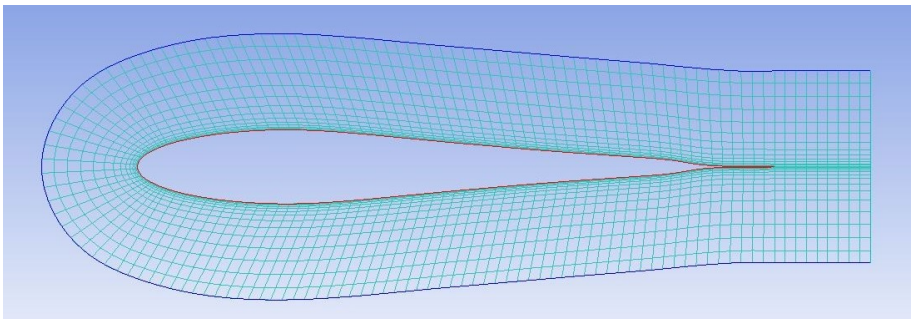

Figure 4.3: The Boundary fitted grid around the fish foil

The overlapping grid transfers information between the grids, and there are numerical errors connected to this transfer. To capture the flow features, it is essential that the boundary fitted grid is outside the boundary layer of the fish. Based on the flatplate assumption from Blasius [**?**]. The boundary layer thickness has been calculated as following:

$$\delta = \frac{4.91x}{\sqrt{Re_x}} \tag{4.1}$$

x is the relative fish length and Re =1000, gives a boundary layer thicknes of 0.0465 BL at 0.3 BL and 0.15 BL at 1 BL. To ensure that the cell size are relatively equal, the boundary fitter grid is chosen to be 0.15 BL around the entire fish foil.

Schwartz concludes that the cells near the foil should be much finer than what he had simulated and he suggests to expand the cell size towards the boundary of the bodyfitted grid [21]. This is suggested to save CPU time and increase the background gird.

As aforementioned, the quality of the mesh is generally measured on non-orthogonality, skewness, aspect ratio and smoothness.

When cells are not square numerical error can be introduced. The cells should be as orthogonal as possible, but OpenFOAM allows for a maximum 70 degrees skewness, but a smaller angle is better. At the fish foil boundary, they should ideally be 90 degrees on the wall.

For a mesh with orthogonal cells there will develop a numerical error if the squares are not aligned with the Cartesian coordinate system. If the cells are not aligned, the information in the flow will be transferred with an angle to the flow direction [19].

For the transfer of information efficiently between cells it is also important the the length of cell sides are as equal as possible. This is measured as aspect ratio, the difference between the minimum and maximum with of cells is small. In addition the a large aspect ratio result in a interpolation error, causing a numerical diffusion. That being said, a large aspect ratio can also save CPU time.

In addition to the aspect ratio it is also important that the cell size are of similar size. Sudden jumps in the size will cause interpolation error, causing a numerical diffusion [26].

With the aforementioned in mind, the grid cell size is decreasing in size towards the boundary. This is done in order to decrease CPU time. The boundary condition for the OpenFoam file, is listed in table 4.1.

Patch	U	p
inlet	fixedValue (1,0,0)	zeroGradient
outlet	zeroGradient	fixedValue (0,0,0)
fish foil	fixedValue (0,0,0)	zeroGradient
fish boundary	overset (1,0,0)	overset (0,0,0)
Top and bottom	zeroGradient	zeroGradient
Front and back	empty	empty

Table 4.1: Boundary conditions

With the aforementioned in mind, a refinement study should be conducted, meaning that cell sizes are decreasing in size until the solution has stabled. It is impotent that the mesh is no to refined, as the this could result in unstable numerical solution [17].

Five refined mesh has been made from the mesh in figure 4.3 and the finest is illustrated in figure 4.4.

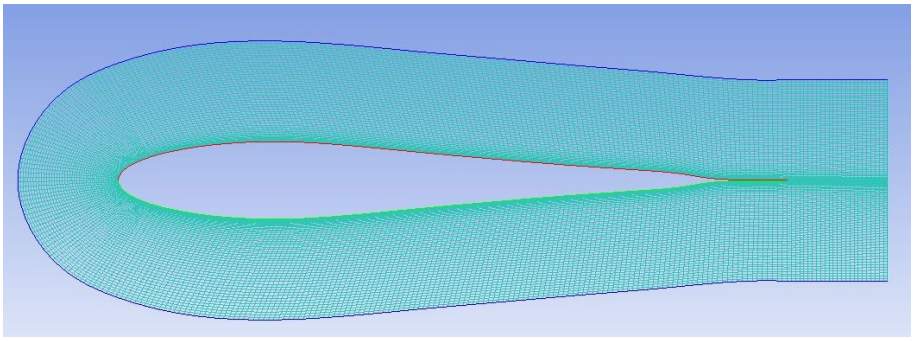

Figure 4.4: finest refined grid size

After 0.7 seconds real time, one can see that the refined mesh has much less numerical error.

Comparing the lift coefficient for the five mesh sizes, with corresponding background mesh, after 0.7 seconds real time, the results in figure Figure E.1 indicate that the two finest refined mesh sizes have converged. This indication is supported with visual inspection of the velocity in the transverse direction, shown in figure 4.2. The figure to the left, 4.5, indicates a numerical instability, while the figure to the right, 4.6, has symmetry.

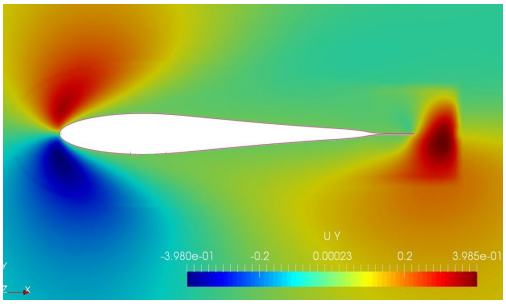

Figure 4.5: Unrefined grid size velocity in transvers direction

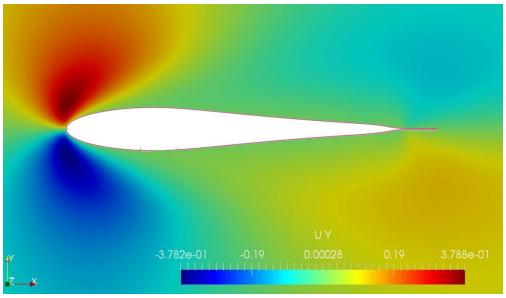

Figure 4.6: Refined grid size velocity in transvers direction

Based on Schwartz suggestion to make the grid finer close to the body and expanding out toward the boundary [21], an investigating was done to improve the second largest mesh sized grid.

From this mesh, five new mesh configurations were made, with a decrease in cell size towards the boundary, but with the same amount of cells in the boundary fitted grid. Figure E.3 indicates that the two grids with the finest mesh close to the body have converged.

$Mesh2_5$ is the most promising and is therefor further investigated. A domain convergence with increased duration was preformed. Figure 4.7 indicates that the solution has not converged as previously supposed. After about 1 second real time, a sudden instability occurs. This result indicates that improving the previously unstable mesh configuration for this case this way is not promising.

To get a satisfied solution the two finest mesh configurations, mesh4 and mesh5 E.2, are now further investigated. To be certain on a stable convergence, the time duration is further increased to 10 seconds real time. I figure 4.8, it indicates that the finest mesh, mesh5, has converged to a stable solution. This is supported by figure 4.9, which indicates an instability at the far end of the tail, while in figure 4.10 the solution appears symmetric. The boundary fitted grid configuration for mesh5 is now chosen to further investigate the wall effect.

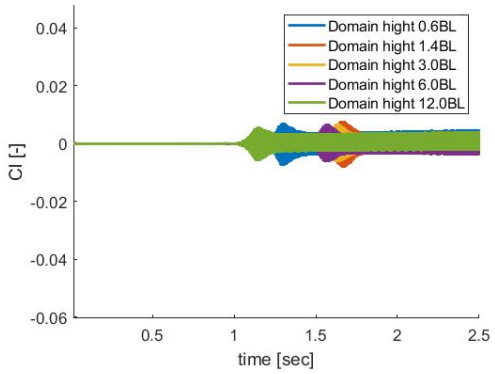

Figure 4.7: grid size

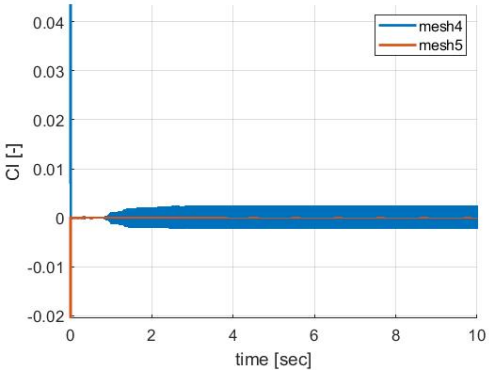

Figure 4.8: grid size

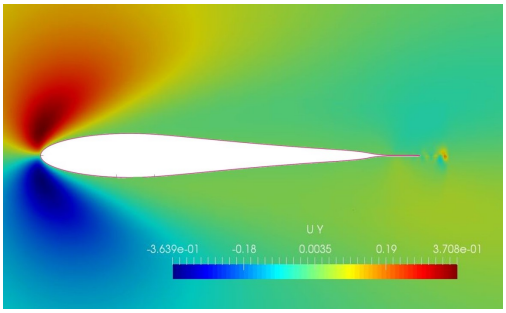

Figure 4.9: finest refined grid size velocity in transvers direction

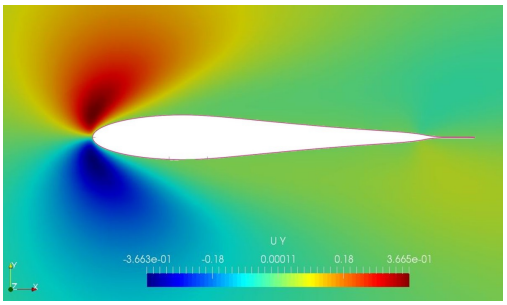

Figure 4.10: second finest size velocity in transvers direction

4.3 Locomotion experiment

Now, a boundary fitted grid that gives stable solution is found. To investigate how mush influence the wall has on the fish, the experimental setup dimensions are imposed to the sea bass case, as indicated in table 4.2.

Patch	U	p
Inlet	fixedValue (1,0,0)	zeroGradient
Outlet	zeroGradient	fixedValue (0,0,0)
Fish foil	fixedValue (0,0,0)	zeroGradient
Fish boundary	overset (1,0,0)	overset (0,0,0)
Top and bottom	fixedValue (0,0,0)	zeroGradient
Front and back	empty	empty

Table 4.2: Wall case boundary conditions

The results indicate that the wall stabilises the flow faster and better, as shown in figure 4.14. Figures 4.11 and 4.12, visually support a stable solution as the flow is symmetric about the midline of the fish. From figure 4.13 it is found the drag coefficients:

- Wall case: $C_d = 0.0200$
- Free domain case: $C_d = 0.0063$

From these results the wall effect give rise to a three times larger drag coefficient than without the wall prescient. This indicates that the fish must use more energy to achieve the same thrust as in a free condition.

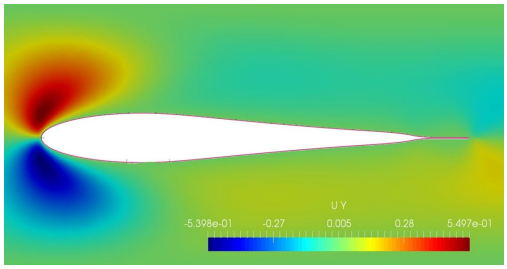

Figure 4.11: Wall case with velocity in transvers direction

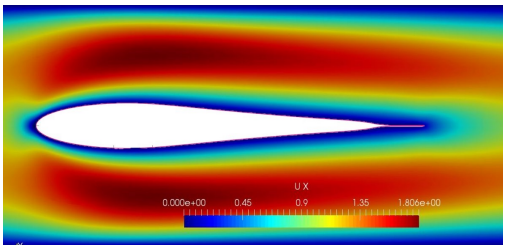

Figure 4.12: Wall case with velocity in flow direction

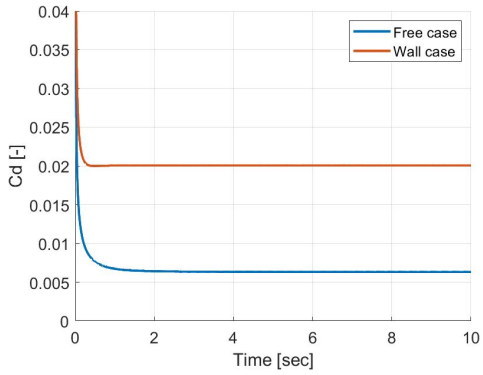

Figure 4.13: Comparsion between drag coefficients for free case and wall case

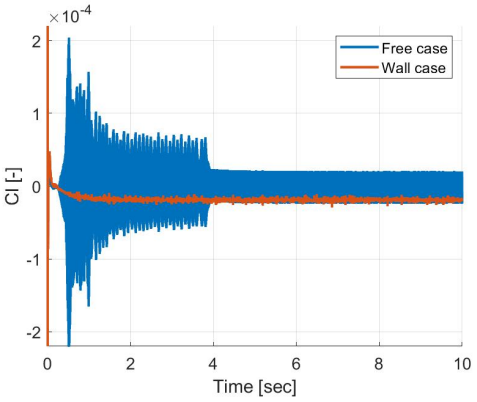

Figure 4.14: Comparsion between lift coefficients for free case and wall case

Chapter 5

Discussions on sea bass analysis

The purpose of this master thesis was to investigate the fish hydrodynamics based on analysis of available sea bass experiments and on numerical studies.

5.1 Locomotion experiments

The two main limits in relation to the experimental setups was the placement of the fish in relation to the walls and an error in calibration. There were also a lot of uncertainty related to the accuracy of the experiment. From the experimental log, provided by Adjunct Professor Claudio Lugni, many possible error sources to the experiment were identifies. There were many problems that occurred under the experiment on which this thesis is based that gave rise to challenges, that have either been accepted or compensated for. Prof. Lugni's initial experiment was conducted to investigate the stable swimming of a sea bass without free surface conditions. For this reason the experiment was done in a closed flow tunnel. With my target of investigating stable swimming in deep water, with application for AUV's and marine robotics, the ideal condition would be to have no walls, as AUV's operates in open waters. This is in practise not possible, because experimental set up with these dimensions would be to expensive and the wall condition will therefore affect the flow. The lid is used to remove the free surface condition, and replaces it with a wall condition. This is desirable because the four walls makes a closed system, than represent deep water condition better then three walls and a free surface, yet it still influences the flow. Consequently, The sea bass will not swim as it would in the wild, and this could result in an unsteady swimming technique. From the investigation of the video provided by Adjunct Professor Claudio Lugni, I have observed that the fish is accelerating a lot under the experiment and that it swims very close to the inlet and the side wall. This will affect both the inflow speed and direction of the fish, as well as making the motion asymmetric. The video I have selected has been chosen based on this and I was only able to select a short time duration, to make sure that the fish did not accelerate. The choice of video is very important as it directly influences the results.With longer videos, including more stable swimming for different inflow velocities, a more broad investigation could be performed. It could also be beneficial to have long videos to remove local changes to the stable motion.

In addition, The experimental design was inherently flawed. The impeller driving the flow was not calibrated and the velocity monitor had a 10% bias error according to the biologist helping out with experiment. long with a small experimental set up, this made it hard to know the exact inflow. The biggest challenge in overcoming the experimental setup, relates to the camera setup. Three low speed high resolution cameras were used in the experiment and one additional high speed low resolution GoPro camera was located on the top of the swimming tunnel. The camera setup only had one camera on each side of the tank, making it unfeasible to get depth in the image and investigate the fish in 3D. Consequently, the hydro analysis had to be performed for a top view 2D. For the 2D analysis of the fish, the low frame rate on the high resolution cameras, resulted in to few captured frames in each period, making it unacceptable for analysing the motion sufficiently. Consequently, the GoPro camera had to be used for analysing the fish motion. The GoPro was not properly tested before the experiment and only every fourth frame

was saved. Further, the placement of the hole for inserting the fish was made so that the outline of the hole cut the fish visually in half. To investigate the fish motion, this resulted in a much more comprehensive image analysis. The fish is attached to two accelerometers. This will most likely influence the swimming characteristics however this is difficult to quantify. These accelerometers are measuring time and are connected with the high resolution cameras by a laser triggered starting mechanism. However, the resolution cameras have a lower frame rate than the GoPro.

Optimally, it would be beneficial to examine a video with longer duration, so as to include many observed fish periods. This is desirable to give less influence from motions deviating from the steady swimming. It is also desirable to have no in-flow accelerations, meaning that the CoM is fixed and equal tail beat frequency. The target is a calm steady swimming and acceleration would therefor interfere with my results. Ideally, there would be no interruption in the image. for my 2D case it would be desirable to have little to no 3D tail effect. The wall effect from the small tank disturbed the flow as a result of the no-slip condition giving rise to velocity differences at the wall, causing the steady swimming to be interrupted and is not ideal, hence the observed motion is not the exact steady motion I wanted to examine.

5.2 Fish identification by image processing

The comprehensive image processing came as a result of the experimental setup. The image process conducted in my project thesis, processed the image with the same thresholds. As a result, this led to the tail not being reconstructed properly for all time frames. This resulted in an inaccuracy when redefining the position on the body in percentage, with respect to the fish length for every image. To improve and overcome this challenge, a semi-automatic image processing procedure was performed. The image was divided into three sections, based on the resolution and equal reconstructing challenges, to ensure that the entire fish was properly reconstructed. The caudal fin had issues with the wire inter- fering with the tail, the high relative movement in reference to the GoPro resolution and the natural 3D effect of the tail. This made it impossible to know where the main axis of the tail was, and it is a bias error from the GoPro. The tail region is the most important part of the fish connected to generating thrust in form of vortex shedding and flow features behind the tail. From visual verification in appendix Figure Figure B.17, it indicates that the midline for the length of the fish is found. The mean midline length is 651.63 pixels, with a standard deviation of 14.2 pixels, which indicates that the length of the fish in each image is accurate.

5.3 Midline construction by curve fitting

To compensate for the rough midline, different curve fitting methods were examined. Several of the methods try to best fit functions through the initial midline points. The prescribed curvature can give fundamentally wrong midline predictions. They have the tendency to curve the tail based on the curvature building up to the tail. This prediction can either be very precise or completely wrong. As the tail is the part with the most uncertainty, it has been concluded that it is better to use a method that only directly evaluates midline points or predicts a point based on the closed points. This is done to make sure that further errors are not added. From the visual verification B.34, the fitted line is much smoother and follows the midline well. The verification indicates that Movmean and Pchip combination is a well imposed choice and gives a good prediction for each frame in a period of swimming.

To get from a smooth midline for every frame to function in space and time, a Fast Fourier Transform was used. This evaluates 21 evenly spaced points along the body and evaluates each one by one.. The FFT predicts a best fitting cosine function to the midline point in time. The closer the function is in amplitude and form, the better the prediction. Figure C.1 indicates that FFT constructing is well imposed, but the change in position and minor accelerating changes effects can be observed as an inconsistency in the difference between the FFT input and the midline points in time. Based on the combination of these 21 processed signals, the main amplitudes along the body have the same frequency.

Based on the amplitude with this exact dominating frequency the function for the amplitude development along the body is found through a polynomial curve fitting procedure. The combined wave number and phase shift is found the same way. Figures 3.44 and 3.44 both are indicating a well posed curve through all the points. To get the cure for the wave number and the phase shift, the points had to be corrected for a phase shift at approximately 0.24 BL.

From the FFT, a simplified fish motion in time and space has been created. The midline form can be seen in figure 3.45 and the entire form is illustrated in figure 3.46. Figure B.51 indicates that the FFT is able to impose the motion for the fish, when reapplying the removed noise onto the FFT result.

From the FFT result, the wave number is found from removing the amplitude in time and finding the half of the wave length for every time step. The wave length is 0.8578 BL with a standard deviation of 0.0348 BL. This indicates that the wavelength is as expected and accurate.

To verify the FFT results, a function based on the travelling index of BCF fish analyzed from biological data is used. From figure 3.46, the travelling indexes are found using the definitions in figure 2.14. Based on these indexes, a new function is made and plotted, as seen in figure 3.51. From comparing the slopes in figure 3.50, the agreement is good. The empirical amplitude has a lower minimum point.

5.4 Locomotion extraction

Towards the goal of identifying the locomotion of the sea bass from the experiment, it is essential that the entire motion of the fish contributes to the solution. From the FFT, only certain parts of the motion were considered and these parts were heavily edited. When treating the signal and finding trends, the authentic signal is lost. The advantage of this is that local errors from the midline ensure no influence to the signal. The drawback of editing the signal is that one has to ensure that it does not give the signals characteristics that it does not have. An additional weakness to not using the initial signal, is that the method and procedure is not easy to apply to different cases. To find a method that is easy to reapply for another application, is essential for this thesis, as the heaviest challenge was related to the image quality. The quality of cameras is improving fast and future research may benefit from improved camera technology. Using a method where the quality is connected to the initial midline, the method will be improved and become better with technology, and will therefore contribute more towards finding the best replication of the fish motion.

The LSM is a method which is used directly on the initial midline. The result is therefore not influenced by reconstruction of the midline, as in the case of the FFT. For a well-resolved fish image, this method would be beneficial. For this thesis the image of the initial fish is not sharp enough. This results in a rough outline and the midline will consequently become uneven. When using the initial midline as input for the LSM, deviations from the actual midline will get to influence the results. The SVD identifies the best fitting solution to the target solution. It is difficult to quantify how much influence the deviating points have on the solution, as a result of the SVD. The local deviation can be interpreted as high frequency noise to the low frequency signal being the smooth midline. From investigating the effect high frequency has on LSM ability to filter out noise and identifying functions, the effect of the rough midline will affect the results, however the tendency is kept.

The quality of the LSM is cobbled with the quality of the reference law. For both simplifications in this analysis, the domination frequency and the wave number identified from the simplified FFT solution is applied. This means that the models try to fit the midline points to a motion with a prescribed wave number and tail beat frequency. With the best fitting principle in mind, different frequencies will not influence the result much and influence of local deviation is minimised. In this case, with a low of high-frequency on the midline, this assumption improves the results. The drawback is that other larger minority contribution frequencies are not considered. This will affect the quality of the function. The trade-off is connected to the complexity of the linearization and the challenges this leads to. A more complex linearized system increases the possibility for more accurate results, but it will also introduce new challenges and therefore demand more from the user.

From the results of prescribing the FFT solution as the evaluated midline points for both the oversimplified and simplified LSM, it is clear that the simplified LSM results are not properly resolved for the effect of phase shift. The oversimplified LSM is expected to give a less accurate result, but in this case it is not restricted by a non- physicality. When evaluation with the LSM, it is therefore desirable to perform the investigation for multiple levels of restriction and complexity, to ensure that the results are physical.

The oversimplified LSM is not considering phase shift and the method has no physical restrictions. It therefore provides a good verification to the simplified method. The oversimplified LSM indicates that

the results are affected if additional noise is added. The results from applying the midline direct to the LSM is expected not to be exact.

For the simplified LSM the biggest challenge is to overcome the non-physical aspect of phase shift. It is also also important to ensure that the results are physical with respect to the form of the locomotion and recoil. This has to be done manually and demands that the user is familiar with these forms. For the sea bass, this means that the center of recoil is placed in the front part of the fish and that the locomotion amplitude does not change sign. a thorough investigation on what to expect, is therefore required. This is done by investigating simplified models that minimize the chance of large non physical errors. From the results of prescribing a locomotion and recoil motion to the simplified LSM, the errors connected to recovering the signal when adding noise, is much smaller than for the oversimplified LSM. The problem with the results is that the signs coefficients are not the same. This indicates that there is a phase shift that is not properly taken care off. When applying the the simplified LSM directly on the initial midline, the problem is not there. The solution is very close to the direct solution for the oversimplified LSM setup, and this indicates that the method works and that the identified locomotion is the best replication of the locomotion from the experimental swimming.

When comparing the locomotion from the FFT solutions and direct solution, it is clear that the tendency of the amplitude slope is found. The simplified LSM on the midline has a very similar form to the over-simplified LSM FFT solution, this indicates that the simplified LSM is able to capture the locomotion properly with the assumptions made. From the empirical method of creating the locomotion from the scaling parameters found by biological data, the parameters for this locomotion is found and compared with different fish. The original FFT solution was placed between the Largemouth Bass Swim at 2.4 BL/s and the Saithe, while the simplified LSM solution is placed closest to one of the two references on the Largemouth bass Swim at 1.6 BL/s. As there is an uncertainty with the flow speed and the wall effect, which can force the fish to swim with a higher tail beat frequency than for the same prescribed inflow in infinite water. A consequence of the fish now swimming on a fixed location, is that the fish is acceleration and the quality of the initial midline, the direct method is expected not to be exact and therefore is a close comparison to the Largemouth bass Swim at 1.6 BL/s, is very promising for the method.

5.5 Sea bass analysis in OpenFOAM

OpenFOAM is used for numerical investigation. Overlapping mesh is used to set up the case. Overlapping mesh was chosen to build on the previous work done by the last Masters student on this topic, Schwartz. He studied a standard NACA foil, for steady and oscillating motion. I have therefore chosen to start with a fish foil replica of the sea bass from the experiment. To create the outline of the fish it is important that the physical aspect of the outline for the fish is adhered. It is most important that the flow behaves similarly to the real fish. It is therefore essential that the outline is smooth and symmetric about the spine. These assumptions are also practical for AUV' and underwater robotics, as they will be constructed smooth and no sudden pressure build up.

When creating the boundary fitted grid, the size is decided from the Blasus formula for boundary layer for a flat plate. The boundary thickens at the tail is given to the entire boundary fitted grid. The fish is not a flat plate, so the boundary layer is expected to be larger, but it is also desirable to create a boundary fitted grid with the midline of the fish given the prescribed motion. Then the midline is curved, a two large boundary will cause very small or very large cells close to the outer boundary. The larger the boundary layer, the larger the error. To ensure that cell size around the fish equal, the boundary layer is given the same size around the fish and the thickens are therefore prescribed by Blasus.

When choosing the cell size inside the boundary fitted grid, there is a trade-off to consider. If all cell sizes are squared and in line with the flow, then the solution will be very clear, but it will demand a lot of CPU time. It is desirable to have a fast code and background grid is desirable to have as large as possible. To make sure that the solution is kept but the CPU time is decreased, a decreasing cell size is chosen toward the fish boundary. This ensures that the physical changes in the flow in the boundary layer is kept. The problem with decreasing cell size is behind the flow, where multiple cells are transferring information to the outer domain cell. This will create a numerical error, but it is accepted to save time.

From the investigation of making the grid size as large as possible, the results indicate that the solution becomes unstable after one second real time. The boundary fitted grid chosen is the largest cell size

with a stable solution.

When having chosen the boundary fitted grid, the wall effect in the experiment was investigated. A case with an outer domain 10 times larger than the thickens of the fish is chosen for infinite water condition and the experimental dimension is decided by the dimension of the tank. The drag coefficient is 4 times as large with the wall present, then without the wall. In reality the drag on the fish will not be this large, as the drag is a complex 3D phenomenon. This numerical simulation is done in 2D but the flow in the tunnel is turbulent. The flow is moving faster in the middle of the tank then by the wall. This is because of the friction drag on the wall. In the 2D case all the water is compressed between the fish and the wall, this is not the case in 3D. The compressed water because of the presence of the fish in 3D is the square root of the compression in 2D. Thus the additional drag caused by the wall is considerably smaller, but has an effect on the motion of the fish.

Chapter 6

Conclusions and further work

6.1 Summary and Conclusions

From the preliminary work the propulsive contribution to the thrust was identified as the momentum transfer mechanism between drag, lift and acceleration reaction forces. The Reynolds number for the sea bass in the analysed experiment is $1.05 \cdot 10^5$ and it is in the expected range 2.1. The sea bass undulatory BCF mode is subcarangiform. Because the sea bass has a wave length, 0.86 BL, shorter than the body length, the subcarangiform of the sea bass is therefor expected to consist of locomotion and recoil. Maertens mathematical expressions for these motion are use to separate the locomotion and recoil from the combined fish motion [14]. The mathematical formula by Cui et al.[5], to reconstruct the locomotion from scaling parameters is used for verifying the separated locomotion.

There were many things that went wrong under the experiment, which results in many unknown errors, which reduce the possibility to verify the test and results from the image analysis. For the image analysis a semi-automatic iterative image cleaning process was constructed to identify and retrieve the outline of the fish from the image. The mean midline length was found to be 651.63 pixels with a standard deviation of 14.21 pixels.

From the initial midline a corrected midline was created, to compensate for the rough midline. The combined curve fitting method Movmean and Pchip was used to smooth the initial midline. Based on this cure fitted midline, a Fast Fourier Transform was used to identify a simplified fish motion function. The domination frequency was found to be 4.9558 Hz and the wave number to be 7.325 BL^{-1}.

To separate the locomotion and recoil from the fish motion the Least Squares Method, a least square fitting process, is used for two levels of simplifications. It is investigated for a prescribed fish motion on the same form as Maertens [14] and it works for both of them, but is sensitive to additional noise. The verification for separating the Fast Fourier Transform solution was working for the most simplified Least square method, but it had a problem with recovering the phase shift for the simplified method. For the Least Squares Method used directly on the initial midline, both methods worked and were able to identify the locomotion.

OpenFOAM was used to numerically investigate the effect of the wall on the fish. The wall effect results in a larger drag on the fish and the locomotion separated with Least Squares Method is expected to be locomotion for a sea bass swimming faster than 1 BL/s.

6.2 Recommendations for Further Work

For the next experiment conducted on fish, I would suggest to compensate for the fish being stressed. I would recommend to let the fish swim for a longer period of time with low speed before increasing the speed for the experiment. It is important that the fish is comfortable in a closed tunnel, before conduction the experiment.

The GoPro had very low resolution, and the tail consequently became blurred into the background, making it difficult to distinguish them apart. For further work, an investigation on different background colors or material on the background should be done in order to minimize this effect.

I would recommend to investigate into the use of machine learning to identify the fish motion, if the quality of the images are better.

From the investigation of the locomotion extraction, the biggest problem has been to overcome the physical aspects of phase shifts. The method indicates that it works, thus a more thorough investigating into the separation of the motion should be done. Different ways to linearized the Left Hans Side of the equation system should also be investigated.

Further work connected to the numerical investigation in OpenFOAM, should be to improve the boundary fitted grid and to impose the locomotion function to investigate if or how much thrust the locomotion is able to generate by itself.

Bibliography

[1] B. Allotta, A. Caiti, R. Costanzi, F. Fanelli, D. Fenucci, E. Meli, and A. Ridolfi. A new AUV navigation system exploiting unscented kalman filter. *Ocean Engineering*, 113:121–132.

[2] D. S. Barrett. The design of a flexible hull undersea vehicle propelled by an oscillating foil.

[3] Q. Bone and R. H. Moore. *Biology of fishes*. Taylor & Francis.

[4] C. M. Breder. *The Locomotion of Fish*, volume vol. 4.

[5] Z. Cui, Z. Yang, L. Shen, and H. Jiang. Complex modal analysis of the movements of swimming fish propelled by body and/or caudal fin. *Wave Motion*, 78:83–97.

[6] T. O. Fossum. Intelligent autonomous underwater vehicles. page 29.

[7] F. Fucile. Deterministic sea wave and ship motion forecasting: from remote wave sensing to prediction error assessment. pages 55–102, 2016.

[8] S. Holzner. How the principle of conservation of momentum works. URL `https://www.dummies.com/education/science/physics/how-the-principle-of-conservation-of-momentum-works/`.

[9] B. G. K. *An introduction to fluid dynamics*. Cambridge University.

[10] B. Lantos and L. Márton. *Nonlinear control of vehicles and robots*. Springer-Verlag.

[11] M. J. Lighthill. Hydromechanics of aquatic animal propulsion. *Annual Review of Fluid Mechanics*, 1(1):413–446, .

[12] M. J. Lighthill. Note on the swimming of slender fish. *Journal of Fluid Mechanics*, 9(2):305–317, .

[13] J. Liu and H. Hu. Mimicry of sharp turning behaviours in a robotic fish. In *Proceedings of the 2005 IEEE International Conference on Robotics and Automation*, pages 3318–3323. IEEE.

[14] A. P. Maertens, A. Gao, and M. S. Triantafyllou. Optimal undulating swimming for a single fish-like body and for a pair of interacting swimmers. *Journal of Fluid Mechanics*, 813:301–345.

[15] A. Moraes and P. Lage. Analysis of the non-orthogonality correction of finite volum discretization on unstructured meshes. pages 1–12, 2013.

[16] A. J. Murphy and M. Haroutunian. Using bioinspiration to improve capabilities of underwater vehicles. 17th International Unmanned Untethered Submersible Technology Conference (UUST): 22–31, 2011.

[17] A. Paul and G. M. Durbin. *Fluid Dynamics with a Computational Perspective*. United States of America by Cambridge University Press, New York, 2007.

[18] R. Peyret. *Handbook of computational fluid mechanics*. Academic Press, 1996.

[19] J. Rhoads. Openfoam workshop 2014: Effects of grid quality on solution accuracy. pages 1–8, 2014.

[20] M. Rufo and M. Smithers. GhostSwimmer™ AUV: Applying biomimetics to underwater robotics for achievement of tactical relevance. *Marine Technology Society Journal*, 45(4):24–30.

[21] J. D. L. Schwartz. Towards the hydrodynamic study of a 2d fish-like geometry during locomotion. (2), 2019.

[22] M. Sfakiotakis, D. Lane, and J. Davies. Review of fish swimming modes for aquatic locomotion. *IEEE Journal of Oceanic Engineering*, 24(2):237–252.

[23] S. STS. Compressible vs. incompressible media. URL `https://campaign.stssensors.com/blog/pressure-measurement-compressible-media`.

[24] M. S. Triantafyllou and G. S. Triantafyllou. An efficient swimming machine. *Scientific American*, 272(3):64–70.

[25] M. S. Triantafyllou, G. S. Triantafyllou, and D. K. P. Yue. Hydrodynamics of fishlike swimming. *Annual Review of Fluid Mechanics*, 32(1):33–53.

[26] H. K. Versteeg and W. Malalasekera. *An introduction to computational fluid dynamics: the finite volume method*. Pearson Education Ltd, 2nd ed edition.

[27] C. S. Wardle, J. J. Videler, and J. D. Altringham. TUNING IN TO FISH SWIMMING WAVES: BODY FORM, SWIMMING MODE AND MUSCLE FUNCTION. page 9.

[28] P. W. Webb. Form and function in fish swimming. *SCIENTIFIC AMERICAN*, page 17.

[29] E. C. website. Knuth: European seabass. URL `https://ec.europa.eu/fisheries/marine_species/farmed_fish_and_shellfish/seabass_en`.

[30] H. G. Weller, G. Tabor, H. Jasak, and C. Fureby. A tensorial approach to computational continuum mechanics using object-oriented techniques. *Computers in Physics*, 12(6):620.

Appendix A

The travelling index of BCF fish analyzed from the biological data.

biological data, is brought together by Cui et al. [5] is in table **??**. The different scaling parameters of the midline motion of BCF fish are listed. The references in the table below is the ones from Cui et al. [5].

Fish names	Fish categories	s_2(BL)	s_3(BL)	s_4(BL)	λ(BL)	Travelling index
Goldfish (Carassius auratus) common type [73]	Subcarangiform	0.0581	0.1744	0.3372	0.882	0.623
Goldfish (C. auratus) comet type [73]	Subcarangiform	0.0535	0.1497	0.3209	0.772	0.720
Goldfish (C. auratus) fantail type [73]	Subcarangiform	0.0562	0.152	0.4045	0.667	0.623
Goldfish (C. auratus) eggfish type [73]	Subcarangiform	0.0958	0.1617	0.4371	0.698	0.770
Bonnethead shark [72]	Subcarangiform	0.0	0.16 ~ 0.2	0.0	0.85 ~ 0.97	0.67 ~ 0.71
Zebrafish [74]	Subcarangiform	0.0	0.275	0.2	1.0	0.665
Blacktip shark [72]	Subcarangiform	0.0	0.16 ~ 0.2	0.0	0.98 ~ 1.16	0.62 ~ 0.67
Rainbow trout [75]	Subcarangiform	0.156	0.936	0.25	0.95	0.626
Juvenile [76]	Subcarangiform	0.018	0.126	0.25	0.5 ~ 1.0	0.60 ~ 0.78
Tiger musky [77]	Subcarangiform	0.147	1.018	0.0	0.8	0.769
Rainbow trout [77]	Subcarangiform	0.358	0.994	0.2	0.9	0.777
Rainbow trout [70]	Subcarangiform	0.0	0.12	0.0	0.7 ~ 1.3	0.61 ~ 0.77
Teleosts [14,34]	Subcarangiform	0.25	1.0	0.3	0.9	0.627
Leopard shark (Triakis semifasciata)[71]	Subcarangiform	0.02	0.1	0.3	0.517 ~ 0.957	0.58 ~ 0.76
Zebrafish larva [60]	Subcarangiform	0.0413	0.2004	0.24	0.816	0.692
Leopard shark [72]	Subcarangiform	0.0	0.16 ~ 0.24	0.0	0.63 ~ 0.91	0.68 ~ 0.78
Mackerel [59,78]	Carangiform	0.02	0.1	0.25	0.95	0.649
Saithe and mackerel [35,79]	Carangiform	0.02	0.1	0.25	0.89 ~ 1.1	0.62 ~ 0.66
Caranguiform fish [80]	Carangiform	0.004	0.024	0.25	0.8971	0.639
Largemouth bass [2,5,15]	Carangiform	0.004	0.024	0.25	0.9	0.638
Largemouth bass Swim at 0.7 BL/s [27,81]	Carangiform	0.0065	0.055	0.4	0.8	0.757
Largemouth bass Swim at 1.6 BL/s [27,81]	Carangiform	0.0185	0.072	0.35	0.8	0.586
Largemouth bass Swim at 0.7 BL/s [15]	Carangiform	0.0041	0.0472	0.3	0.59 ~ 0.83	0.58 ~ 0.68
Largemouth bass Swim at 1.2 BL/s [15]	Carangiform	0.0053	0.0576	0.3	0.59 ~ 0.83	0.58 ~ 0.68
Largemouth bass Swim at 1.6 BL/s [15]	Carangiform	0.0153	0.0651	0.3	0.59 ~ 0.83	0.64 ~ 0.73
Largemouth bass Swim at 2.0 BL/s [15]	Carangiform	0.0165	0.0718	0.3	0.59 ~ 0.83	0.64 ~ 0.73
Largemouth Bass Swim at 2.4 BL/s [15]	Carangiform	0.0181	0.0741	0.3	0.59 ~ 0.83	0.64 ~ 0.733
Saithe (Pollachius virens) [35]	Carangiform	0.018	0.095	0.25	0.64 ~ 1.0	0.63 ~ 0.75
Mackerel (Scomber scombrus) [35]	Carangiform	0.019	0.1075	0.35	0.63 ~ 0.83	0.55 ~ 0.63
Mackerel/Saithe [62,82]	Carangiform	0.1	1.0	0.0	1.0	0.708
Carp [62,82]	Carangiform	0.1	1.0	0.0	1.25	0.642
Scup [62,83,84]	Carangiform	0.1	1.0	0.0	1.54	0.576
Cod [85]	Carangiform	0.043	0.156	0.25	0.93	0.703
Carangiform fish [86,87]	Carangiform	0.0408	1.0	0.0	1.0	0.613
Mullet fish (slip ratio 0.7) [88]	Carangiform	0.0061	0.0928	0.0	0.92 ~ 1.30	0.61 ~ 0.71
Mullet fish (slip ratio 0.9) [88]	Carangiform	0.0061	0.0717	0.0	0.80 ~ 1.38	0.60 ~ 0.75
Mullet fish (slip ratio 1.1) [88]	Carangiform	0.0061	0.0661	0.0	0.50 ~ 0.98	0.71 ~ 0.844
Mullet fish [88]	Carangiform	0.0378	0.13	0.26	0.74 ~ 1.11	0.68 ~ 0.76

Appendix B

Midline construction

B.1 Initial midline construction

The initial midlines from the the video, after having identified the outline of the fish for each frame. The following section consists frame 1 to 13 out of the 113 frames evaluated. The frame rate is 25 frames pr. sec.

Figure B.1: Initial midline, frame development from frame 1 to frame 3

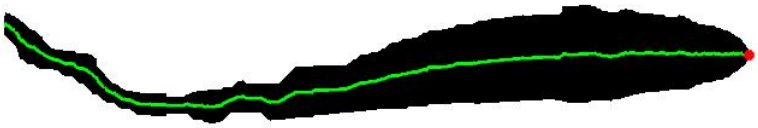

Figure B.2: frame 1

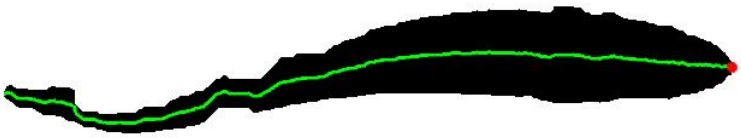

Figure B.3: frame 2

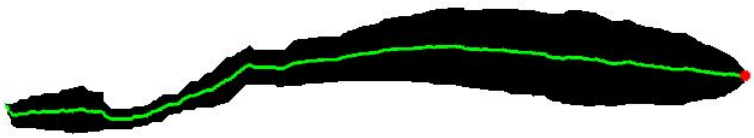

Figure B.4: frame 3

Figure B.5: Initial midline, frame development from frame 4 to frame 8

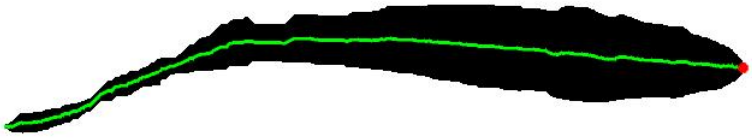

Figure B.6: frame 4

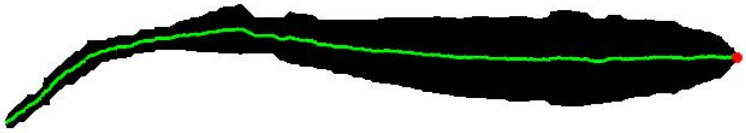

Figure B.7: frame 5

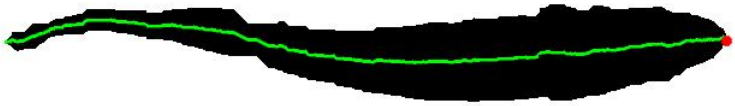

Figure B.8: frame 6

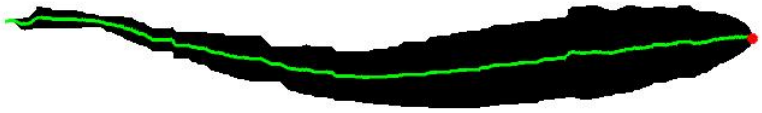

Figure B.9: frame 7

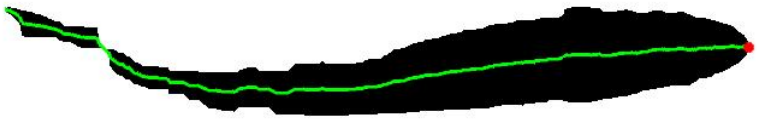

Figure B.10: frame 8

Figure B.11: Initial midline, frame development from frame 9 to frame 13

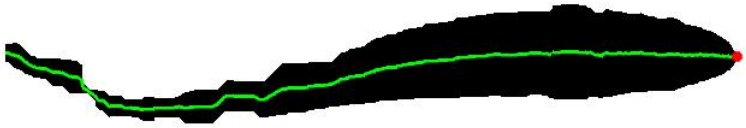

Figure B.12: frame 9

Figure B.13: frame 10

Figure B.14: frame 11

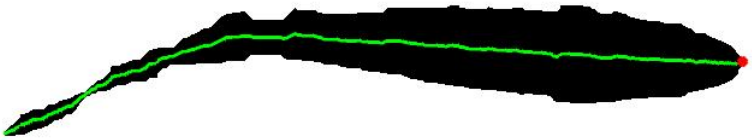

Figure B.15: frame 12

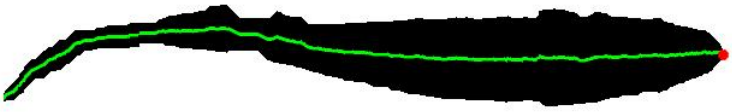

Figure B.16: frame 13

B.2 Initial midline

The initial midline plotted against for the initial image for visual inspection. The following section consists frame 1 to 14 out of the 113 frames evaluated. The frame rate is 25 frames pr. sec.

Figure B.17: Initial midline verification, frame development from frame 1 to frame 4

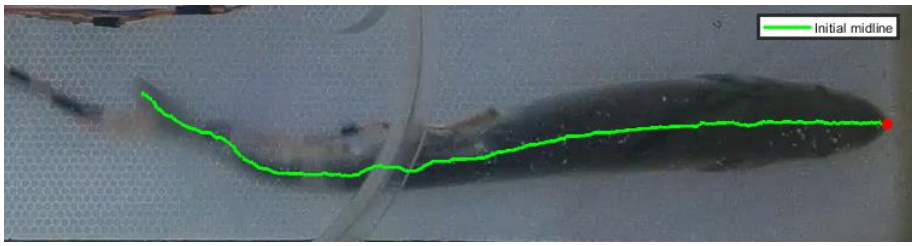

Figure B.18: frame 1

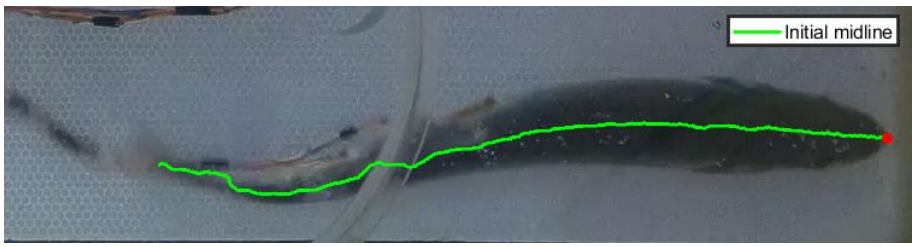

Figure B.19: frame 2

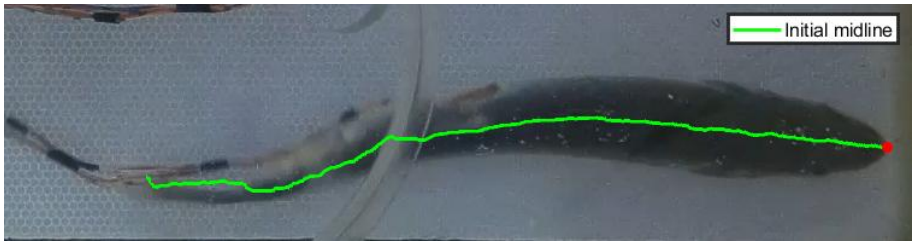

Figure B.20: frame 3

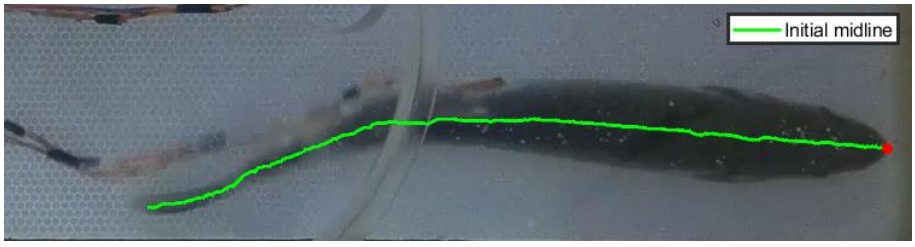

Figure B.21: frame 4

Figure B.22: Initial midline verification, frame development from frame 5 to frame 9

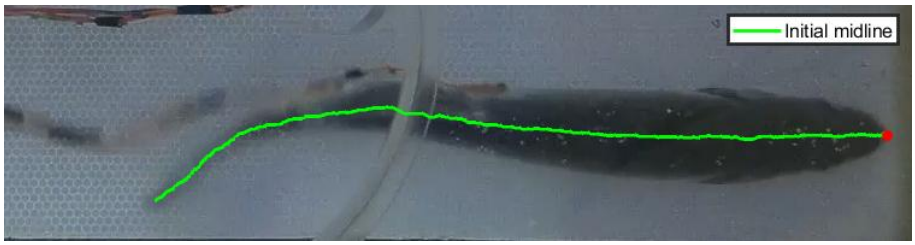

Figure B.23: frame 5

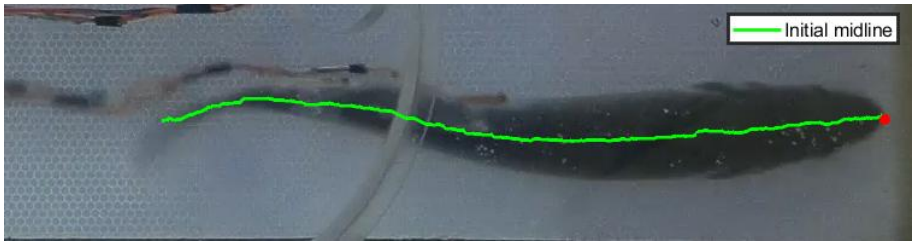

Figure B.24: frame 6

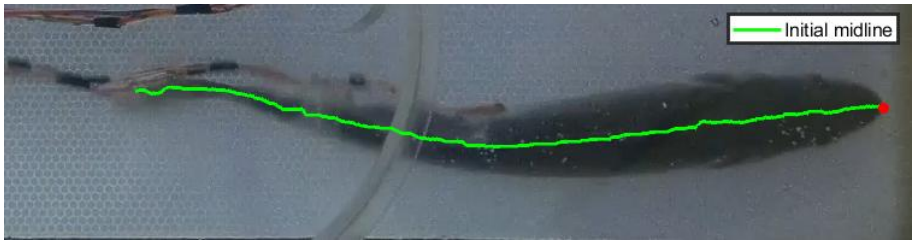

Figure B.25: frame 7

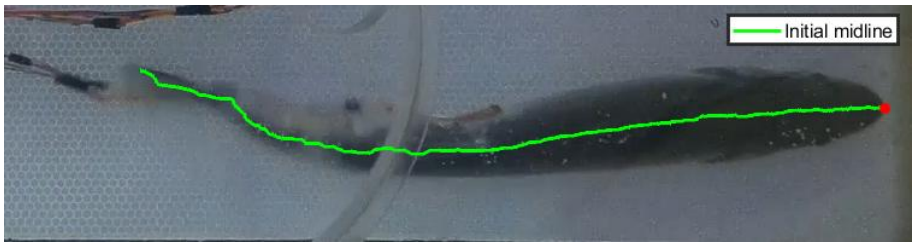

Figure B.26: frame 8

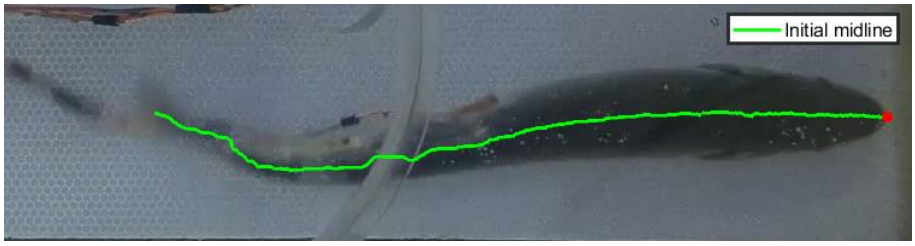

Figure B.27: frame 9

Figure B.28: Initial midline verification, frame development from frame 10 to frame 14

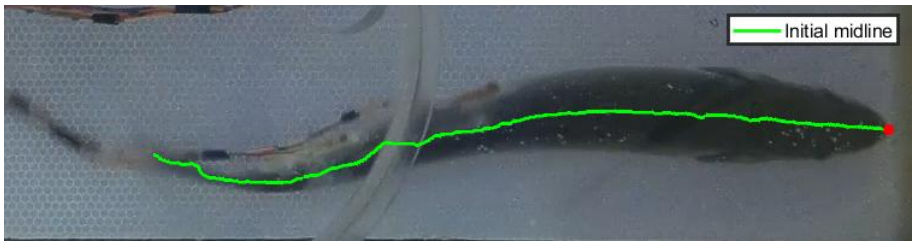

Figure B.29: frame 10

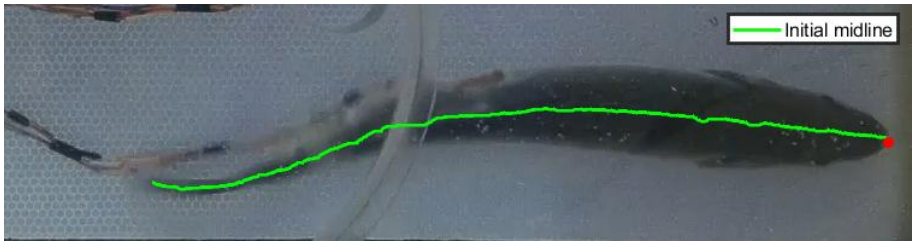

Figure B.30: frame 11

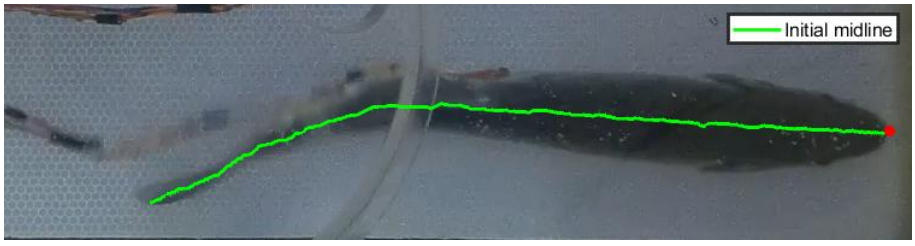

Figure B.31: frame 12

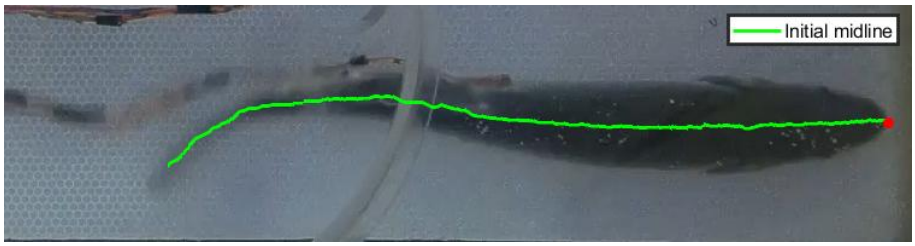

Figure B.32: frame 13

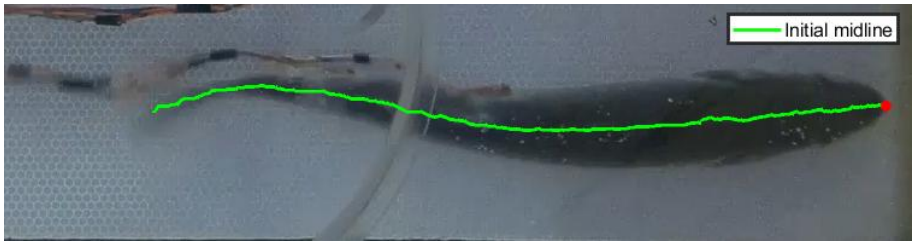

Figure B.33: frame 14

B.3 Curve fitted midline

The curve fitted midline, smoothing the initial midline. The following section consists frame 1 to 14 out of the 113 frames evaluated. The frame rate is 25 frames pr. sec.

Figure B.34: Curve fitted midline, frame development from frame 1 to frame 4

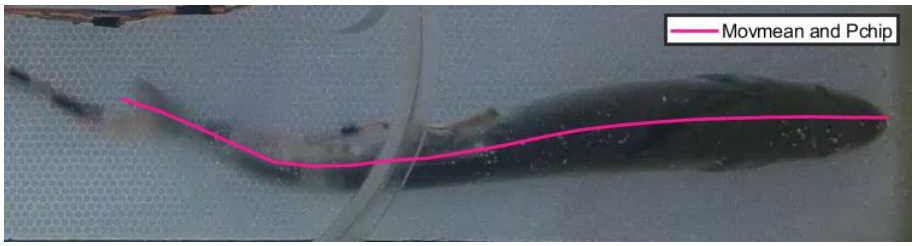

Figure B.35: frame 1

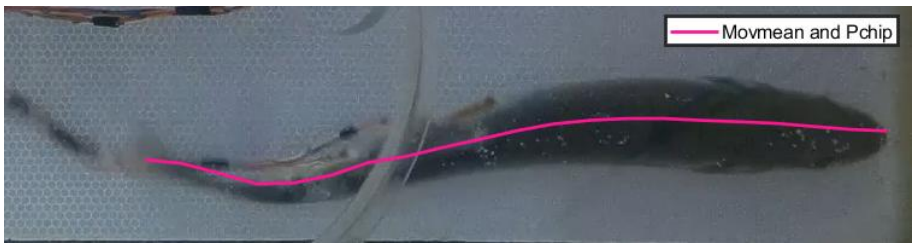

Figure B.36: frame 2

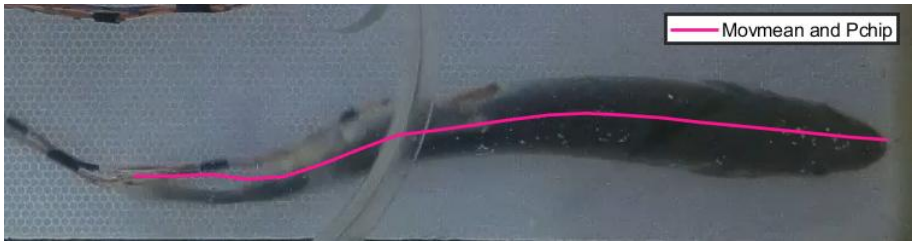

Figure B.37: frame 3

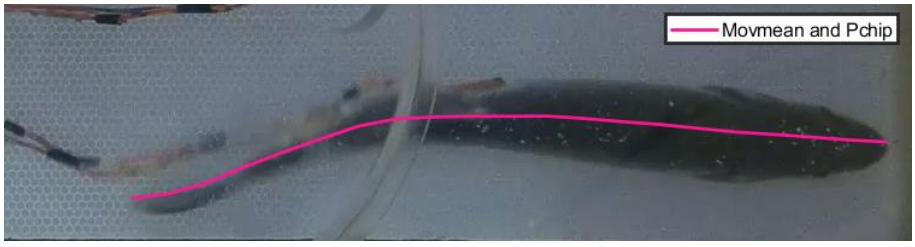

Figure B.38: frame 4

Figure B.39: Curve fitted midline, frame development from frame 5 to frame 9

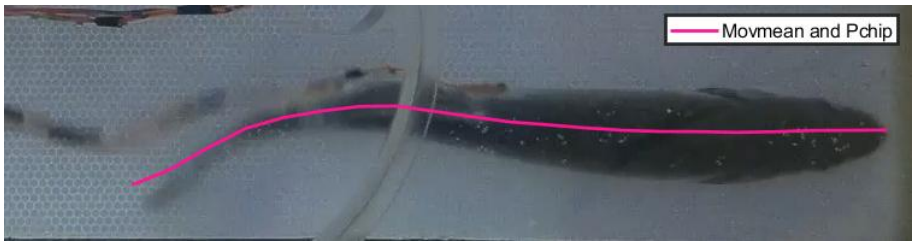

Figure B.40: frame 5

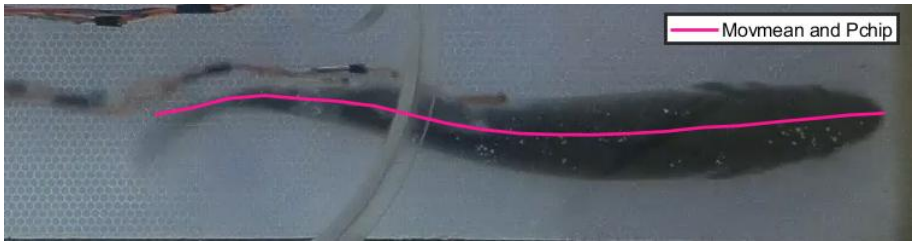

Figure B.41: frame 6

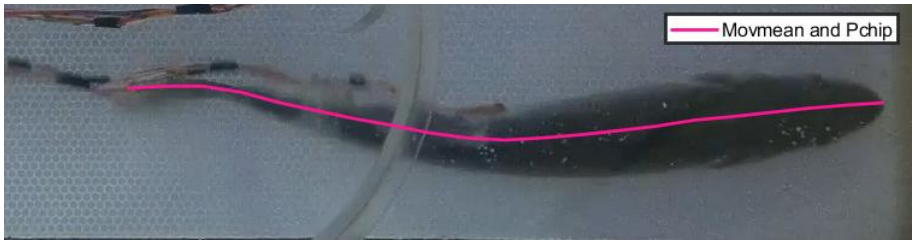

Figure B.42: frame 7

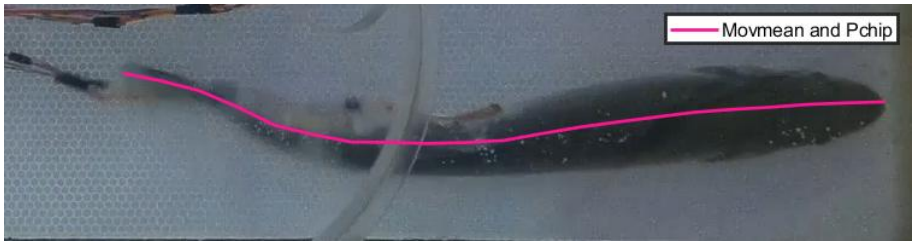

Figure B.43: frame 8

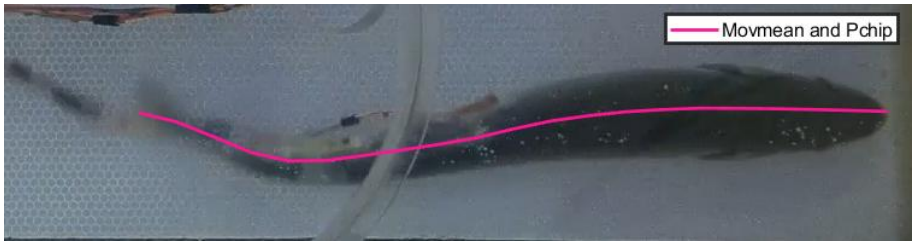

Figure B.44: frame 9

Figure B.45: Curve fitted midline, frame development from frame 10 to frame 14

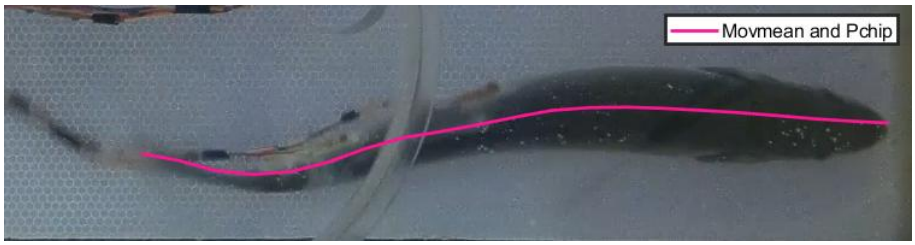

Figure B.46: frame 10

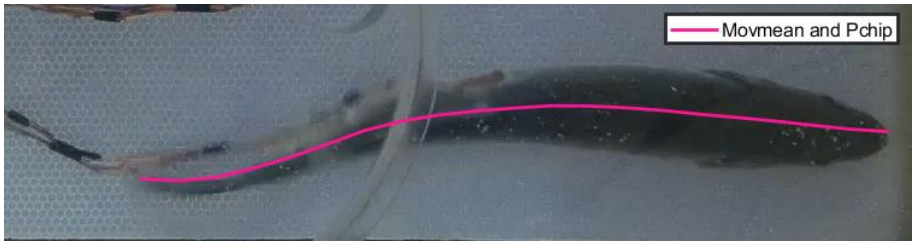

Figure B.47: frame 11

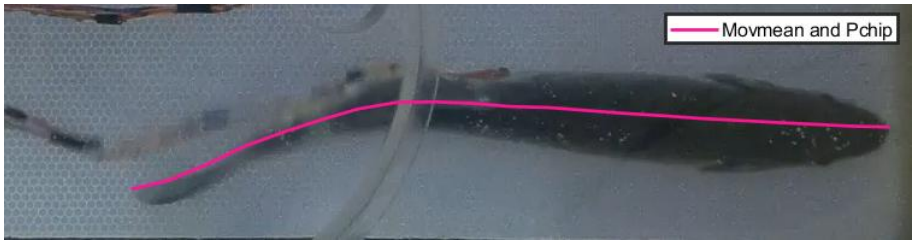

Figure B.48: frame 12

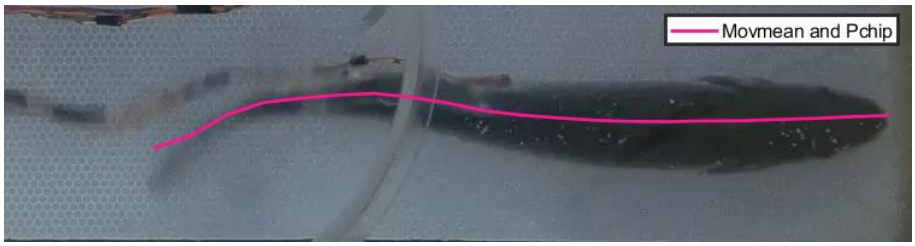

Figure B.49: frame 13

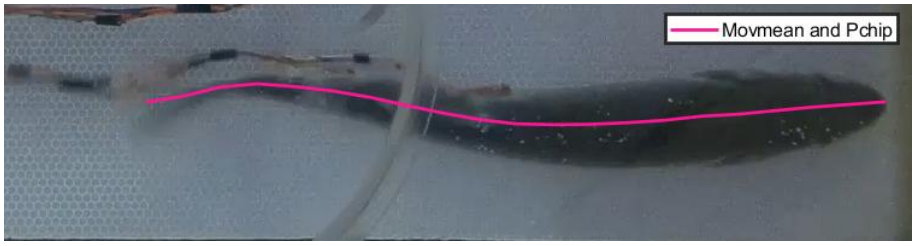

Figure B.50: frame 14

B.4 Midline from FFT with reapplied noise

The midline from FFT with reapplied noise. The following section consists frame 1 to 14 out of the 113 frames evaluated. The frame rate is 25 frames pr. sec.

Figure B.51: Midline from FFT, frame development from frame 1 to frame 4

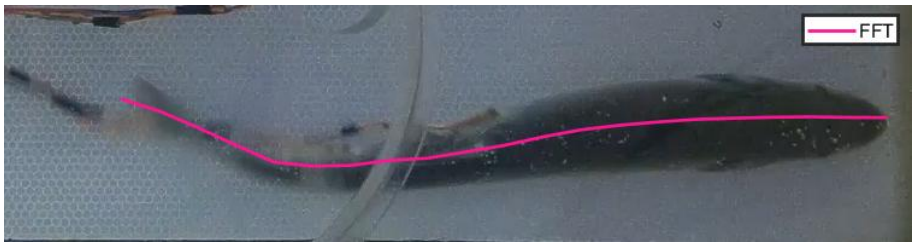

Figure B.52: frame 1

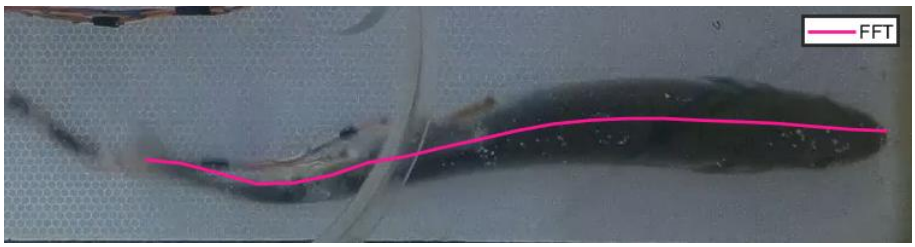

Figure B.53: frame 2

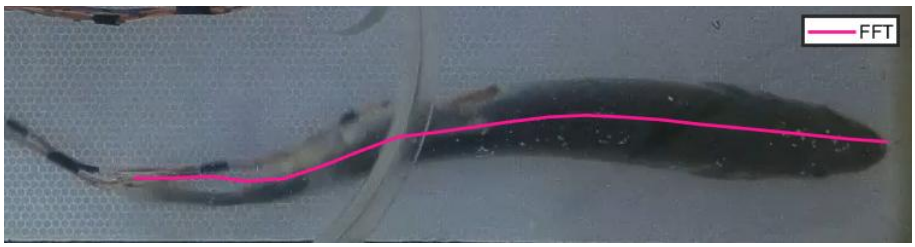

Figure B.54: frame 3

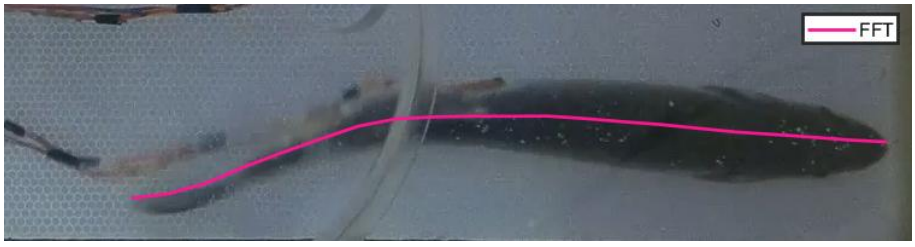

Figure B.55: frame 4

Figure B.56: Midline from FFT, frame development from frame 5 to frame 9

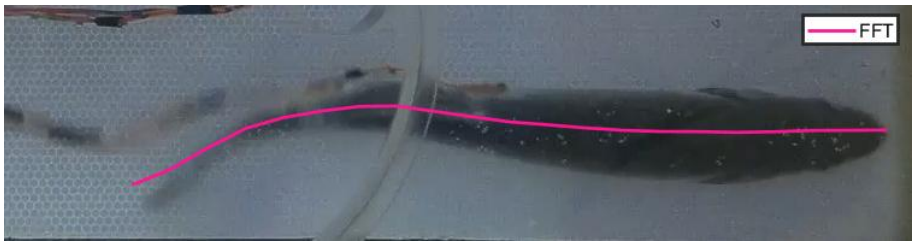

Figure B.57: frame 5

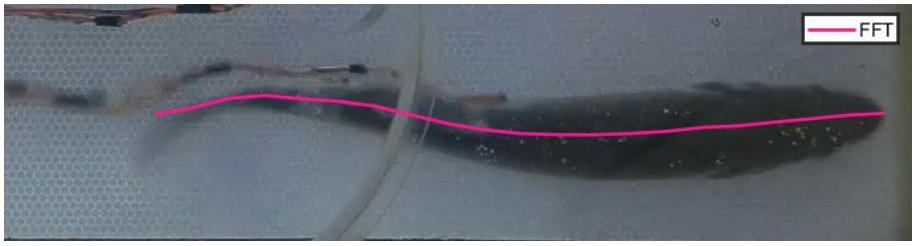

Figure B.58: frame 6

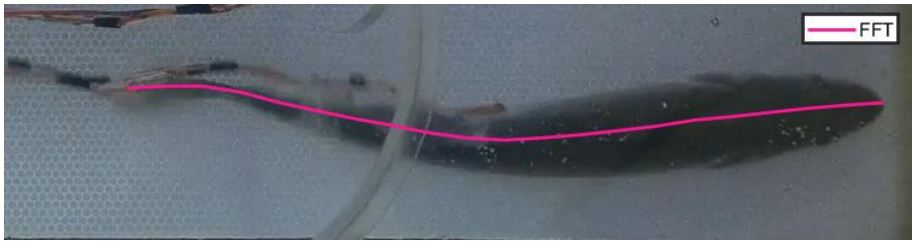

Figure B.59: frame 7

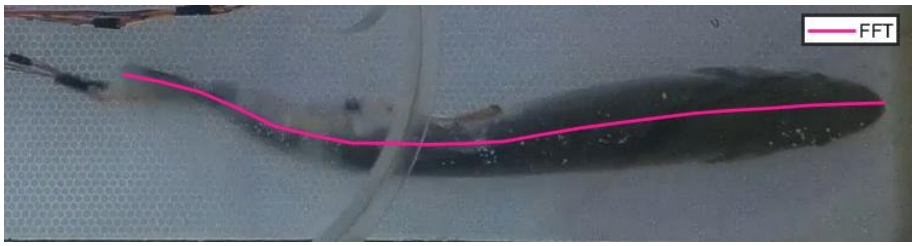

Figure B.60: frame 8

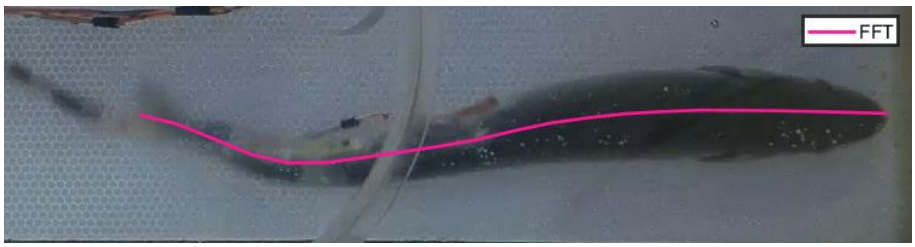

Figure B.61: frame 9

Figure B.62: Midline from FFT, frame development from frame 10 to frame 14

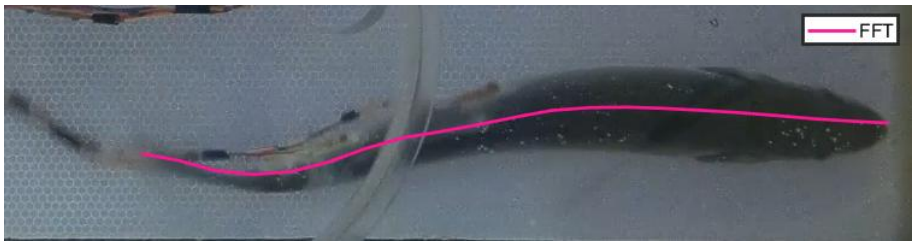

Figure B.63: frame 10

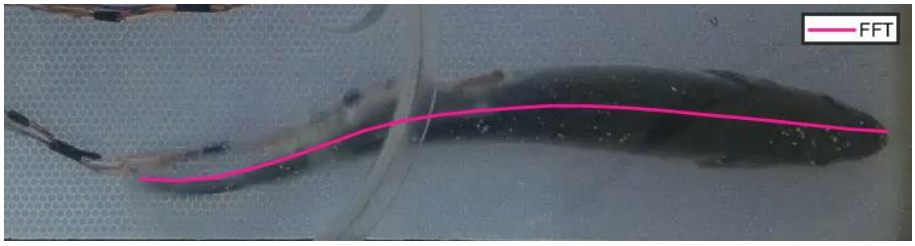

Figure B.64: frame 11

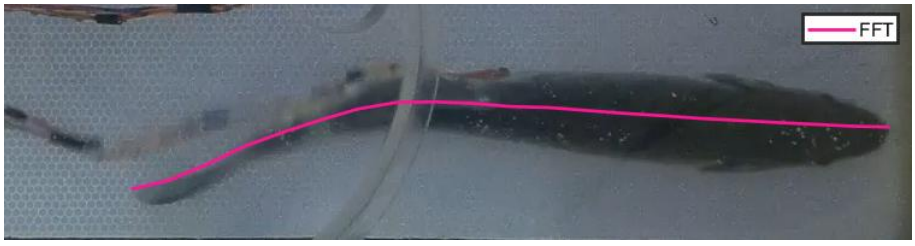

Figure B.65: frame 12

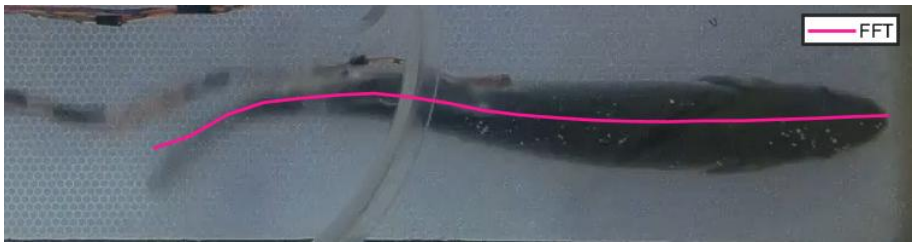

Figure B.66: frame 13

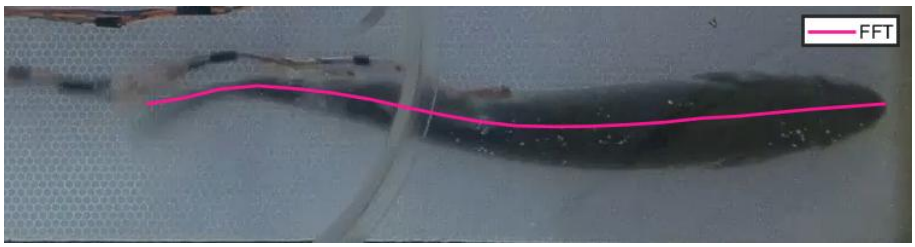

Figure B.67: frame 14

B.5 Midline from the simplified LSM locomotion

The midline from simplified LSM locomotion. The following section consists frame 1 to 14 out of the 113 frames evaluated. The frame rate is 25 frames pr. sec.

Figure B.68: LSM Midline, frame development from frame 1 to frame 4

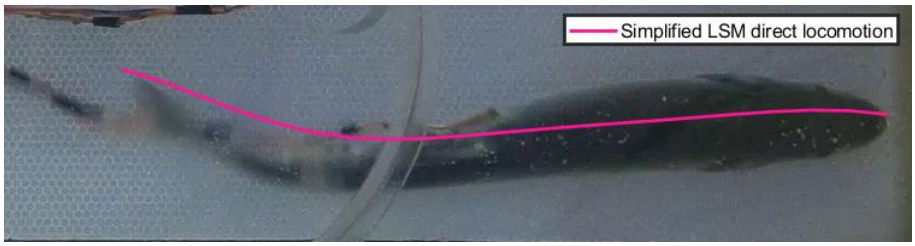

Figure B.69: frame 1

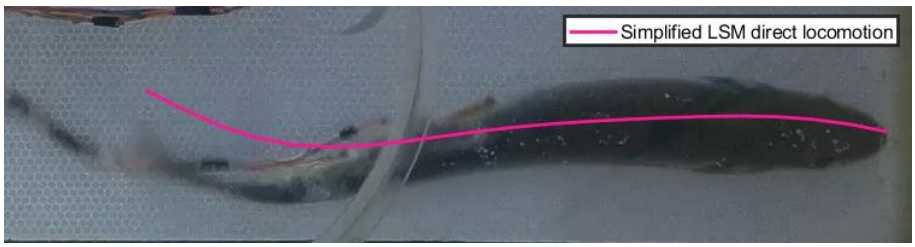

Figure B.70: frame 2

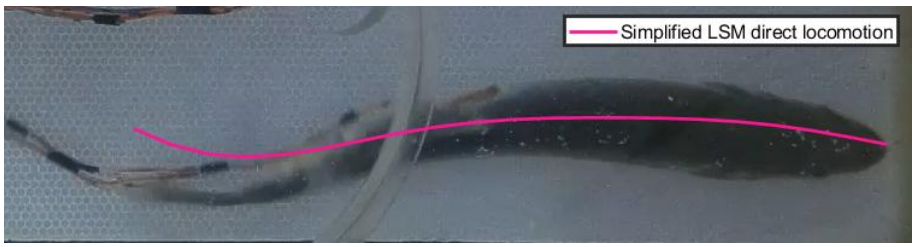

Figure B.71: frame 3

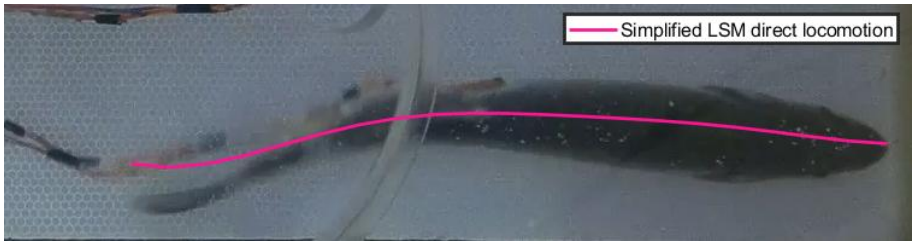

Figure B.72: frame 4

Figure B.73: LSM Midline, frame development from frame 5 to frame 9

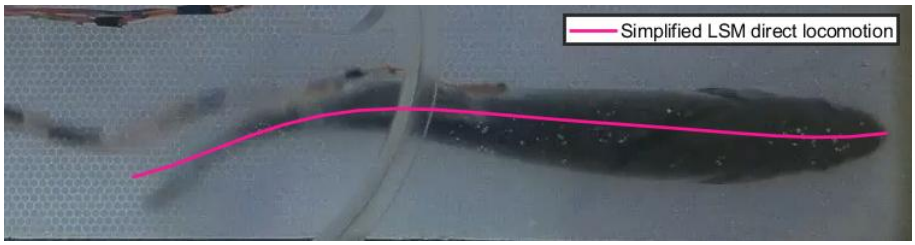

Figure B.74: frame 5

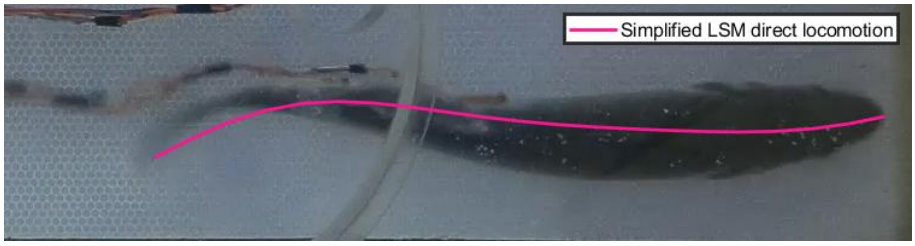

Figure B.75: frame 6

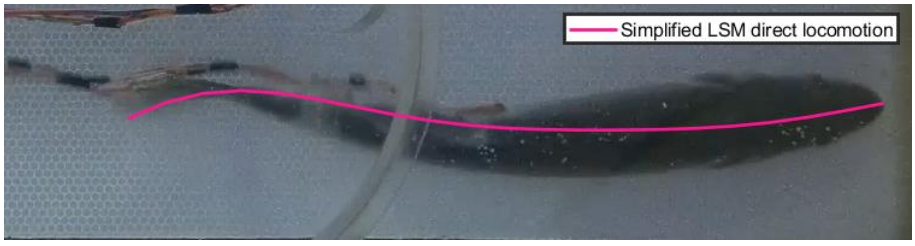

Figure B.76: frame 7

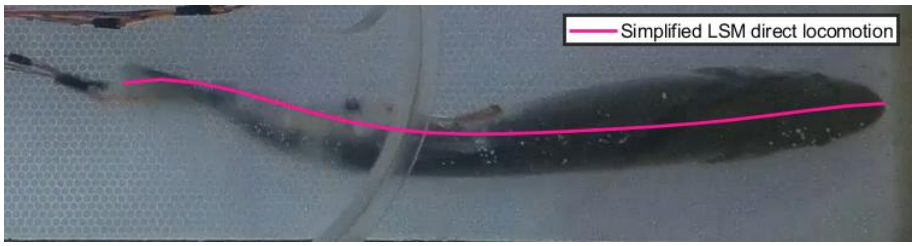

Figure B.77: frame 8

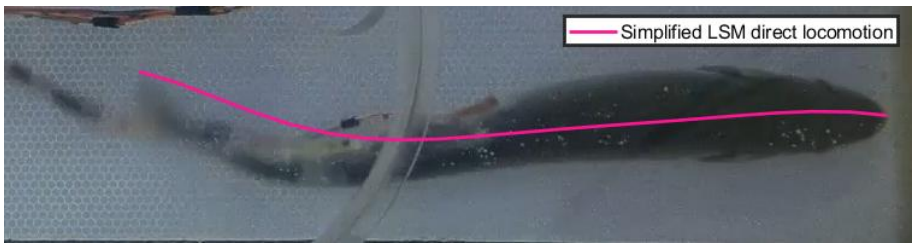

Figure B.78: frame 9

Figure B.79: LSM Midline, frame development from frame 10 to frame 14

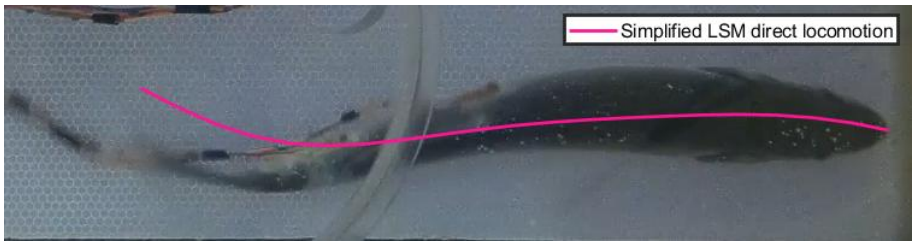

Figure B.80: frame 10

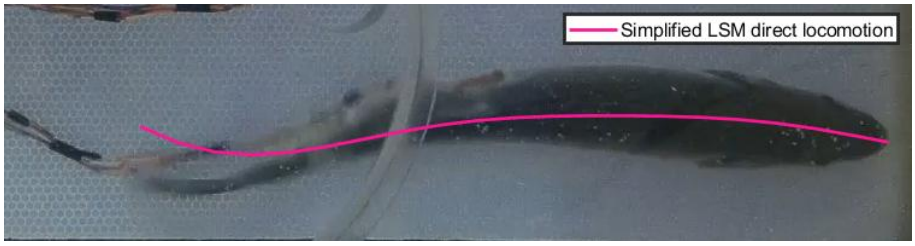

Figure B.81: frame 11

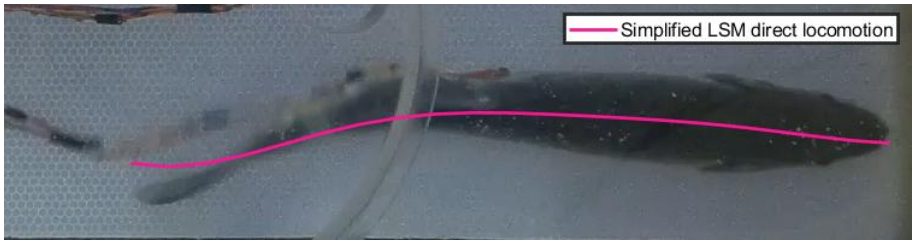

Figure B.82: frame 12

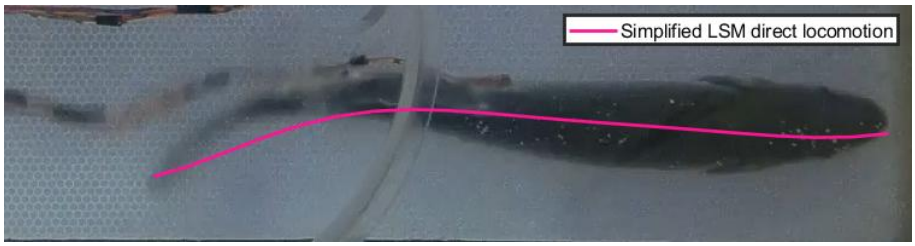

Figure B.83: frame 13

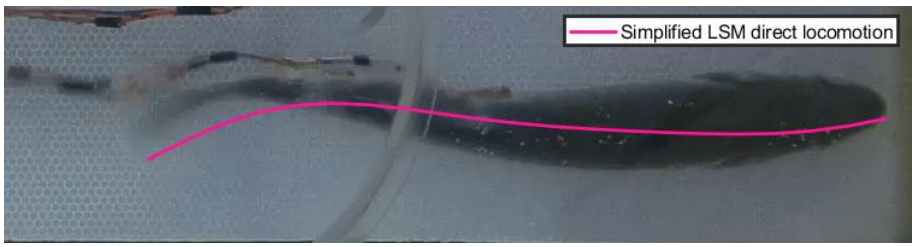

Figure B.84: frame 14

Appendix C

Midline Reconstruction

C.1 Input for the FFT

The linearization of every 21 evenly spaced points in time and only considers the dominating frequency, as the evaluated FFT signal.

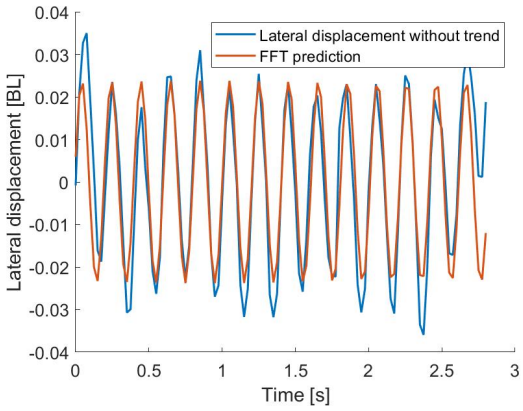

Figure C.1: Lateral displacement for 0 percent body length [BL] in time [s]

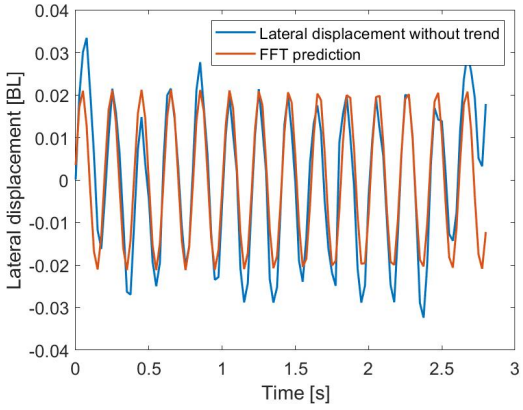

Figure C.2: Lateral displacement for 5 percent body length [BL] in time [s]

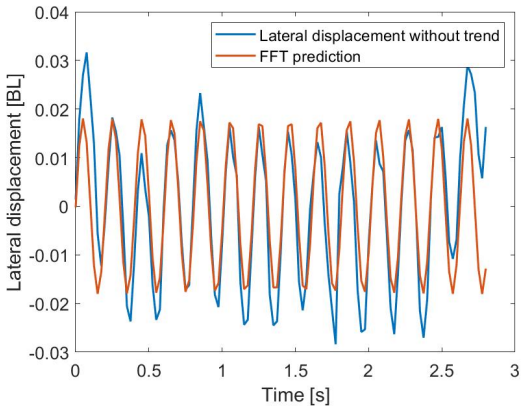

Figure C.3: Lateral displacement for 10 percent body length [BL] in time [s]

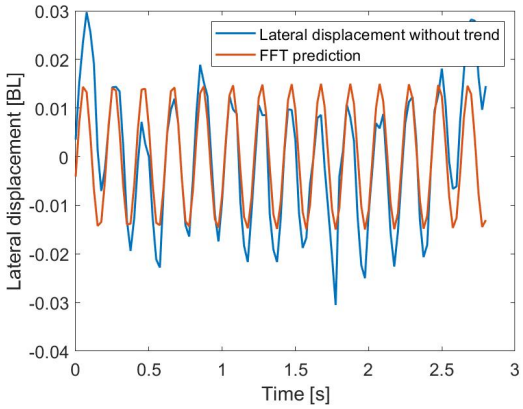

Figure C.4: Lateral displacement for 15 percent body length [BL] in time [s]

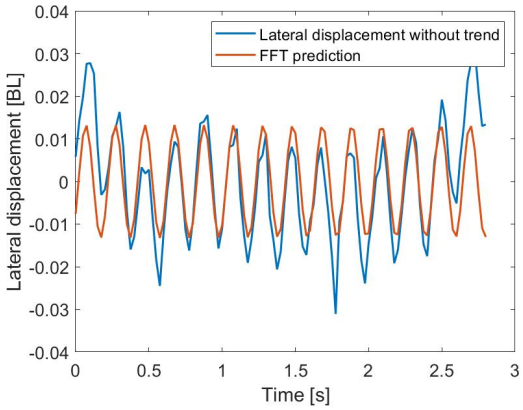

Figure C.5: Lateral displacement for 20 percent body length [BL] in time [s]

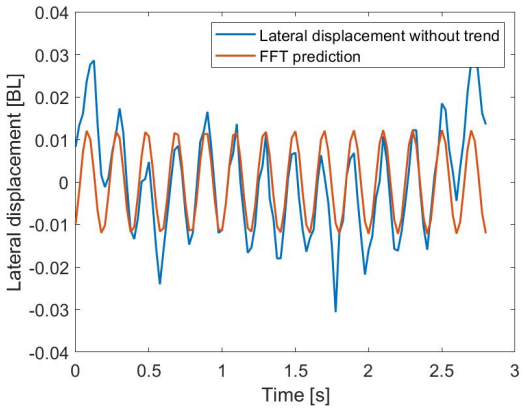

Figure C.6: Lateral displacement for 25 percent body length [BL] in time [s]

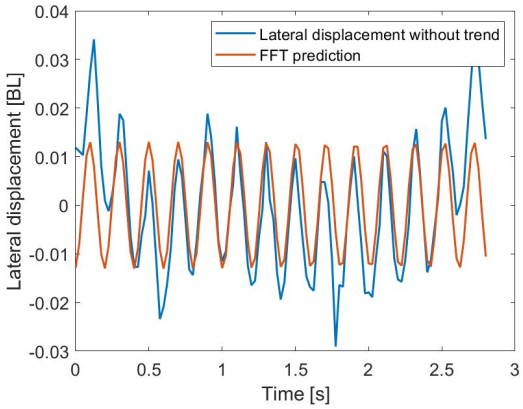

Figure C.7: Lateral displacement for 30 percent body length [BL] in time [s]

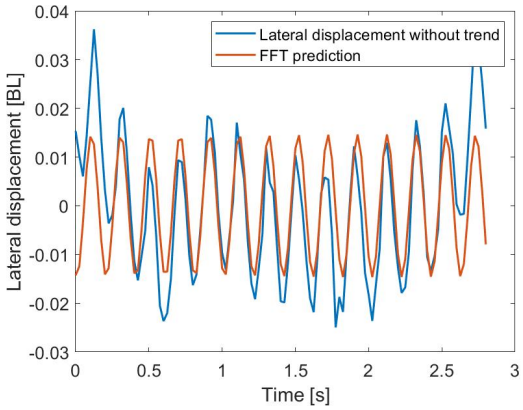

Figure C.8: Lateral displacement for 35 percent body length [BL] in time [s]

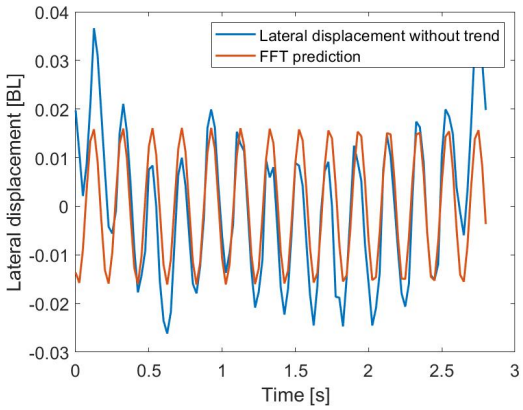

Figure C.9: Lateral displacement for 40 percent body length [BL] in time [s]

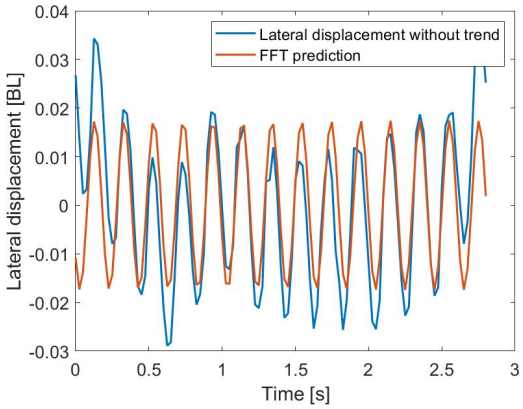

Figure C.10: Lateral displacement for 45 percent body length [BL] in time [s]

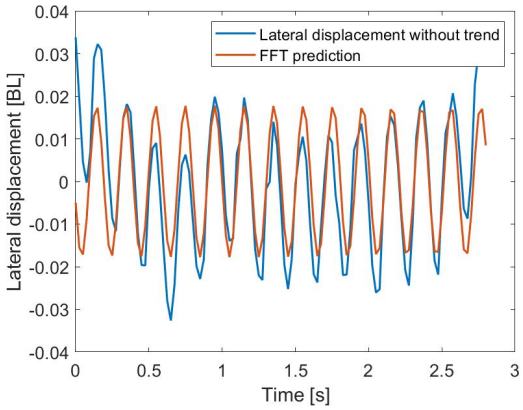

Figure C.11: Lateral displacement for 50 percent body length [BL] in time [s]

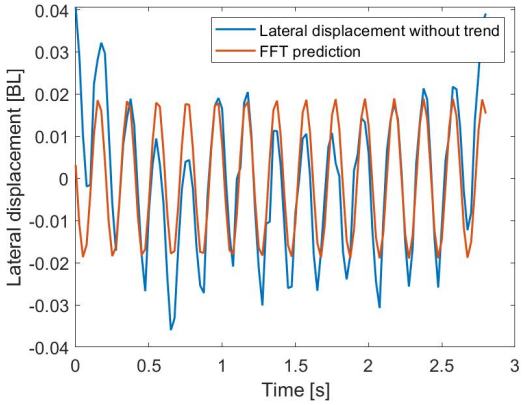

Figure C.12: Lateral displacement for 55 percent body length [BL] in time [s]

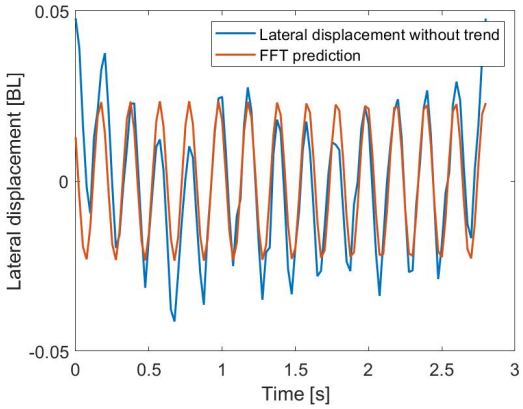

Figure C.13: Lateral displacement for 60 percent body length [BL] in time [s]

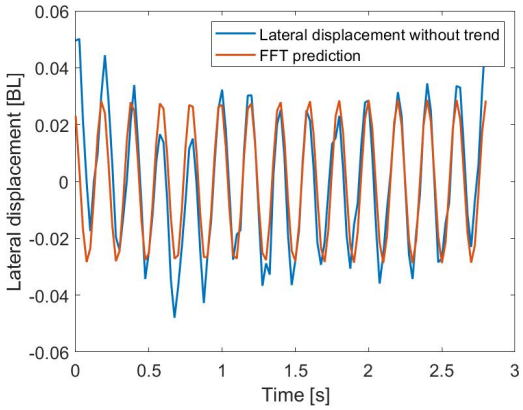

Figure C.14: Lateral displacement for 65 percent body length [BL] in time [s]

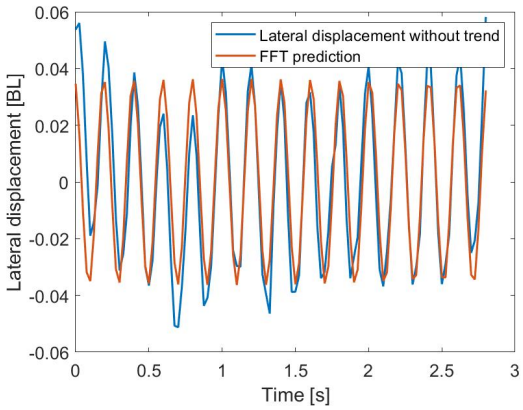

Figure C.15: Lateral displacement for 70 percent body length [BL] in time [s]

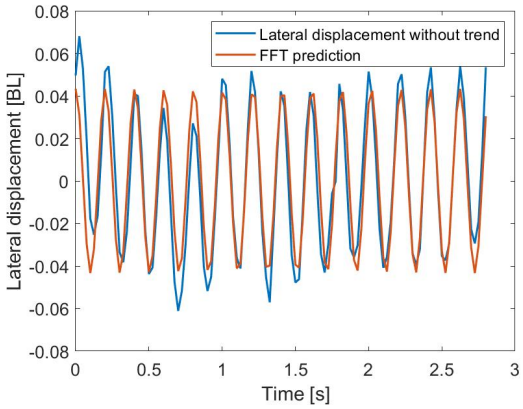

Figure C.16: Lateral displacement for 75 percent body length [BL] in time [s]

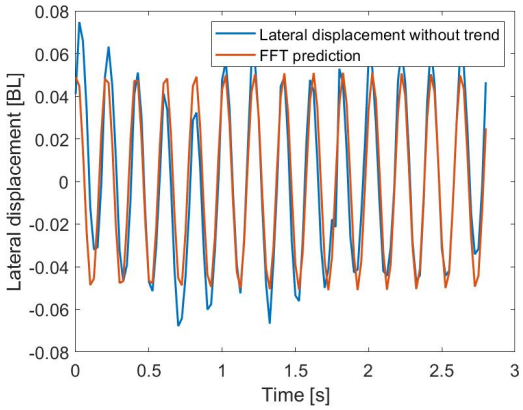

Figure C.17: Lateral displacement for 80 percent body length [BL] in time [s]

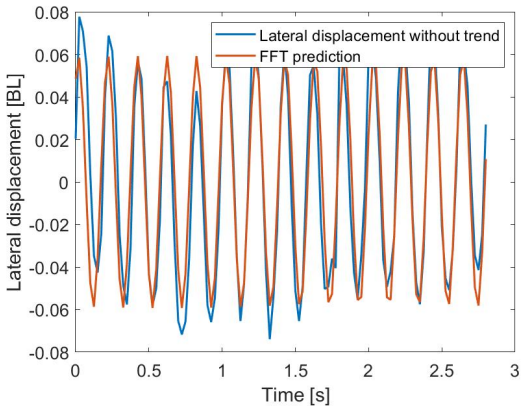

Figure C.18: Lateral displacement for 85 percent body length [BL] in time [s]

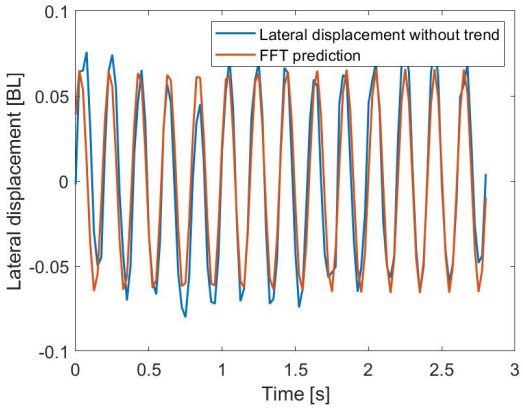

Figure C.19: Lateral displacement for 90 percent body length [BL] in time [s]

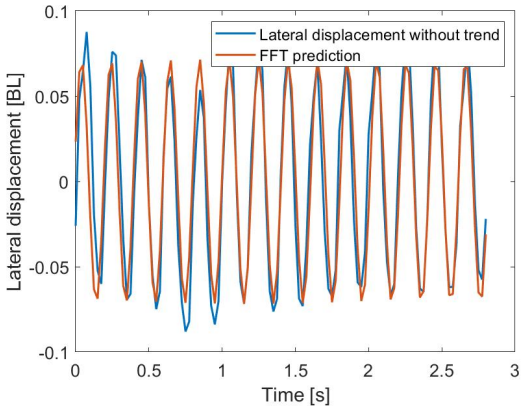

Figure C.20: Lateral displacement for 95 percent body length [BL] in time [s]

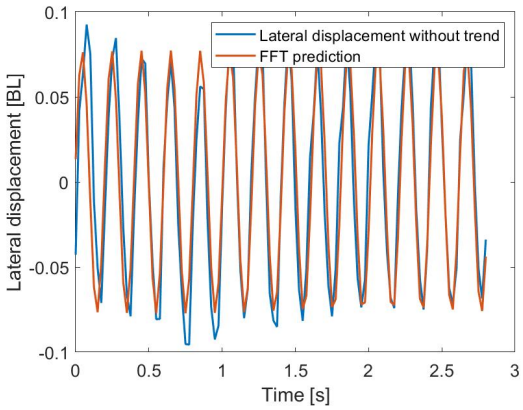

Figure C.21: Lateral displacement for 100 percent body length [BL] in time [s]

C.2 Movmean and Pchip

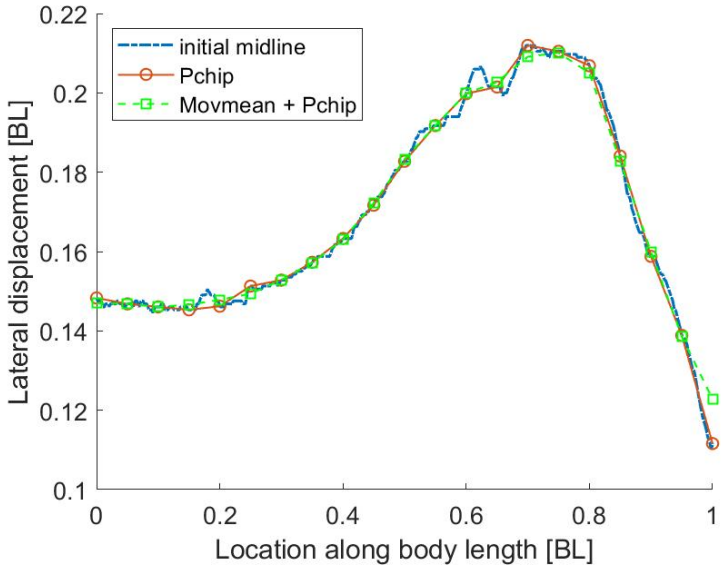

Figure C.22: Curve fitting, frame 1

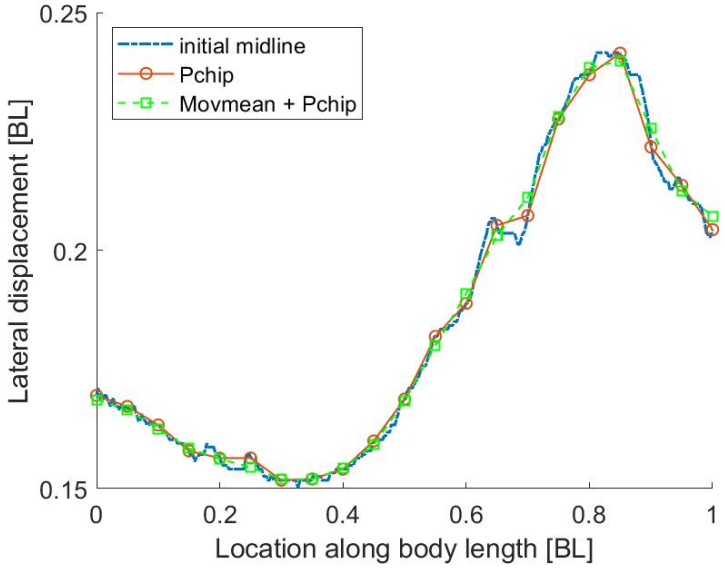

Figure C.23: Curve fitting, frame 2

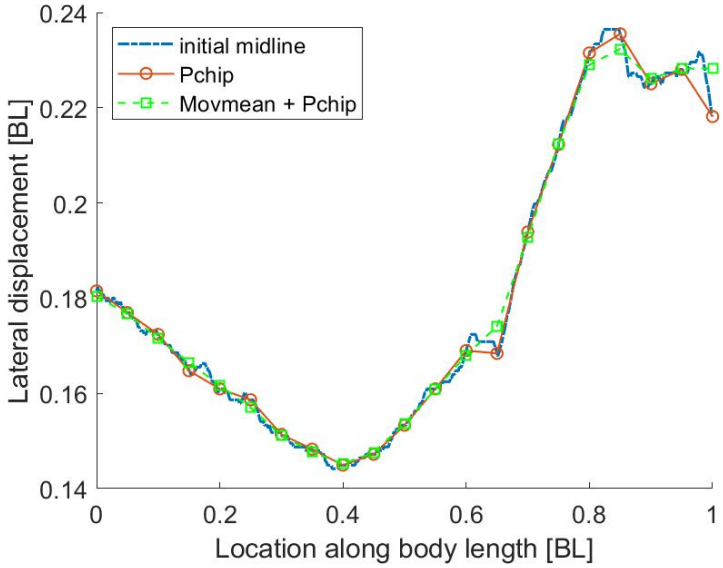

Figure C.24: Curve fitting, frame 3

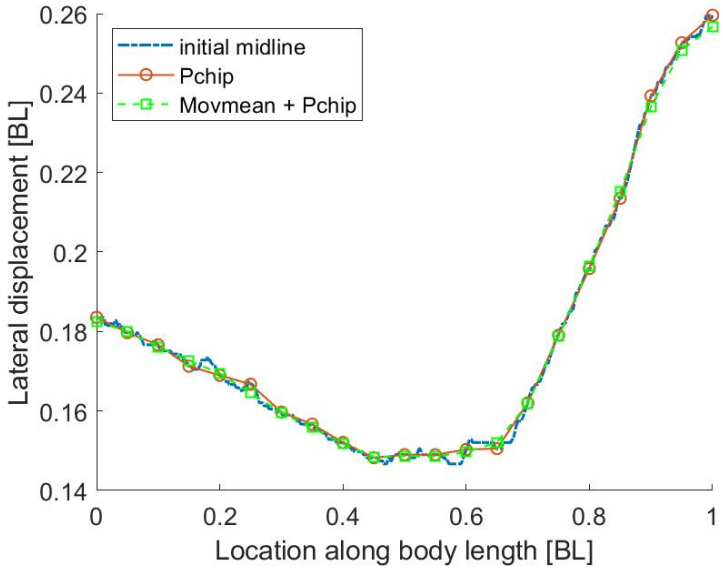

Figure C.25: Curve fitting, frame 4

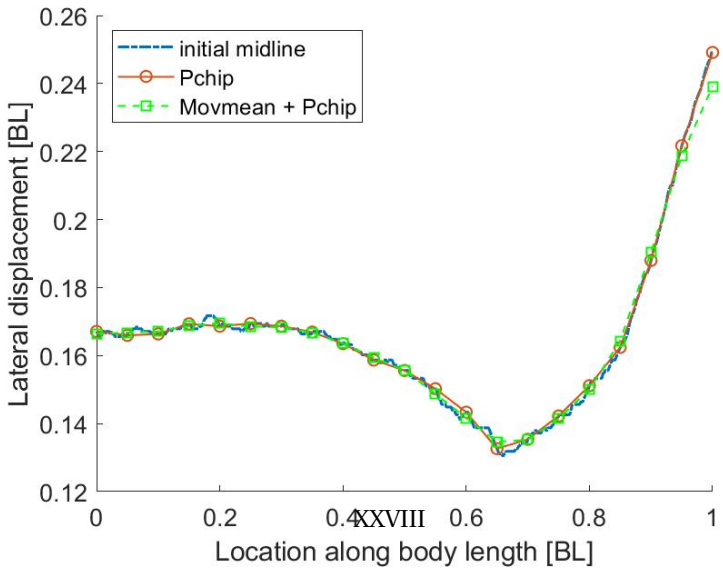

Figure C.26: Curve fitting, frame 5

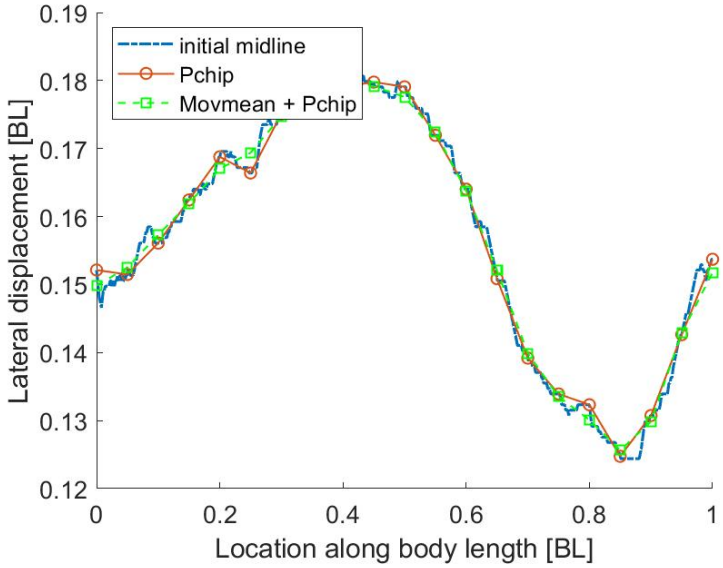

Figure C.27: Curve fitting, frame 6

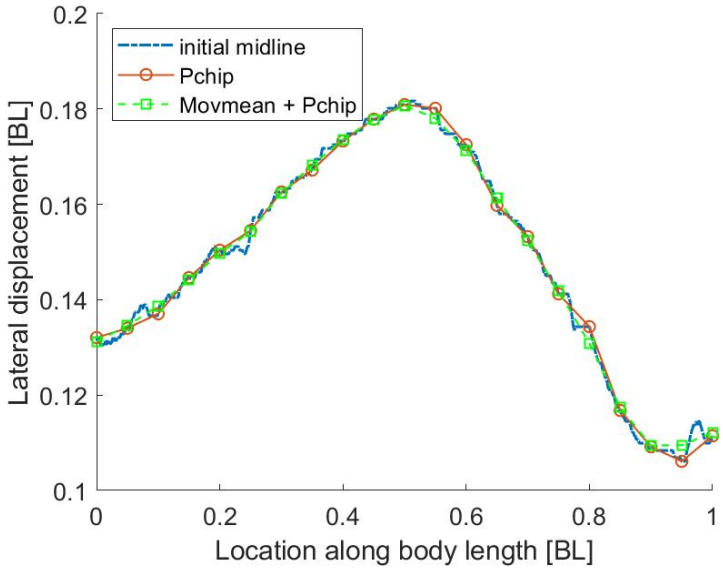

Figure C.28: Curve fitting, frame 7

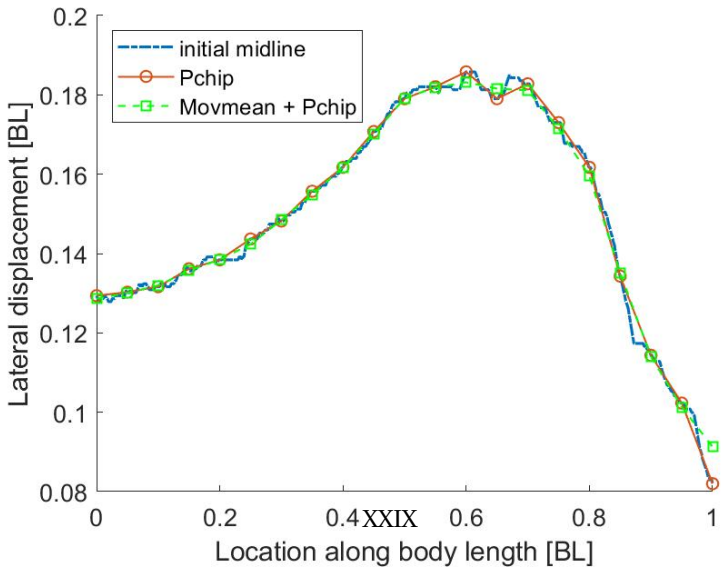

Figure C.29: Curve fitting, frame 8

Appendix D

Experimental layout

Suplementary images to understand the layout of the experiment on the sea bass.

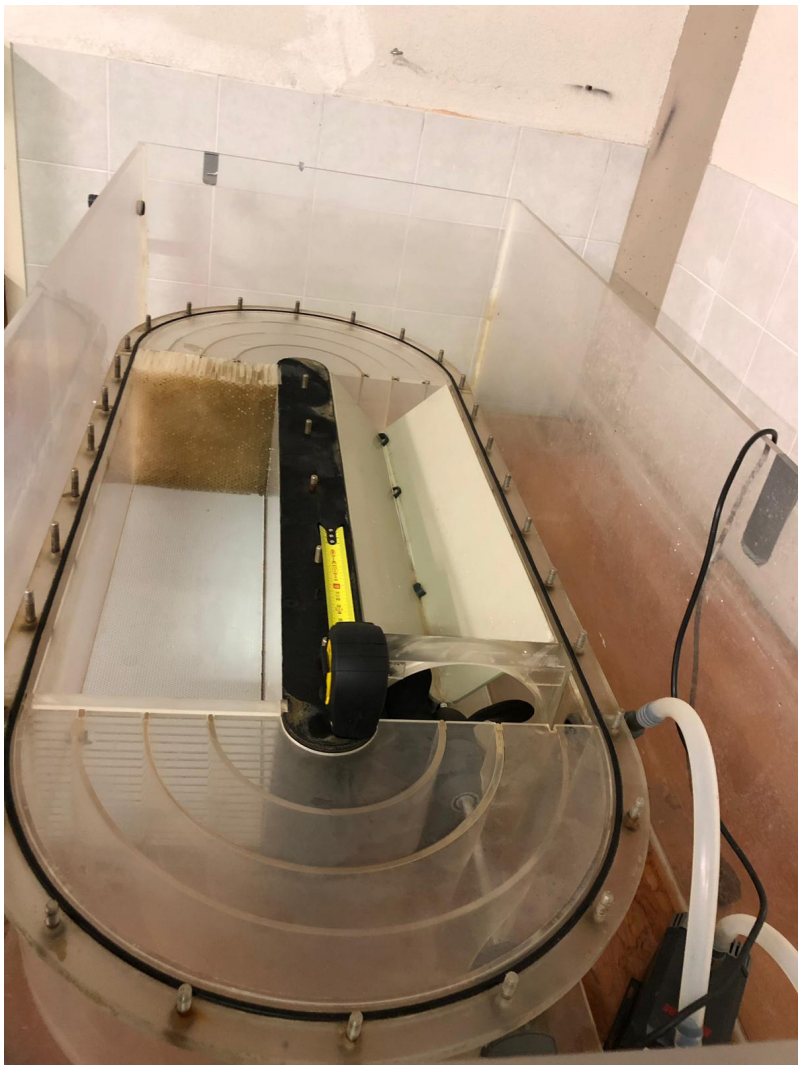

Figure D.1: Photo of the experimental setup. The photo is a courtesy of Adjunct Professor Claudio Lugni

Figure D.2: Side view of the sea bass from the experiment. The photo is a courtesy of Adjunct Professor Claudio Lugni

Appendix E

OpenFOAM

The lift coefficients for the first initial mesh refinements, mesh 1 to 5, where mesh 4 and 5 are on top of each other.

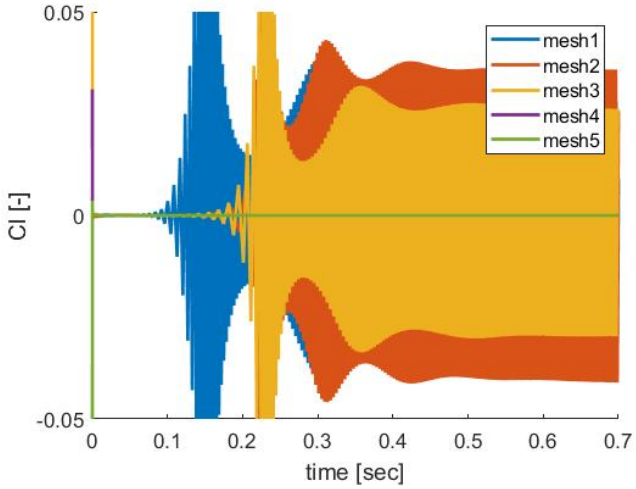

Figure E.1: Lift coefficient convergence, mesh 1 is unrefined and mesh 5 is the most refined.

The closer image of the plots above, E.1.

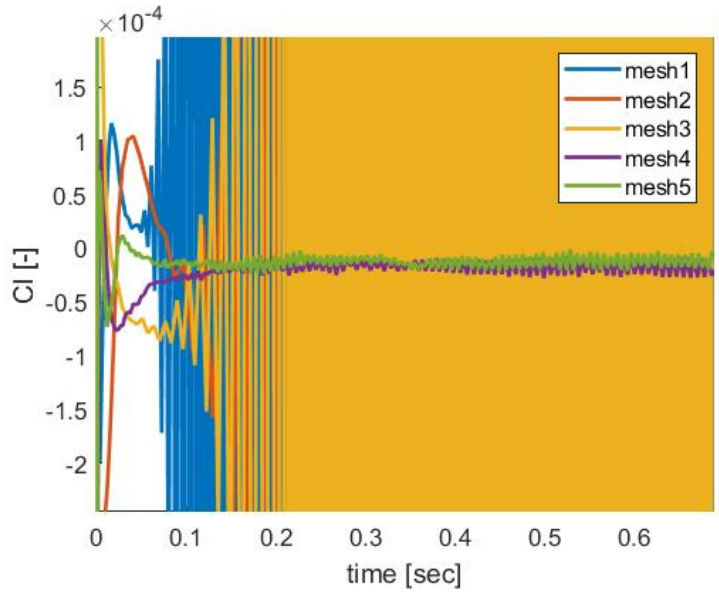

Figure E.2: Lift coefficient convergence, mesh 1 is unrefined and mesh 5 is the most refined.

The refinement of mesh2 from figure E.1, to improve the mesh.

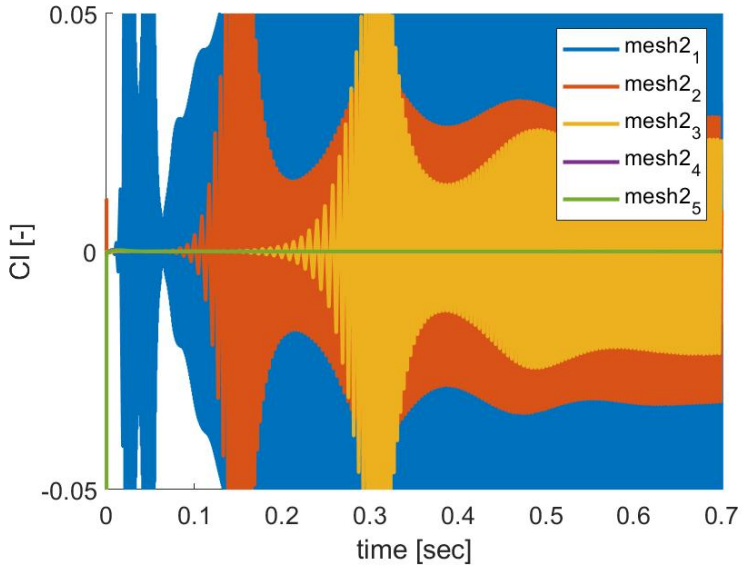

Figure E.3: Lift coefficient convergence, mesh 1 is unrefined and mesh 5 is the most refined.

The worst and the best results from the refinement of mesh2.

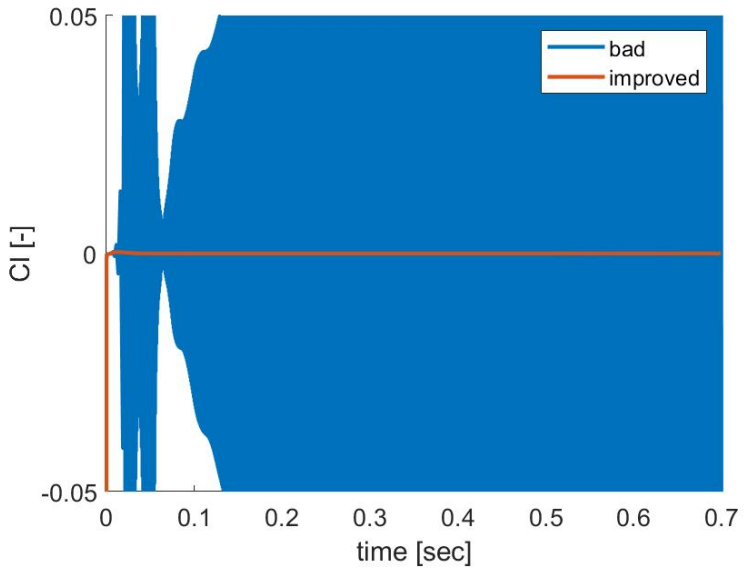

Figure E.4: grid size

The closer image of the plots above, E.4.

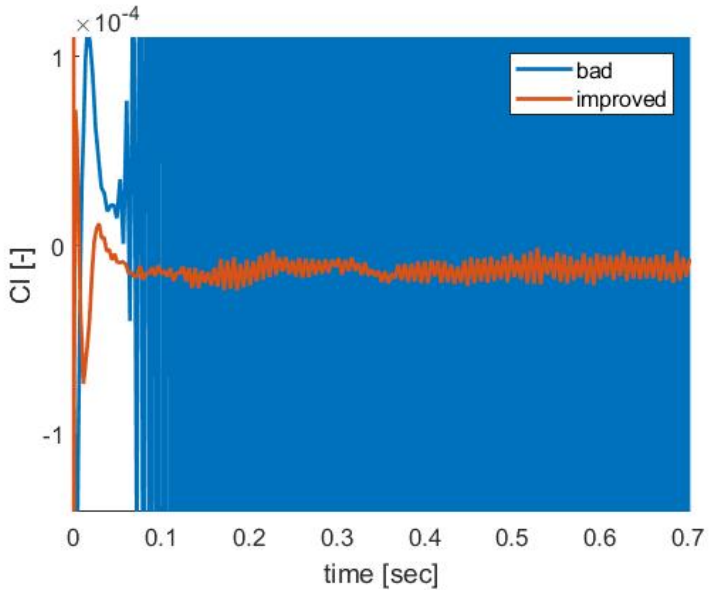

Figure E.5: grid size

The best of the refined mesh2, $Mesh2_5$, with a domain refinement.

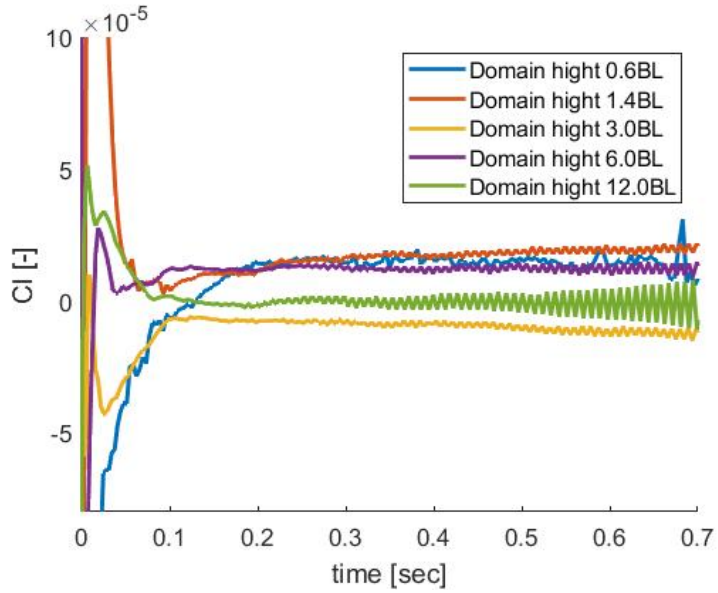

Figure E.6: $Mesh2_5$ with increasing domain size and same time duration as initially investigated

For the same duration as the previous plots, this seems promising, but after approximately 1 second the plots numerically explodes, as indicated in figure E.7.

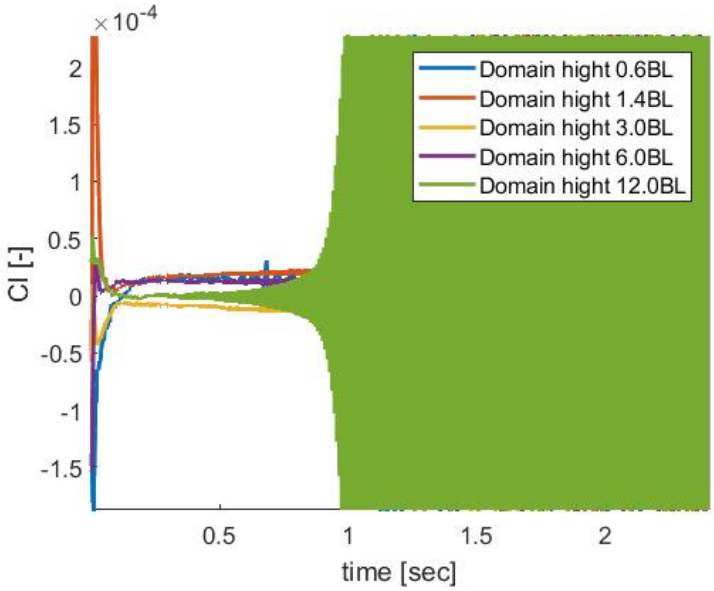

Figure E.7: $Mesh2_5$ with increasing domain size and time duration

This indicates that the improvement done for the unstable plot, only postponed the numerical explotion.

case hope1 and 2 as mesh 5 and 4 respectively, plotted for the lift coefficient in figure E.8 and drag coefficient in figure E.9.

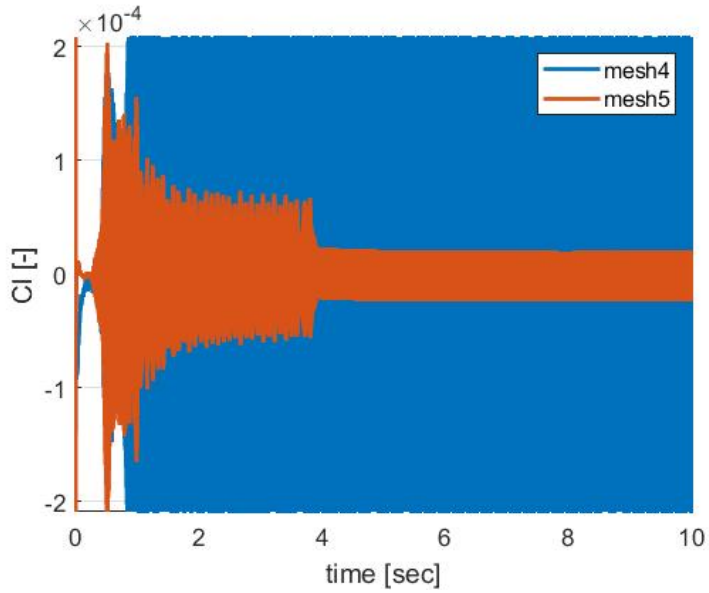

Figure E.8: Drag coefficients for the two finest grids. Zoomed in to show how the finest behaves.

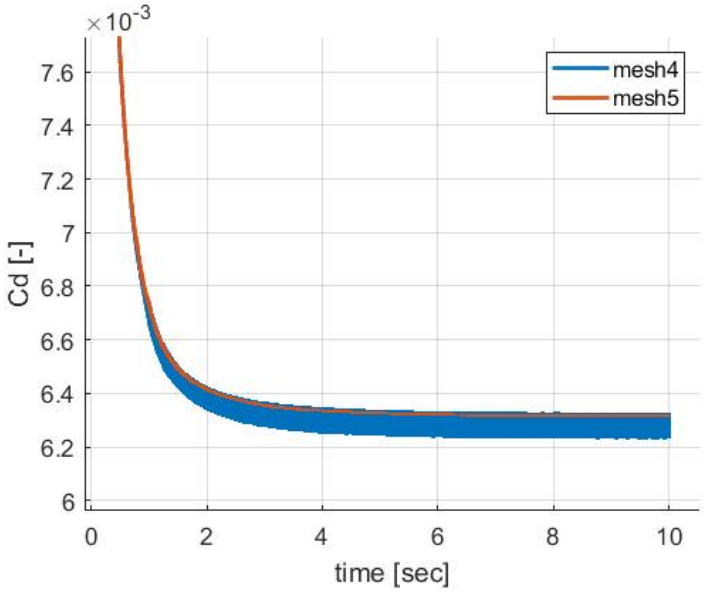

Figure E.9: Drag coefficients for the two finest grids.

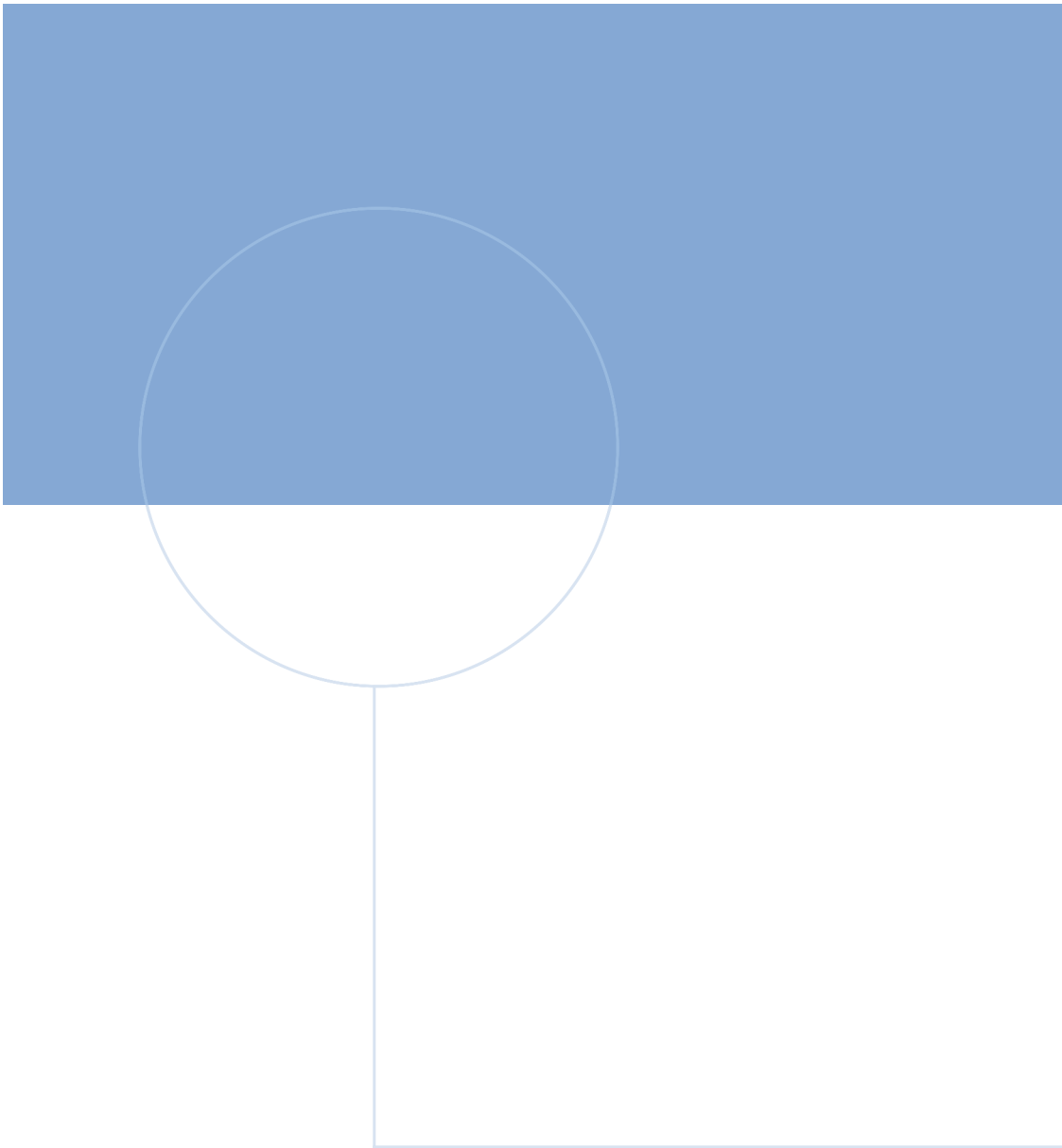

NTNU

Norwegian University of
Science and Technology